Springer Theses
Recognizing Outstanding Ph.D. Research

Axel U. J. Lode

Tunneling Dynamics in Open Ultracold Bosonic Systems

Numerically Exact Dynamics, Analytical Models, and Control Schemes

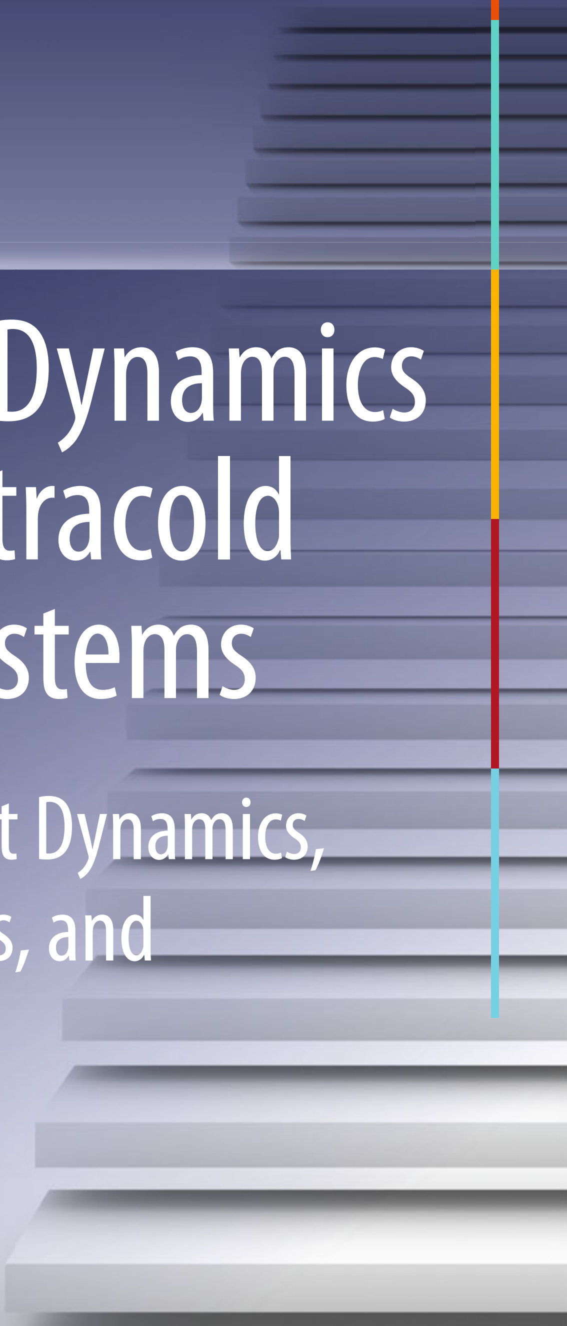

EXTRA
MATERIALS
extras.springer.com

Springer

Springer Theses

Recognizing Outstanding Ph.D. Research

For further volumes:
http://www.springer.com/series/8790

Aims and Scope

The series “Springer Theses” brings together a selection of the very best Ph.D. theses from around the world and across the physical sciences. Nominated and endorsed by two recognized specialists, each published volume has been selected for its scientific excellence and the high impact of its contents for the pertinent field of research. For greater accessibility to non-specialists, the published versions include an extended introduction, as well as a foreword by the student’s supervisor explaining the special relevance of the work for the field. As a whole, the series will provide a valuable resource both for newcomers to the research fields described, and for other scientists seeking detailed background information on special questions. Finally, it provides an accredited documentation of the valuable contributions made by today’s younger generation of scientists.

Theses are accepted into the series by invited nomination only and must fulfill all of the following criteria

- They must be written in good English.
- The topic should fall within the confines of Chemistry, Physics, Earth Sciences, Engineering and related interdisciplinary fields such as Materials, Nanoscience, Chemical Engineering, Complex Systems and Biophysics.
- The work reported in the thesis must represent a significant scientific advance.
- If the thesis includes previously published material, permission to reproduce this must be gained from the respective copyright holder.
- They must have been examined and passed during the 12 months prior to nomination.
- Each thesis should include a foreword by the supervisor outlining the significance of its content.
- The theses should have a clearly defined structure including an introduction accessible to scientists not expert in that particular field.

Axel U. J. Lode

Tunneling Dynamics in Open Ultracold Bosonic Systems

Numerically Exact Dynamics, Analytical Models, and Control Schemes

Doctoral Thesis accepted by
the University of Heidelberg, Germany

Springer

Author
Dr. Axel U. J. Lode
Condensed Matter Theory
and Quantum Computing Group
University of Basel
Basel
Switzerland

Supervisor
Prof. Dres h.c. Lorenz S. Cederbaum
Theoretical Chemistry Group
University of Heidelberg
Heidelberg
Germany

Videos to this book can be accessed at
http://www.springerimages.com/videos/978-3-319-07084-1

ISSN 2190-5053 ISSN 2190-5061 (electronic)
ISBN 978-3-319-07084-1 ISBN 978-3-319-07085-8 (eBook)
DOI 10.1007/978-3-319-07085-8
Springer Cham Heidelberg New York Dordrecht London

Library of Congress Control Number: 2014939408

© Springer International Publishing Switzerland 2015
This work is subject to copyright. All rights are reserved by the Publisher, whether the whole or part of the material is concerned, specifically the rights of translation, reprinting, reuse of illustrations, recitation, broadcasting, reproduction on microfilms or in any other physical way, and transmission or information storage and retrieval, electronic adaptation, computer software, or by similar or dissimilar methodology now known or hereafter developed. Exempted from this legal reservation are brief excerpts in connection with reviews or scholarly analysis or material supplied specifically for the purpose of being entered and executed on a computer system, for exclusive use by the purchaser of the work. Duplication of this publication or parts thereof is permitted only under the provisions of the Copyright Law of the Publisher's location, in its current version, and permission for use must always be obtained from Springer. Permissions for use may be obtained through RightsLink at the Copyright Clearance Center. Violations are liable to prosecution under the respective Copyright Law.
The use of general descriptive names, registered names, trademarks, service marks, etc. in this publication does not imply, even in the absence of a specific statement, that such names are exempt from the relevant protective laws and regulations and therefore free for general use.
While the advice and information in this book are believed to be true and accurate at the date of publication, neither the authors nor the editors nor the publisher can accept any legal responsibility for any errors or omissions that may be made. The publisher makes no warranty, express or implied, with respect to the material contained herein.

Printed on acid-free paper

Springer is part of Springer Science+Business Media (www.springer.com)

“... quantum physics means that anything can happen at any time for no reason.”

Professor Farnsworth, Futurama,
Bender’s Game

Supervisor's Foreword

The tunneling effect lies at the very heart of quantum mechanics. Quantum particles can penetrate through potential barriers even if they lack the energy to overcome them. Classical particles can only pass over the potential barrier and not through it. There is hence no classical equivalent of the tunneling effect. The amount of scientific work on tunneling of a single particle through a barrier is enormous. There is, however, very little knowledge on how a system made of several and certainly of many particles tunnels through a barrier to open space. The quantum mechanical process of tunneling in open many-body systems is of fundamental interest for many different branches of science. This is simply because almost all systems of interest in, for instance chemistry and physics, are open many-body systems. In chemistry, tunneling occurs in photoassociation and photodissociation processes, in nuclear physics tunneling is important for alpha decay and nuclear fission and fusion.

In the tunneling to open space process, a particle that has tunneled through the barrier will not return to the potential well out of which it has succeeded to escape. If several particles have tunneled, the situation becomes more intricate as these particles feel a drastically different situation outside the barrier than in the well. That the particles outside the well are no longer confined and, moreover, interacting with each other makes the mathematical and numerical treatment of tunneling to open space an extremely challenging task. Imagine that one particle has tunneled and the second one follows only some time later. In the meantime, the first one might already have travelled a long distance. This consideration makes it clear that one has to be able to treat a large if not enormous portion of free space correctly and precisely in order to describe the tunneling of a system made of a few and even more so of many particles to open space. The present thesis reports numerically exact descriptions of up to $N = 1001$ bosons in a spatial domain of more than 7 mm long (!). This, for a quantum many-body system, is truly tremendous.

The field of Bose–Einstein condensates has enjoyed enormous activity since their first production with ultracold gases in 1995. This unique state of matter of dilute atomic ultracold gases, is highly attractive for both experimental and theoretical scientists since the strength of the interaction between the bosons, their dimensionality, as well as the shape of the trap potential holding them can be varied and controlled essentially at will. It is due to these unique possibilities to control ultracold atoms that they are now used as so-called quantum simulators for a wide variety of other systems in solid state, particle, and even in astrophysics. In this spirit, the present theoretical thesis relies on ultracold bosons to study and analyze the effect of quantum many-body tunneling to open space theoretically. In the field, much attention has been paid to the investigation of the static and dynamic properties of Bose–Einstein condensates in traps and optical lattices. Here, there are two popular standard theories that dominate the literature: The famous Gross–Pitaevskii mean-field theory and the Bose–Hubbard lattice model of condensed-matter physics. It is not overestimating to note that there are more than a thousand manuscripts in the APS Journals dealing with the physics and properties of Bose–Einstein condensates as "seen" by these two theories. It has to be stressed that these theories rely on model considerations, whereas the current thesis presents numerically exact results of the full time-dependent Schrödinger equation. In that, the present thesis investigates in great detail and beyond the standard models the physics of tunneling to open space and finds and describes fascinating collective many-body phenomena, such as the mechanism of the loss of coherence in the process. It is furthermore found in a performed comparison that these fascinating many-body effects are not properly accounted for or even not contained in the standard Bose–Hubbard and Gross–Pitaevskii theories.

This thesis is among the first reports of numerically exact computations for the nonequilibrium quantum dynamics of interacting bosons in one and two spatial dimensions. The scheme pursued for the investigation of the tunneling process is as follows: A Bose–Einstein condensate is initially trapped in a potential well and then allowed to tunnel through a potential barrier to open space. Two generic scenarios are addressed. In the first, the barrier is ending at the same energy as the bottom of the well and thus all bosons can decay by tunneling out from the well (tunneling without a threshold). In the second scenario, the barrier is ending at an energy higher than the bottom of the well such that one or more particles of the condensate will not be able to tunnel and will have to stay in the well (tunneling with a threshold). The particles of the condensate are interacting with each other and the tunneling, of course, depends on this interaction. Both the spatial and momentum evolution of the full wave function of the condensate are investigated in great detail and the results are visualized by inspecting the one-particle and two-particle densities and correlation functions of the system as a function of time, both in real and momentum space. The results show extremely interesting physics not anticipated before and contradicting the above popular models. In particular, the tunneling mechanism found without a threshold can be viewed as if the bosons – although condensed in the well – tunnel one-by-one and lose their coherence in the process of escaping, i.e., the system fragments in open space! The study of tunneling with a threshold reveals, using the above mechanism, a strategy which allows a control of the momentum distribution and even the coherence properties (!) of the escaping particles.

The numerically exact calculations were carried out with an implementation of the multiconfigurational time-dependent Hartree for bosons (MCTDHB) method – the MCTDHB Package, see http://MCTDHB.org. The MCTDHB method is an efficient many-boson wave-packet propagation technique for the nonequilibrium dynamics of interacting bosons and is emerging as a leading many-body method for the quantum dynamics of Bose–Einstein condensates. With such complicated problems as the time-dependent many-boson Schrödinger equation, it is of great importance to validate and benchmark the quality of new methods. This is done in this thesis by identifying a model system of interacting bosons which can be solved exactly and subsequently using the MCTDHB Package, and comparing the predictions of the latter against these exact solutions of the many-boson Schrödinger equation. With this strategy, the present thesis first establishes the numerical exactness of MCTDHB for many-boson ground states in one and two dimensions. Subsequently and, most importantly, it is verified that MCTDHB can also numerically exactly calculate the real-time propagation of many-boson systems with a generalized Hamiltonian with both time-dependent one-body and two-body terms. The excellent agreement with the exact results is very valuable and establishes the MCTDHB method as a new standard for the physics of time-dependent many-boson systems.

Heidelberg, Germany, April 2014 Prof. Lorenz S. Cederbaum

Acknowledgments

My research in the recent years which culminates in this thesis was supported by many people to whom I feel deeply indebted.

First of all, I would like to thank my supervisor Prof. Dr. Lorenz S. Cederbaum. He always knew what objective to pursue when I was at my wit's end. The unique working environment provided in the Theoretical Chemistry group is an effect of his approach to science – without this encouraging and motivating environment as well as the brilliant way Lorenz Cederbaum asks scientific questions, I would not have finished this thesis.

The scientific work presented in this thesis builds on intense and inspiring discussions with, mentoring, tutoring, and the continuous support by Prof. Dr. Ofir E. Alon as well as Dr. Alexej I. Streltsov. I want to acknowledge also their and Dr. Kaspar Sakmann's contribution in copy-editing this thesis.

Next, I would like to thank Prof. Dr. Selim Jochim for pioneering experiments on the tunneling dynamics in open few-particle systems which are closely related to the physics of the present thesis. Furthermore, I want to thank him for refereeing this thesis. Finally, I would like to acknowledge him and the members of his *Ultracold Quantum Gases* group in Heidelberg for stimulating and interesting discussions.

I feel indebted for discussions with, criticism, and proof-reading service of Adrian Komainda, Alexander Kuleff, Alexej Streltsov, Samuel Markson, Ofir Alon, Daniel Pelaez-Ruiz, Elke Faßhauer, Matthis Eroms, Shachar Klaiman, Ulrike Lode, Marios Tsatsos, Shirin Faraji, Hans-Dieter Meyer, Lorenz S. Cederbaum, Kaspar Sakmann, and Andreas Deuchert.

I would like to express my gratitude for the support and encouragement by Dimitrios R.M. D.K. Voularinos, Dimitrios J.J. I. Papakonstantinou, Björn D. P.P. Jessen, Efi Anestedi, Aliki Petratou, Marios Tsatsos, Daniel Pelaez-Ruiz, Elke Faßhauer, Shirin Faraji, Susana Gomez, and the Therotical Chemistry group as a whole.

My siblings Ulrike and Holger Lode as well as my parents Marianne and Gernot Lode are acknowledged for their unconditional support and encouragement.

Last but not least, I am indebted to the relentless and invaluable inspiration, incentive, and support by Simone Lode (née Bruggesser) throughout all the years.

Supplementary Material

For the research presented in this thesis, the MCTDHB method to solve the time-dependent many-body problems for interacting bosons was a crucial ingredient. The MCTDHB software (see http://MCTDHB.uni-hd.de) needed to be improved and optimized in order to perform the demanding calculations for the tunneling to open space process. The gained numerical and programming know-how helped the development of the Open-Source MCTDHB package (see http://OpenMCTDHB.uni-hd.de), which is available for anyone who wants to try out the method. Eventually, the expertise gained in the research presented in this thesis lead to the development of the user-friendly, well-documented, efficient, and well-maintained recursive implementation of the MCTDHB method, R-MCTDHB (see http://ultracold.org).

The main research results in this thesis are results on the dynamics of quantum many-boson systems and a natural way to visualize such dynamics are videos of the respective quantities' time-evolutions. The figures for which a complementary video is available online have a caption marked by an asterisk, *.

Contents

Acronyms

1D	One-dimensional
2D	Two-dimensional
3D	Three-dimensional
ABM	Adams–Bashforth–Moulton predictor corrector method
BEC	Bose–Einstein condensate
BDF	Backwards differentiation formulae
BH	Bose–Hubbard
BHH	Bose–Hubbard Hamiltonian
BMF	Best mean-field, also time-dependent multi-orbital mean-field
DMRG	Density matrix renormalization group
DNLS	Discrete nonlinear Schrödinger equation
EOM	Equations of motion
GP	Gross–Pitaevskii
HIM	Harmonic interaction model
IMEST	Interaction matrix evaluation by successive transforms
MCTDH	Multiconfigurational time-dependent Hartree method
MCTDHB	Multiconfigurational time-dependent Hartree method for bosons
MPI	Message Passing Interface
OpenMP	Open Multi-Processing
QM	Quantum mechanics
RDM	Reduced density matrix
SIL	Short iterative Lanczos method
TDGP	Time-dependent Gross–Pitaevskii
TDSE	Time-dependent Schrödinger equation
TDVP	Time-dependent variational principle
TEBD	Time-evolving block decimation

Chapter 1
Introduction

> *"Begin at the beginning," the King said, gravely, "and go on till you come to an end; then stop."*
>
> Lewis Carroll, Alice in Wonderland

Though the physics of ultracold bosons is a rich field, still the physics of many interacting bosons tunneling to open space has not been described yet by means of exact methods. The present thesis connects both fields of ultracold atoms and many-body physics of tunneling. This introduction provides some basic knowledge of both scientific contexts, embeds them, and motivates the present connection.

1.1 Bose–Einstein Condensation

Bose–Einstein condensation is a phenomenon which has drawn the attention of the scientific community ever since its prediction in 1924 [1–3]. Until the actual production of a Bose–Einstein condensate (BEC), it took a very long time. Because sophisticated laser-cooling techniques, like for instance Doppler or Sisyphos cooling, are needed (see Refs. [4–7] for an overview). Finally, in 1995 three groups, independently, succeeded in cooling a trapped sample of ultracold bosons below the critical temperature for the formation of BECs. The first group, led by Ketterle, used repulsive sodium [8], the second, led by Cornell and Wieman, used repulsive rubidium [9], and the third one, led by Hulet, used attractive lithium [10]. Bose–Einstein condensation opened a door to the in-depth study of quantum many-body physics, because the amount of control that can be exerted on BECs in the lab is outstanding: their dimensionality [11–13], their confinement [14], and their interparticle interactions [15] can be controlled almost at will. Hence, BECs are used as so-called quantum simulators to emulate the physics encountered in other physical systems as, for instance, solid state systems (see e.g. [16]) or even analogs of black holes from astrophysics [17]. More recently, dipolar BECs have been realized in chromium [18]

A. U. J. Lode, *Tunneling Dynamics in Open Ultracold Bosonic Systems*,
Springer Theses, DOI: 10.1007/978-3-319-07085-8_1,

and dysprosium [19]. The presence of contact *and* dipolar interparticle interactions in these samples allows for an even bigger class of physical systems that can be studied in a well controlled experimental environment. Further applications of BECs include, for instance, precision measurements (see e.g. Ref. [20]), dynamics of BECs in optical lattices [21], quantum computation [22] and the study of vorticity and vortex dynamics [23]. A good overview of the present theoretical and experimental techniques and possibilities in the field is available in Refs. [21, 24–26].

It is appropriate to introduce here the definition for condensation put forward by Penrose and Onsager in the 1950s: the reduced one-body density matrix of a condensed quantum many-body system has only a single macroscopic eigenvalue [27]. This eigenvalue corresponds to the quantum mechanical single-particle state which is occupied by all the bosons. In several recent and more complex experiments, especially for the case of dynamical scenarios, it turned out that the reduced density matrix has several—in contrast to only a single—macroscopic eigenvalues. This interesting physical situation is referred to as the fragmentation of BECs, see Refs. [28–36].

With the wealth of accessible and controlled physical situations, it is of great interest to tackle further fundamental many-body problems. One of these is the many-boson tunneling process to open space. Beyond the well-known (effective) single-particle description of the process [37, 38], nearly nothing is known about its mechanism. This thesis explores and assesses the physics of tunneling from a many-body point of view and proposes and validates an intuitive model, as well as a scheme to manage and control the tunneling dynamics.

1.2 The Many-Body Physics of Tunneling

Ever since the beginning of quantum theory, the tunneling phenomenon was of great interest [37, 38]. This is mainly due to the lack of a classical analog. The tunneling process occurs in all potentials that have regions to which a classical particle could go, the so-called energetically allowed regions, as well as regions to which a classical particle could not go, the so-called energetically forbidden regions. Usually, an energetically allowed region is separated from an energetically forbidden one by a barrier. A quantum particle in such a potential can overcome the potential barrier without having the necessary average energy, because its position is described by a probability distribution which is bigger than 0 in the classically forbidden regions of the potential (cf. Fig. 1.1). With this very general condition for its occurrence, quantum tunneling is characteristic for many processes and omnipresent in nature and its physical systems. It occurs in the field of nuclear physics in fusion [39] and fission [40], in the field of chemistry in photodissociation [41] as well as photoassociation [42], to name just a few. It is important to stress here that almost all of the systems in which the tunneling phenomenon occurs are many-body systems which are, in principle, open. Yet, the tunneling process is conventionally studied from an effective single-particle perspective—neglecting the dynamics of correlations

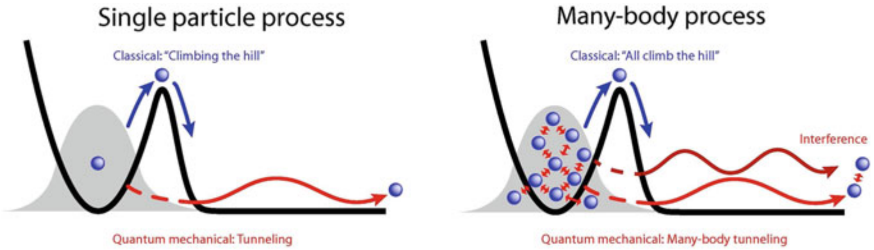

Fig. 1.1 Sketch of Single- and Many-Particle Tunneling

between the constituent particles of the system. For an illustration, compare the left and right panels of Fig. 1.1. A theoretical or experimental study with BECs beyond the simplified effective single particle picture is a complicated task, which necessitates sophisticated methods and new ways of analysis. The realization of BECs [8–10] and the aforementioned developments provided new possibilities to study many-body tunneling in a very well-controlled environment. For ultracold bosonic atoms, the Hamiltonian of the many-body system is known explicitly. The Hamiltonian uniquely defines the dynamics via the time-dependent Schrödinger equation (TDSE). Hence, the time-evolution and quantum dynamics are also known, in principle. With the multiconfigurational time-dependent Hartree for bosons (MCTDHB) method numerically exact solutions of the TDSE for many bosons for general time-dependent problems were recently made available [28, 43] for the first time.

In the present thesis, the full many-body results are compared to the single particle case in order to explore the collective many-body phenomena and correlation dynamics in the tunneling process. The analysis of the many-boson physics explains how the overall tunneling to open space process can be modeled as an interference of simultaneous single-particle tunneling processes emerging from a coherent source. With this understanding, a scheme for the control of the dynamics in the many-body system is formulated and verified.

1.3 Theoretical Description of Quantum Many-Body Systems

The challenge that arises when one tries to solve the TDSE of a many-body system lies in the high dimensionality of its solution. The solution of the TDSE for N particles in D-dimensional space is the time-dependent probability distribution that depends on each of the N particles' positions, hence, it has dimensionality $D \cdot N$. In almost all cases such a solution has no closed analytical expression. Furthermore, clever representations are needed for such a high-dimensional solution. A common way to approach the problem of solving the many-body TDSE is variational methods. Basically, one makes an hopefully clever ansatz for the wave function that contains parameters. For these parameters, equations of motion can be obtained from the time-dependent variational principle [44]. These equations of motion depend on the parameters in the ansatz and determine their time-evolution. Depending on the physics of the many-body system and the quality of the ansatz made, such an effective description may be accurate or inaccurate.

The present thesis contains a plethora of results rooting in a recently achieved breakthrough with variational methods used to solve the many-boson TDSE: the derivation and implementation of the multiconfigurational time-dependent Hartree for bosons (MCTDHB) method in 2007, see Ref. [45]. In the history of variational methods, MCTDHB is the first to provide numerically exact solutions of the TDSE for a wide variety of many-boson problems. Chronologically, the complexity of the time-adaptive ansatzes used for the derivation of variational methods grew. Gross and Pitaevskii were using a so-called product state as the ansatz for the many-particle wave function in 1961. The assumption implies that all bosons are occupying one (time-dependent) single-particle state. The equation of motion for this state is termed the the time-dependent Gross–Pitaevskii equation (TDGP) (cf. Refs. [46, 47]). It is well-suited to describe fully condensed systems and is an effective single-particle or mean-field method since it uses only one single-particle state. In many physical situations correlations start to play a role and particles tend to occupy several single particle states. Such, so-called fragmented states of many-body systems cannot be described by the product ansatz that leads to the TDGP equation. In order to describe also fragmented states, a more complex ansatz is needed. The straightforward generalization that allows the particles to occupy several instead of only one single-particle state was derived and implemented in 2003 and 2007 and is termed best mean-field (BMF) [48, 49]. BMF is capable of describing fragmented many-body states and thus allows one to systematically go beyond the effective single-particle or mean-field description. The TDGP equation is contained in the BMF equations as the special case in which all bosons occupy a single state only. Basically, BMF constructs a single, variationally optimized fully symmetrized many-body configuration made of several single-particle states. In modern experiments with ultracold atoms, often quite drastic changes of the environment are performed. Quenches, where a parameter in the system is changed abruptly, are, for instance, widely spread experimental setups. In such experiments, the many-body nature of the quantum state of the system can change. For example, an initially condensed system could lose its coherence and become fragmented with time because the external potential was changed from a harmonic confinement to an optical lattice in the experiment (see e.g. Ref. [50]). To describe such different quantum phases, at least two types of many-body states are required: a product, i.e., coherent mean-field-like state and a fragmented, i.e., incoherent BMF-like state. Hence, to tackle quantum many-body dynamics where the many-body properties are allowed to change with time in a general manner, several configurations, i.e., BMF-like states are necessary in the description. This can be achieved by taking as the ansatz for a variational calculation a time-dependently weighted sum of all possible configurations that can be formed with a certain number of time-dependent single-particle states. Then, the resulting equations of motion can describe the details of the transitions from coherence to fragmentation. This is precisely what the aforementioned MCTDHB ansatz does. MCTDHB is a self-consistent generalization of the BMF and TDGP methods, both of which it contains as a special case. MCTDHB can be considered as an exact diagonalization with a time-adaptive orbital basis set. Lattice models like for instance the Bose–Hubbard model can be arrived at from MCTDHB by dropping the time-dependence of the orbitals and neglecting contributions of off-diagonal interaction matrix elements. It is worthwhile to stress here that MCTDHB is in principle exact when the number of single-particle states taken into account can be taken large enough. The only limitation is the computational effort. The numerical exactness is assessed in the present thesis by showing the convergence of the MCTDHB method to the exact solution of the full time-dependent many-body Schrödinger equation of a solvable problem of bosons with both time-dependent external and time-dependent interparticle interaction potential.

1.4 Structure of this Thesis

Chapter 2 provides an introduction to the quantum-physical methods in the field and focuses on the ones that are used throughout this thesis. The quality and the numerical implementation of the aforementioned MCTDHB theory is assessed. This is done by, first, a benchmark and, second, a comparative study with lattice models. For the benchmark the analytically solvable harmonic interaction model (HIM) and a time-dependent generalization of it (TDHIM) (see also Ref. [43]) is used in Chap. 3. The comparison is done with the help of a Bose–Hubbard simulation and a mapping of discrete and continuous space in Chap. 4. In Chap. 5 several analytical considerations on the many-body physics in the tunneling process to open space are presented. For instance, the aforementioned model assembling the many-body dynamics from simultaneous single-particle processes is derived and discussed. Chap. 6 presents numerically exact results for the many-boson tunneling to open space process and discusses the significance of correlation and coherence dynamics in this many-body process. Furthermore, the models formulated in Chap. 5 are verified. In Chap. 7 the dynamics in the tunneling process of many bosons to open space are subjected to a threshold, i.e., a non-zero value of the potential in the asymptotic region. To model the dynamics properly, the introduced model with simultaneous single-particle-tunneling processes is modified accordingly. It is shown how the counting statistics and correlation dynamics in the process can be controlled by manipulating the threshold and interparticle interactions. A summary of the findings and an outlook complete the present thesis in Chap. 8. The Appendices collect longer analytical calculations as well as other derived many-body analysis quantities which have not been applied numerically so far.

References

1. A. Einstein, Quantentheorie des einatomigen idealen Gases. II. Sitzungsber. Preuss. Akad. Wiss. Bericht **1**, 3 (1925)
2. S.N. Bose, Plancks Gesetz und Lichtquantenhypothese. Z. Phys. **26**, 178–181 (1924)
3. A. Einstein, Quantentheorie des einatomigen idealen Gases. Sitzungsber. Preuss. Akad. Wiss. Bericht **22**, 261 (1924)
4. T.W. Hänsch, A.L. Schawlow, Cooling of gases by laser radiation. Opt. Commun. **13**(1), 68–69 (1975)
5. N.R. Newbury, C.J. Myatt, E.A. Cornell, C.E. Wieman, Gravitational Sisyphus Cooling of ^{87}Rb in a Magnetic Trap. Phys. Rev. Lett. **74**, 2196–2199 (1995)
6. J.I. Cirac, R. Blatt, P. Zoller W.D. Phillips, Laser cooling of trapped ions in a standing wave. Phys. Rev. A **46**, 2668–2681 (1992)
7. H.J. Metcalf, P. Van Der Straten, *Laser Cooling and Trapping* (Springer, New York Inc., 1999)
8. K.B. Davis, M.-O. Mewes, M.R. Andrews, N.J. van Druten, D.S. Durfee, D.M. Kurn, W. Ketterle, Bose–Einstein Condensation in a Gas of Sodium Atoms. Phys. Rev. Lett. **75**, 3969 (1995)
9. M.H. Anderson, J.R. Ensher, M.R. Matthews, C.E. Wiemann, E.A. Cornell, Observation of Bose–Einstein Condensation in a Dilute Atomic Vapor. Science **269**, 198 (1995)
10. C.C. Bradley, C.A. Sackett, J.J. Tollet, R.G. Hulet, Evidence of Bose–Einstein Condensation in an Atomic Gas with Attractive Interactions. Phys. Rev. Lett. **75**, 1687 (1995)
11. A. Görlitz et al., Realization of Bose–Einstein Condensates in Lower Dimensions. Phys. Rev. Lett. **87**, 130402 (2001)
12. F. Schreck et al., Quasipure Bose–Einstein Condensate Immersed in a Fermi Sea. Phys. Rev. Lett. **87**, 080403 (2001)
13. M. Greiner et al., Exploring Phase Coherence in a 2D Lattice of Bose–Einstein Condensates. Phys. Rev. Lett. **87**, 160405 (2001)
14. K. Henderson, C. Ryu, C. MacCormick, M.G. Boshier, Experimental demonstration of painting arbitrary and dynamic potentials for Bose–Einstein condensates. New J. Phys. **11**, 043030 (2009)
15. C. Chin, R. Grimm, P. Julienne, E. Tiesinga, Feshbach resonances in ultracold gases. Rev. Mod. Phys. **82**, 1225 (2010)
16. M. Greiner, O. Mandel, T. Esslinger, T.W. Hänsch, I. Bloch, Quantum phase transition from a superfluid to a Mott insulator in a gas of ultracold atoms. Nature **415**, 39–44 (2002)
17. O. Lahav, A. Itah, A. Blumkin, C. Gordon, S. Rinott, A. Zayats, J. Steinhauer, Realization of a Sonic Black Hole Analog in a Bose–Einstein Condensate. Phys. Rev. Lett. **105**, 240401 (2010)
18. A. Griesmaier, J. Werner, S. Hensler, J. Stuhler, T. Pfau, Bose–Einstein Condensation of Chromium. Phys. Rev. Lett. **94**, 160401 (2005)
19. M. Lu, N.Q. Burdick, S.H. Youn, B.L. Lev, Strongly Dipolar Bose–Einstein Condensate of Dysprosium. Phys. Rev. Lett. **107**, 190401 (2011)
20. J. Dunningham, K. Burnett, W.D. Phillips, Bose–Einstein condensates and precision measurements. Phil. Trans. R. Soc. A **363**, 2165–2175 (2005)
21. O. Morsch, M.K. Oberthaler, Dynamics of Bose–Einstein condensates in optical lattices. Rev. Mod. Phys. **78**, 179–215 (2006)
22. T. Calarco, U. Dorner, P.S. Julienne, C.J. Williams, P. Zoller, Quantum computations with atoms in optical lattices: Marker qubits and molecular interactions. Phys. Rev. A **70**, 012306 (2004)
23. D.V. Freilich, D.M. Bianchi, A.M. Kaufman, T.K. Langin, D.S. Hall, Real-time Dynamics of Single Vortex Lines and Vortex Dipoles in a Bose–Einstein Condensate. Science **329**(5996), 1182–1185 (2010)
24. W. Ketterle, Nobel lecture: When atoms behave as waves: Bose–Einstein condensation and the atom laser. Rev. Mod. Phys. **74**, 1131–1151 (2002)

25. I. Bloch, J. Dalibard, W. Zwerger, Many-body physics with ultracold gases. Rev. Mod. Phys. **80**, 885 (2008)
26. C.J. Pethick, H. Smith, *Bose–Einstein Condensation in Dilute Gases* (Cambridge University Press, Cambridge, 2008)
27. O. Penrose, L. Onsager, Bose–Einstein Condensation and Liquid Helium. Phys. Rev. **104**, 576–584 (1956)
28. K. Sakmann, A.I. Streltsov, O.E. Alon, L.S. Cederbaum, Exact Quantum Dynamics of a Bosonic Josephson Junction. Phys. Rev. Lett. **103**, 220601 (2009)
29. L.S. Cederbaum, A.I. Streltsov, O.E. Alon, Fragmented Metastable States Exist in an Attractive Bose–Einstein Condensate for Atom Numbers Well Above the Critical Number of the Gross–Pitaevskii Theory. Phys. Rev. Lett. **100**, 040402 (2008)
30. A.I. Streltsov, O.E. Alon, L.S. Cederbaum, Role of Excited States in the Splitting of a Trapped Interacting Bose–Einstein Condensate by a Time-Dependent Barrier. Phys. Rev. Lett. **99**, 030402 (2007)
31. O.E. Alon, A.I. Streltsov, L.S. Cederbaum, Zoo of Quantum Phases and Excitations of Cold Bosonic Atoms in Optical Lattices. Phys. Rev. Lett. **95**, 030405 (2005)
32. O.E. Alon, L.S. Cederbaum, Pathway from Condensation via Fragmentation to Fermionization of Cold Bosonic Systems. Phys. Rev. Lett. **95**, 140402 (2005)
33. P. Bader, U.R. Fischer, Fragmented Many-Body Ground States for Scalar Bosons in a Single Trap. Phys. Rev. Lett. **103**, 060402 (2009)
34. R.W. Spekkens, J.E. Sipe, Spatial fragmentation of a Bose–Einstein condensate in a double-well potential. Phys. Rev. A **59**, 3868–3877 (1999)
35. E.J. Mueller, T.-L. Ho, M. Ueda, G. Baym, Fragmentation of Bose–Einstein condensates. Phys. Rev. A **74**, 033612 (2006)
36. C. Weiss, Y. Castin, Creation and Detection of a Mesoscopic Gas in a Nonlocal Quantum Superposition. Phys. Rev. Lett. **102**, 010403 (2009)
37. G. Gamow, Zur Quantentheorie des Atomkernes. Z. f. Phys. **51**(3–4), 204–212 (1928)
38. H.A. Kramers, Wellenmechanik und halbzählige Quantisierung. Zeitschr. f. Physik A **39** (10–11), 828–840 (1926)
39. N. Takigawa, A.B. Balantekin, Quantum tunneling in nuclear fusion. Rev. Mod. Phys. **70**, 77–100 (1998)
40. B.S. Bhandari, Resonant tunneling and the bimodal symmetric fission of ^{258}Fm. Phys. Rev. Lett. **66**, 1034–1037 (1991)
41. J. Keller, J. Weiner, Direct measurement of the potential-barrier height in the $\mathrm{B}^1\Pi_u$ state of the sodium dimer. Phys. Rev. A **29**, 2943–2945 (1984)
42. M. Vatasescu et al., Multichannel tunneling in the $\mathrm{Cs}_2 0_g^-$ photoassociation spectrum. Phys. Rev. A **61**, 044701 (2000)
43. A.U.J. Lode, K. Sakmann, O.E. Alon, L.S. Cederbaum, A.I. Streltsov, Numerically exact quantum dynamics of bosons with time-dependent interactions of harmonic type. Phys. Rev. A **86**, 063606 (2012)
44. P. Kramer, M. Saraceno, *Geometry of the Time-Dependent Variational Principle* (Springer, Heidelberg, 1981)
45. O.E. Alon, A.I. Streltsov, L.S. Cederbaum, Multiconfigurational time-dependent Hartree method for bosons: Many-Body dynamics of bosonic systems. Phys. Rev. A **77**, 033613 (2008)
46. E.P. Gross, Structure of a quantized vortex in boson systems. II Nuovo Cimento **20**, 454 (1961)
47. L.P. Pitaevskii, Vortex lines in an imperfect Bose gas. Sov. Phys. JETP **13**, 451 (1961)
48. L.S. Cederbaum, A.I. Streltsov, Best mean-field for condensates. Phys. Lett. A **318**, 564–569 (2003)
49. O.E. Alon, A.I. Streltsov, L.S. Cederbaum, Time-dependent multiorbital mean-field for fragmented Bose–Einsten condensates. Phys. Lett. A **362**, 453–459 (2007)
50. I. Březinová, A.U.J. Lode, A.I. Streltsov, O.E. Alon, L.S. Cedrbaum, J. Burgdörfer, Wave chaos as signature for depletion of a Bose–Einstein condensate. Phys. Rev. A **86**, 013630 (2012)

Chapter 2
Theoretical Concepts and Numerical Methods

> *Being ignorant is not so much a shame, as being unwilling to learn.*
>
> Benjamin Franklin

The scope of this chapter is to give an overview of the various methods available to tackle the problem of solving the TDSE for a system of many bosons. In the rich variety of literature on this problem, References [1, 2] provide a good starting point. Here, special attention is devoted to the motivation and illustration of the mean-field methods and their multiconfigurational generalizations, because these are the methods within which most of the numerical results in the present study have been obtained. To give a self-contained picture, it is a good approach to review the basics of the second quantized formulation of the quantum mechanics of bosons, as well as some of the theoretical concepts used in the field. The approximations considered here fall into two different categories: the first set relies on making assumptions solely on the ansatzes and intends to solve the *full many-body* Hamiltonian (the Gross–Pitaevskii theory, best mean-field theory, and, MCTDHB). The second set relies on making assumptions on the physical situation and constructing model Hamiltonians and possibly also ansatzes for the wave functions (such as the Bose–Hubbard Hamiltonian (BHH), and the discrete non-linear Schrödinger equation (DNLS)). All these approximations allow for an analytical description only in very rare and special cases or under additional assumptions—it is therefore inevitable to construct methods to solve them numerically in order to avoid the necessity of further idealizations. The above points are discussed in this chapter.

2.1 The Schrödinger Equation from a Many-Body Perspective

The many-body Schrödinger equation reads:

$$\hat{H}(\vec{r}_1, ..., \vec{r}_N, t)\Psi(\vec{r}_1, ..., \vec{r}_N, t) = i\partial_t \Psi(\vec{r}_1, ..., \vec{r}_N, t). \tag{2.1}$$

A. U. J. Lode, *Tunneling Dynamics in Open Ultracold Bosonic Systems*,
Springer Theses, DOI: 10.1007/978-3-319-07085-8_2,

Here, both, $\hat{H}$ and the wave function Ψ depend on the positions of the N particles. In many cases, the Hamiltonian $\hat{H}$ is an Hermitian operator in the N-particle Hilbert space. For N identical bosons, both $\hat{H}$ and Ψ are symmetric when interchanging any two of the coordinates in Eq. (2.1). Hereafter, a Hamiltonian with a single particle potential for each particle and two-body interactions for every pair of particles is considered,

$$\begin{aligned}\hat{H} &= \sum_{i=1}^{N} \hat{h}(\vec{r}_i) + \sum_{i<j}^{j=N} \hat{W}(\vec{r}_j, \vec{r}_i, t),\\ \hat{h}(\vec{r}) &= \hat{T}(\vec{r}) + V(\vec{r}, t),\\ \hat{T}(\vec{r}) &= -\frac{1}{2}\partial_{\vec{r}}^2,\end{aligned} \tag{2.2}$$

unless otherwise specified. Here $\hat{W}$ is the two-body interaction, V is the one-body potential, and $\hat{T}$ is the usual kinetic energy in dimensionless units with $\hbar = m = 1$. Both, $\hat{W}$ and V, can be time-dependent but for most of the problems they will be considered as time-independent. For ultracold bosons it is usually assumed that the two-body physics are well-described by s-wave scattering. Ultracold temperatures imply very low kinetic energies. Hence, only the s-wave is contributing to the partial wave expansion of the scattering processes. In this case:

$$\hat{W}(\vec{r}_i, \vec{r}_j) = \lambda_0 \delta(\vec{r}_i - \vec{r}_j), \tag{2.3}$$

where λ_0 relates to the s-wave scattering length [3, 4]. Already from Eqs. (2.1), and (2.2) it is obvious that this problem becomes high-dimensional for several particles $N > 1$. It is hence difficult to solve and approximations are a must in the many particle case. A very efficient formalism for treating systems of N identical particles is called second quantization. It is explained below.

2.1.1 Second Quantization

The space of many-boson wave functions is the N-particle Hilbert space [5]. Conventionally, a complete and orthonormal set of single-particle states,[1] $\{|a_i\rangle, i = 1, ..., N\}$ is chosen to describe this N-particle Hilbert space. In this basis, a state of N distinguishable particles is the product

$$|a_1\rangle \cdots |a_N\rangle = |a_1, ..., a_N\rangle,$$

where the subscript identifies the particle. Straightforwardly, symmetrized products, the so-called permanents, can be formed by summing all possible permutations of this

---

[1] For didactical reasons, the time-dependencies are omitted in various places in this section.

expression. This summation is denoted as the action of the so-called symmetrization operator $\hat{\mathcal{S}}_+$. Hence, the permanent has the following properties:

$$\hat{\mathcal{S}}_+ \left[|a_1, ..., a_N\rangle\right] = \frac{1}{N!} \sum_{\{\vec{a}\}} |\vec{a}\rangle. \tag{2.4}$$

Here $\{\vec{a}\} = \{|a_\alpha, ..., a_\omega\rangle\}$ denotes all possible permutations of the indices $\alpha, ..., \omega$, and $\hat{\mathcal{S}}_+$ is the symmetrization operator for bosons. Permanents are fully symmetric, N-dimensional, orthogonal functions. If one assumes, that one of the single particle states $|a_i\rangle$ is occupied by n_i bosons, the symmetrization with $\hat{\mathcal{S}}_+$ will make it occur $n_i!$ times in the right hand side of Eq. (2.4). To obtain a proper normalization, one has to divide by the square root of $n_i!$ for all i. Hence, it follows for the permanent $|n_1, n_2, ...\rangle$:

$$|n_1, n_2, ...\rangle = \frac{1}{\sqrt{n_1! n_2! \cdots}} \hat{\mathcal{S}}_+ \left[|a_1, ..., a_N\rangle\right] \tag{2.5}$$

$$\langle n_1, n_2, ...|n_1', n_2', ...\rangle = \delta_{n_1, n_1'} \delta_{n_2, n_2'} \cdots \tag{2.6}$$

$$\sum_{n_1, n_2, ...} |n_1, n_2, ...\rangle\langle n_1, n_2, ...| = \mathbf{1}. \tag{2.7}$$

Here, a constant particle number, i.e. $\sum_{i=1}^{\infty} n_i = N$ was assumed. By introducing the conventional creation and annihilation operators, respectively:

$$\hat{a}_i^\dagger |..., n_i, ...\rangle = \sqrt{n_i + 1} |..., n_i + 1, ...\rangle$$
$$\hat{a}_i |..., n_i, ...\rangle = \sqrt{n_i} |..., n_i - 1, ...\rangle,$$

it is possible to write a general single-permanent many-boson state as:

$$|n_1, n_2, ...\rangle = \frac{1}{n_1! n_2! \cdots} \left(\hat{a}_1^\dagger\right)^{n_1} \left(\hat{a}_2^\dagger\right)^{n_2} \cdots |vac\rangle, \tag{2.8}$$

where $|vac\rangle \equiv |0, 0, ..., 0\rangle$ denotes the vacuum state in which there is no particle present. The commutation relations of the operators $\hat{a}_j$ are of bosonic nature:

$$\left[\hat{a}_i, \hat{a}_j\right] = 0; \qquad \left[\hat{a}_i^\dagger, \hat{a}_j^\dagger\right] = 0; \qquad \left[\hat{a}_i, \hat{a}_j^\dagger\right] = \delta_{ij}. \tag{2.9}$$

With this, the description of a general basis set of a many-boson system with constant particle number is complete. Section 2.1.1.1 covers how to transform the set of single-particle states building up the permanent given in Eq. (2.8).

2.1.1.1 Unitary Tranformations of Permanents

Usually, unitary transformations are specified on the boson creation and annihilation operators. This paragraph closely follows the considerations made in Refs. [6, 7]. An M-mode Fock state is considered,

$$|\vec{n}\rangle = |n_1, n_2, ..., n_M\rangle = \frac{1}{\sqrt{n_1! n_2! \cdots n_M!}} \left(\hat{a}_1^\dagger\right)^{n_1} \left(\hat{a}_2^\dagger\right)^{n_2} \cdots \left(\hat{a}_M^\dagger\right)^{n_M} |vac\rangle. \tag{2.10}$$

If the following (unitary) transformation to the $\{\hat{a}_k^\dagger; k = 1, ..., M\}$ is applied:

$$\hat{a}_i^\dagger \to \tilde{\hat{a}}_i^\dagger = \sum_{k=1}^{M} U_{ki} \hat{a}_k^\dagger. \tag{2.11}$$

In general, the matrix elements of U_{ki} are given by the overlap integrals of the new basis with the old single-particle basis functions $\{\phi_k, k = 1, ..., M\}$ and $\{\tilde{\phi}_i, i = 1, ..., M\}$. The action of $\mathbf{U}$ on a single permanent Fock state is then

$$\begin{aligned} \mathbf{U}|\vec{n}\rangle &= \widetilde{|\vec{n}\rangle} &(2.12)\\ &= \prod_{i=1}^{M} \left[(n_i!)^{-\frac{1}{2}} \left(\sum_{k_i=1}^{M} U_{k_i i} \hat{a}_{k_i}^\dagger \right)^{n_i} \right] |vac\rangle. &(2.13) \end{aligned}$$

To process this result further, it lies at hand to use the multinomial expansion theorem for the multinomials $\left(\sum_{k_i=1}^{M} U_{k_i i} \hat{a}_{k_i}^\dagger\right)^{n_i}$. The resulting expression reads:

$$\widetilde{|\vec{n}\rangle} = \sum_{\substack{\{n_{ij}\} \\ \sum_{j=1}^{M} n_{ij} = n_i}} \frac{\left(\prod_{i=1}^{M} n_i!\right)^{\frac{1}{2}}}{\prod_{i,j=1}^{M} n_{ij}!} \prod_{\kappa=1}^{M} \left[\prod_{j_\kappa=1}^{M} \left(U_{j_\kappa \kappa} \hat{a}_{j_\kappa}^\dagger \right)^{n_{\kappa j_\kappa}} \right] |vac\rangle. \tag{2.14}$$

For convenience, an integer M-by-M matrix n_{ij} was introduced, whose elements fulfill the constraints that the sum of all its columns are equal to the occupations in the original Fock state $|\vec{n}\rangle$, i.e., $\sum_{j=1}^{M} n_{ij} = n_i$. Labeling the row sums of n_{ij} by m_j, i.e., $\sum_{i=1}^{M} n_{ij} = m_j$, one can rewrite the Fock vector on the right-hand side of the above expression as follows:

$$\widetilde{|\vec{n}\rangle} = \sum_{\substack{\{n_{ij}\} \\ \sum_{j=1}^{M} n_{ij} = n_i}} \frac{\left(\prod_{i=1}^{M} n_i!\right)^{\frac{1}{2}}}{\prod_{i,j=1}^{M} n_{ij}!} \left(\prod_{l=1}^{M} m_l! \right)^{\frac{1}{2}} \left(\prod_{k,l=1}^{M} U_{lk} \right)^{n_{kl}} |m_1, ..., m_M\rangle. \tag{2.15}$$

Now, the sum over all the products of the powers $U_{lk}^{n_{kl}}$, for all possible matrices n_{ij}, can be written as a permanent of a specific N-by-N matrix $\mathbf{U}\,[n_1, ..., n_M|m_1, ..., m_M]$. Its entries are taken from the transformation matrix U_{qs} as follows: the row index of U_{qs} appears n_q times and the column index appears m_s times. Furthermore, it is convenient to use the vector notation for the $m_i, i = 1, ..., M$, too, i.e., $|\vec{m}\rangle = |m_1, ..., m_M\rangle$. Consequently, $\mathbf{U}\,[n_1, ..., n_M|m_1, ..., m_M] = \mathbf{U}\left[\vec{n}|\vec{m}\right]$. Finally, denoting with $\mathrm{Per}(\cdot)$ the permanent of a matrix, one arrives at a compact expression,

$$\mathbf{U}|\vec{n}\rangle = |\widetilde{\vec{n}}\rangle = \sum_{\{\vec{m}\}} \prod_{i=1}^{M} \sqrt{m_i! n_i!} \;\; \mathrm{Per}\left(\mathbf{U}\left[\vec{n}|\vec{m}\right]\right) \quad |\vec{m}\rangle, \tag{2.16}$$

where, the sum runs on all possible distributions of N particles in M orbitals, $\{\vec{m}\}$. It is noteworthy to mention that the unitary transform of a single configuration will have contributions to all possible configurations in the new basis set. It is, therefore, intimately related to the multiconfigurational expansion which will be used frequently later on. Moreover, Eq. (2.16) makes evident the connection between unitary transformations of many-body states of bosons and the computation of permanents and shows, thus, the big complexity of such a transformation [6, 7].

For the sake of completeness and its possible later use, the unitary transformation for multiconfigurational states, i.e., $|\Psi\rangle = \sum_{\{\vec{n}\}} C_{\vec{n}} |\vec{n}\rangle$ is specified here:

$$\mathbf{U}|\Psi\rangle = \mathbf{U} \sum_{\{\vec{n}\}} C_{\vec{n}} |\vec{n}\rangle = \sum_{\{\vec{n}\}} C_{\vec{n}} \mathbf{U} |\vec{n}\rangle. \tag{2.17}$$

The unitary transformation is applied to each configuration, respectively. Now, $\mathbf{U}|\vec{n}\rangle$ can be replaced by Eq. (2.16):

$$\mathbf{U} \sum_{\{\vec{n}\}} C_{\vec{n}} |\vec{n}\rangle = \sum_{\{\vec{n}\}} C_{\vec{n}} \sum_{\{\vec{m}\}} \prod_{i=1}^{M} \sqrt{m_i! n_i!} \;\; \mathrm{Per}\left(\mathbf{U}\left[\vec{n}|\vec{m}\right]\right) \quad |\vec{m}\rangle. \tag{2.18}$$

A few remarks should be made here. The general unitary transform of a *single* permanent, as specified in Eq. (2.16), contributes to *all other possible* configurations, and it is hence already a quite complicated object. Note that the time-evolution operator $e^{-i\hat{H}t}$ of a given Hamiltonian is a unitary transformation. By writing down the unitary transform in Eq. (2.16) one, thus, arrives at the conclusion that *the only way* to properly account for the time-evolution of a system is by using a multiconfigurational wave function. To continue, it is indicated to define some useful operators and their expectation values.

2.1.1.2 One-Body Operators

In general, a sum of one-body operators $\hat{t}$ in second quantization takes the form

$$T = \sum_i \hat{t}_i = \sum_{i,j} t_{ij}\hat{a}_i^\dagger \hat{a}_j; \tag{2.19}$$
$$\text{where} \qquad t_{ij} = \langle i|\hat{t}|j\rangle.$$

Often occurring examples of one-body operators are the occupation number operator,

$$\hat{n}_i = a_i^\dagger a_i; \qquad \hat{n}_i|..., n_i, ...\rangle = n_i|..., n_i, ...\rangle,$$

the particle number operator, $\hat{N} = \sum_i \hat{n}_i$, the kinetic energy $\hat{T}$, or the potential $\hat{V}$.

2.1.1.3 Two-Body Operators

In second quantization the sum of two-body operators $\hat{W} = \frac{1}{2}\sum_{a\neq b} w(\vec{r}_a, \vec{r}_b)$ takes the form

$$\hat{W} = \frac{1}{2}\sum_{i,j,k,l} \hat{a}_i^\dagger \hat{a}_j^\dagger \hat{a}_k \hat{a}_l w_{ijkl}; \tag{2.20}$$
$$\text{where} \qquad w_{ijkl} = \langle i, j|\hat{w}|k, l\rangle = \int d\vec{r}_a \int d\vec{r}_b \phi_i^*(\vec{r}_a)\phi_j^*(\vec{r}_b) w(\vec{r}_a, \vec{r}_b)\phi_k(\vec{r}_a)\phi_l(\vec{r}_b).$$

An example of this is the two-body interaction occurring in Eq. (2.1) and its simplest form $\hat{w}(\vec{r}_i, \vec{r}_j) = \lambda_0 \delta(\vec{r}_i - \vec{r}_j)$.

2.1.1.4 Field Operators

It is often useful to have operators $\hat{\Psi}(\vec{r}, t)$ $[\hat{\Psi}^\dagger(\vec{r}, t)]$ which create [annihilate] a particle at position $\vec{r}$, i.e., in the state $|\vec{r}\rangle$. These are called field operators and read:

$$\hat{\Psi}^\dagger(\vec{r}) = \sum_i \phi_i^*(\vec{r})\hat{a}_i^\dagger; \qquad \hat{\Psi}(\vec{r}) = \sum_i \phi_i(\vec{r})\hat{a}_i. \tag{2.21}$$

To simplify the reading, the time-dependency of the field operators will be omitted where appropriate. They obey the usual bosonic commutation relations, just like the operators $\hat{a}_i, \hat{a}_j^\dagger$, and can be used to rewrite, among others, the operator for particle density $\hat{n}(\vec{r}) = \sum_{i=1}^N \delta(\vec{r} - \vec{r}_i)$ as $\hat{n}(\vec{r}) = \hat{\Psi}^\dagger(\vec{r})\hat{\Psi}(\vec{r})$. The Hamiltonian in Eq. (2.2) expressed with field operators results in

$$\hat{H} = \int d\vec{r} \left(\frac{\hbar^2}{2} \nabla \hat{\Psi}^\dagger(\vec{r}) \nabla \hat{\Psi}(\vec{r}) + V(\vec{r}, t) \hat{\Psi}^\dagger(\vec{r}) \hat{\Psi}(\vec{r}) \right) \\ + \frac{1}{2} \int d\vec{r} \int d\vec{r}' \hat{W}(\vec{r}, \vec{r}', t) \hat{\Psi}^\dagger(\vec{r}) \hat{\Psi}^\dagger(\vec{r}') \hat{\Psi}(\vec{r}) \hat{\Psi}(\vec{r}'). \tag{2.22}$$

For more details, the reader is referred to Ref. [2] and References therein. With this subsection all the necessary second quantization notations and concepts have been introduced. To continue, it is now appropriate to introduce the quantum many-body measures and analysis techniques which are important throughout this work.

2.1.2 Quantities of Interest

The scope of this subsection is to equip the reader with the analysis methods and viewpoint applied throughout this thesis and also place their development in a broader context. Since the prediction of BEC in 1924 (Refs. [8, 9]) some attention was devoted to the quantum mechanical condensation of bosonic particles in the lowest possible single-particle level. In 1956 Penrose and Onsager (Ref. [10]) were concerned with the presence of BEC in superfluid Helium and found a rigorous definition for condensation in quantum systems: a quantum system is condensed, when its reduced one-body density matrix (1-RDM) has a single macroscopic eigenvalue. In recent developments and experiments on BEC it turned out that *fragmentation* (see e.g. Refs. [11–19]) may occur. Fragmentation is defined as the situation where *several* eigenfunctions of the 1-RDM are macroscopically populated. The occurrence of fragmentation is ubiquitous especially in dynamical scenarios.The quantum mechanical description of condensation and fragmentation with the eigenvalues of the 1-RDM is intimately related to Glauber's quantum theory of optical coherence, starting in the 1960s (see Refs. [20–22]). It has been shown, that it is fully equivalent to have complete condensation and full coherence: when the single eigenvalue of the 1-RDM is N then all the normalized correlation functions are constant for all space and time [11, 22]. The systems considered in this thesis are initially confined and coherent systems that are decaying by tunneling through a barrier. Hence, it is instructive to introduce here also some measures which are especially adapted to quantify and assess the dynamics in these processes. The survival or nonescape probability of a decaying many-body quantum system can be defined as an integral either on the one-body density or on the full wave function.

The introduction and definition of the mentioned quantities are done in the following paragraphs. Further quantities, like the so-called particle loss and the principle of *local fragmentation* are deferred to the Appendices A and B (this is due to their complexity and because these quantities have yet to be implemented in the MCTDHB package [23]). Local fragmentation and the expectation values of particle loss operators can in principle be used to improve the detail of the investigation on the many-body mechanism of the tunneling process also locally.

2.1.2.1 Reduced Density Matrices

The p-particle reduced density matrix of a system (p-RDM), $\rho^{(p)}$, is defined by tracing $N-p$ coordinates from the N-particle density , $|\Psi\rangle\langle\Psi|$:

$$\begin{aligned}\rho^{(p)}(\vec{r}_1, ..., \vec{r}_p|\vec{r}_1', ..., \vec{r}_p'; t) &= Tr_{\vec{r}_{p+1}\cdots\vec{r}_N}\left[|\Psi\rangle\langle\Psi|\right] \\ &= \frac{N!}{(N-p)!}\int d\vec{r}_{p+1}\cdots d\vec{r}_N \Psi(\vec{r}_1, ..., \vec{r}_N, t) \\ &\quad \Psi^*(\vec{r}_1', ..., \vec{r}_p', \vec{r}_{p+1}, ..., \vec{r}_N, t).\end{aligned} \tag{2.23}$$

The second line illustrates the action of the trace operation $Tr[\cdot]$. The 1-RDM plays a special role for the definition of condensation and fragmentation, as well as for the analysis of bosonic systems:

$$\rho^{(1)}(\vec{r}_1|\vec{r}_1'; t) = \frac{N!}{(N-1)!}\int d\vec{r}_2\cdots d\vec{r}_N \Psi(\vec{r}_1, ..., \vec{r}_N, t)\Psi^*(\vec{r}_1', \vec{r}_2, ..., \vec{r}_N, t). \tag{2.24}$$

Similar to the above Eq. (2.24), the RDMs can also be obtained in momentum representation. When the starting point is a many-boson wave function specified in momentum space, the RDMs are simply obtained by replacing $\vec{r}$s with $\vec{k}$s in the above Equations (2.23) and (2.24). This holds also for the quantities computed from the RDMs, which are discussed in the next three paragraphs, i.e., the one-body density, natural occupations/orbitals, and normalized correlation functions.

2.1.2.2 The One-Body Density

Probably the most analyzed and the most intuitive quantity to look at in a quantum system is the one-body density. This is simply the diagonal of the 1-RDM of Eq. (2.24):

$$\begin{aligned}\rho(\vec{r}, t) &\equiv \rho(\vec{r}_1 = \vec{r}|\vec{r}_1' = \vec{r}; t) \\ &= \frac{N!}{(N-1)!}\int d\vec{r}_2\cdots d\vec{r}_N \Psi(\vec{r}, ..., \vec{r}_N, t)\Psi^*(\vec{r}, \vec{r}_2, ..., \vec{r}_N, t).\end{aligned} \tag{2.25}$$

From a probabilistic point of view, it can be interpreted as the probability to find one particle at position $\vec{r}$, while the remaining are *somewhere in space*.

2.1.2.3 Natural Occupation Numbers and Natural Orbitals

One of the key measures to assess the degree of condensation and coherence or, complementarily, fragmentation and incoherence, is the diagonal representation of the 1-RDM in Eq. (2.24):

$$\rho^{(1)}(\vec{r}_1|\vec{r}_1';t) = \sum_{k,q=1}^{M} \rho_{kq}(t)\phi_k^*(\vec{r}_1',t)\phi_q(\vec{r}_1,t)$$
$$= \sum_{i=1}^{M} \rho_i^{(NO)}(t)\phi_i^{*(NO)}(\vec{r}_1',t)\phi_i^{(NO)}(\vec{r}_1,t). \tag{2.26}$$

In first equality the 1-RDM or any arbitrary function is expanded in a suitable basis set $\{\phi_i, i = 1, ..., M\}$. The $\rho_{kq}(t)$ are termed one-body matrix elements. In the second equality, one simply diagonalizes the $\rho_{kq}(t)$ matrix to achieve the simplest possible representation of the 1-RDM. The corresponding basis set, $\{\phi_i^{(NO)}, i = 1, ..., M\}$, is termed natural orbitals and their weights, $\rho_i^{(NO)}(t)$ are termed natural occupations. The $\{\rho_i^{(NO)}(t), i = 1, ..., M\}$ and $\{\phi_i^{(NO)}, i = 1, ..., M\}$ are the eigenvalues and eigenfunctions of the 1-RDM, respectively.

2.1.2.4 Normalized Correlation Functions

The normalized $p-$particle correlation function, $g^{(p)}$, is defined by the relation of the p-RDM, see Eq. (2.23), to the diagonals of the 1-RDM at the p different coordinates (see Refs. [20–22, 24]):

$$g^{(p)}(\vec{r}_1', ..., \vec{r}_p', \vec{r}_1, ..., \vec{r}_p; t) = \frac{\rho^{(p)}(\vec{r}_1, ..., \vec{r}_p|\vec{r}_1', ..., \vec{r}_p'; t)}{\sqrt{\prod_{i=1}^{p} \rho_1(\vec{r}_i|\vec{r}_i; t)\rho_1(\vec{r}_i'|\vec{r}_i'; t)}}. \tag{2.27}$$

Coherence of p-th order is achieved, if $g^{(p)} = 1$ holds. It is straightforward to see that this holds only if the p-RDM is a product of 1-RDMs [20]. This is the case if the 1-RDM can be represented by a single complex-valued function, which, in turn, means that the 1-RDM has a single eigenvalue. Therefore, this 1-RDM corresponds to a fully condensed system. From a probabilistic point of view $g^{(p)}$ measures the degree of statistical dependence of the simultaneous measurement of a set of p coordinates $\vec{r}_1, ..., \vec{r}_p$. If $g^{(p)} = 1$ then the measurement of the p coordinates is statistically independent and, consequently, the positions of the particles are not correlated. In this case it is said that the system is p-th order coherent. Full coherence can only be reached for $p = 1$. In the case of big particle numbers and $p \ll N$, the maximally achievable p-th order coherence is $1 + \mathcal{O}(N^{-1})$ [20, 24]. In the case of $g^{(p)} > 1$ the measurement of the p positions is correlated and in the case of $g^{(p)} < 1$ it is anticorrelated. In this respect, coherence comes with condensation and correlation/anticorrelation comes with fragmentation. Of course, the equivalent p-th order normalized correlation functions can be obtained also in momentum space from the p-RDMs in momentum space.

2.1.2.5 The Nonescape Probability

Tunneling processes occur in potentials that have regions separated by a barrier which is higher than the energy of the considered system. Usually, the initial state is localized on one side of this barrier with a probability almost equal to one. During its time evolution the system is eventually no longer localized on one side of the barrier. There are two ways to measure the survival or nonescape probability of the state in question. One can integrate either the one-body density or the full wave function in the part of space Ω where the state is initially localized. This integration defines the density-related and the wave function-related nonescape probabilities, $P_{not,\rho}(t)$ and $P_{not,\Psi}(t)$, respectively:

$$P_{not,\rho}(t) = \int_\Omega \rho(\vec{r},t)d\vec{r}, \tag{2.28}$$

$$P_{not,\Psi}(t) = \int_\Omega \Psi^*(\vec{r}_1,...,\vec{r}_N)\Psi(\vec{r}_1,...,\vec{r}_N)d\vec{r}_1\cdots d\vec{r}_N. \tag{2.29}$$

$P_{not,\rho}(t)$ measures the nonescape probability on the level of single particles, whereas $P_{not,\Psi}(t)$ measures the nonescape probability on the N-particle level. For non-interacting particles, the relation $P_{not,\rho}(t) \propto \sqrt[N]{P_{not,\Psi}(t)}$ is obvious. Additionally, it is reasonable to expect that $P_{not,\Psi}(t)$ is proportional to the autocorrelation function $c(t) = \langle\Psi(t=0)|\Psi(t)\rangle$. This at least holds in the case of open systems, where $P_{not,\Psi}(t)$ and $c(t)$ are monotonously decreasing functions. One can formulate the nonescape probabilities discussed in this paragraph also in relation to the so-called particle loss operators (see Appendix A).

2.2 Theoretical Methods Employing the Full Many-Boson Hamiltonian

2.2.1 The Time-Dependent Variational Principle

The derivation of the TDGP, BMF, and of the MCTDHB is done by tackling the full many-boson Schrödinger equation with the time-dependent variational principle (TDVP) using different ansatzes. To motivate and place the following introduction to these methods on a solid ground, it is instructive to review briefly the TDVP as given in Ref. [25]. The basic idea is that the action functional $\mathcal{S}$ is minimized by the actual time-evolution taken by the system. Hence,

$$\delta\mathcal{S} \overset{!}{=} 0. \tag{2.30}$$

The action $\mathcal{S}$ is the time-integral of the Lagrangian of the considered system described by a set of so-called generalized coordinates. For a quantum mechanical (many-body) system, having a constant particle number and and a Hermitian operator $i\partial_t$, the Lagrangian takes the form:

$$\mathcal{L}(\Psi(t), \Psi^*(t)) = \langle \Psi(t) | i\partial_t - \hat{H} | \Psi(t) \rangle. \tag{2.31}$$

Consequently, requiring the action to be stationary results in demanding the following expression to vanish:

$$\delta \mathcal{S}\left[\Psi(t), \Psi^*(t)\right] = \delta \int_{t_1}^{t_2} \mathcal{L}(\Psi(t), \Psi^*(t)) dt \tag{2.32}$$

$$= \delta \int_{t_1}^{t_2} \langle \Psi(t) | i\partial_t - \hat{H} | \Psi \rangle \overset{!}{=} 0. \tag{2.33}$$

It is possible with this machinery to derive the equations of motion for any wisely or unwisely chosen *generalized coordinates* Ψ and Ψ^*. Kramer and Saraceno aptly described this issue in Ref. [25], on p. 6:

> "As is well-known, a variational principle is a blind and dumb procedure that always provides an answer, but it's accuracy depends crucially on the choice of the trial function."

In what follows, the quest for a more and more accurate variational description in terms of improvement of the ansatz for the trial function (wave function) Ψ for many-boson systems is presented and discussed.

2.2.2 *The Time-Dependent Gross–Pitaevskii Equation*

The main working tool for the description of the physics of ultracold bosons and BEC is the famous and successful time-dependent Gross–Pitaevskii equation (see Refs. [1, 26] and the References therein). Phenomenologically, it was the natural first step taken to understand the quantum physics of the TDSE, Eq. (2.1), with the many-boson Hamiltonian, Eq. (2.2), using the TDVP. The starting point to obtain the TDGP is to use a contact interparticle potential, $\hat{W}(\vec{r}, \vec{r}\,') = \lambda_0 \delta(\vec{r} - \vec{r}\,')$. In order to cover the phenomenology of BEC, one assumes that all bosons occupy only one quantum mechanical single-particle state. This implies the truncation of the field operator, Eq. (2.21), to a single time-dependent mode function $\Phi(\vec{r}, t)$:

$$\hat{\Psi}(\vec{r}, t) \equiv \Phi(\vec{r}, t) \hat{b}(t). \tag{2.34}$$

From this, the (single) boson creation operator,

$$\hat{b}(t) = \int \Phi^*(\vec{r}, t) \hat{\Psi}(\vec{r}, t) d\vec{r}, \tag{2.35}$$

is defined. As a result, the GP many-boson wave function is a product state,

$$|\Psi(t)\rangle = \frac{1}{\sqrt{N!}}\left(\hat{b}^{\dagger}(t)\right)^{N}|vac\rangle = |N, 0, ...; t\rangle = \frac{1}{\sqrt{N!}}\prod_{i=1}^{N}\Phi(\vec{r}_i, t). \qquad (2.36)$$

The expectation value of $i\partial_t - \hat{H}$ then reads

$$\langle\Psi|i\partial_t - \hat{H}|\Psi\rangle = -N\int d\vec{r}\{\Phi^*(\vec{r}, t)\hat{h}\Phi(\vec{r}, t) + \frac{(N-1)}{2}\lambda_0|\Phi(\vec{r}, t)|^4\} + \langle\Psi|i\partial_t|\Psi\rangle \qquad (2.37)$$

Plugging this ansatz, Eq. (2.37), in the action functional, Eq. (2.33), and requiring the latter to be stationary, results in the following Equation:

$$\frac{\delta\mathcal{S}\left[\Phi(\vec{r}, t)\right]}{\delta\Phi^*(\vec{r}, t)} = 0 \quad \rightarrow \quad i\partial_t\Phi(\vec{r}, t) = \left[\hat{h} + \lambda_0(N-1)|\Phi(\vec{r}, t)|^2\right]\Phi(\vec{r}, t). \qquad (2.38)$$

Equation (2.38) describes the dynamics of interacting bosons which are *completely condensed* into a single particle state and is referred to as the time-dependent Gross–Pitaevskii equation.

2.2.3 *Best Mean-Field*

The straightforward generalization of the GP ansatz for the many-boson wave function is simply to allow the bosons to occupy M, instead of one, single particle states. This permits the description of *single-configurational* condensed *or* fragmented quantum states, given that one uses an appropriate number M of single-particle states. Here, *single-configurational* means that a single permanent, cf. Eq. (2.8), is used in the description. This section will sketch the derivation of the equations of motion of the time-dependent multi-orbital mean-field or, in short, *best mean-field* (BMF) as given in [27]. Note that there is also a time-independent version of the best mean-field for condensates, which for brevity is not presented here (see Ref. [28]). The ansatz for the time-dependent best mean-field with M orbitals reads:

$$\Phi(\vec{r}_1, \vec{r}_2, ..., \vec{r}_N, t) = \hat{\mathcal{S}}\Big[\underbrace{(\phi_1(\vec{r}_1, t)\phi_1(\vec{r}_2, t)\cdots)}_{n_1 \text{ times}}\underbrace{(\phi_2(\vec{r}_{n_1+1}, t)\phi_2(\vec{r}_{n_1+2}, t)\cdots)}_{n_2 \text{ times}}\cdots \underbrace{(\phi_M(\vec{r}_{N-n_M+1}, t)\phi_M(\vec{r}_{N-n_M+2}, t)\cdots)}_{n_M \text{ times}}\Big], \qquad (2.39)$$

where $\hat{\mathcal{S}}$ is a symmetrization operator. In the second quantization formalism, the above Eq. (2.39) reads:

$$|\Phi\rangle = |n_1, n_2, ..., n_M; t\rangle.$$

As in the previous derivation of the TDGP, the TDVP is used to obtain equations of motion (EOMs) for the variational parameters $\phi_1(\vec{r},t)$, ..., $\phi_M(\vec{r},t)$. Obviously, the TDGP is recovered in the case of $M = 1$ in Eq. (2.39). The functional action is given as

$$S = \int dt \left[\langle \Phi | \hat{H} - i\partial_t | \Phi \rangle - \sum_{k=1,j=1}^{M} \mu_{kj}(t) \left[\langle \phi_k | \phi_j \rangle - \delta_{kj} \right] \right], \tag{2.40}$$

where μ_{kj} are Lagrange multipliers to ensure the orthonormality of the time-evolution of the orbitals ϕ_k and ϕ_j. For convenience, the time-dependencies will be omitted in the following where they are not explicitly needed. It is convenient to define:

$$\begin{aligned}
h_{kj} &= \int \phi_k^*(\vec{r}) \hat{h}(\vec{r}) \phi_j(\vec{r}) d\vec{r}, \\
(i\partial_t)_{kj} &= \int \phi_k^*(\vec{r}) \left(i\partial_t\right) \phi_j(\vec{r}) d\vec{r} \\
&= \int \phi_k^*(\vec{r}) \dot{\phi}_j(\vec{r}) d\vec{r}, \\
W_{kjql} &= \int\int \phi_k^*(\vec{r}) \phi_j^*(\vec{r}\,') W(\vec{r}-\vec{r}\,') \phi_q(\vec{r}) \phi_l(\vec{r}\,') d\vec{r} d\vec{r}\,', \\
W_{kj[ql]} &= W_{kjql} + W_{kjlq}, \\
\hat{J}_l(\vec{r}) &= \int \phi_l^*(\vec{r}) W(\vec{r}-\vec{r}\,') \phi_l(\vec{r}\,') d\vec{r}\,', \\
\hat{K}_l(\vec{r}) &= \int \phi_l^*(\vec{r}) W(\vec{r}-\vec{r}\,') \mathcal{P}_{\vec{r}\vec{r}\,'} \phi_l(\vec{r}\,') d\vec{r}\,', \\
\boldsymbol{P} &= \mathbf{1} - \sum_{i=1}^{M} |\phi_i\rangle\langle\phi_i|.
\end{aligned} \tag{2.41}$$

Here, $\mathcal{P}_{\vec{r}\vec{r}\,'}$ swaps $\vec{r}$ with $\vec{r}\,'$ in the expression on its right side. By demanding the action to be stationary when varying the parameters in the ansatz, $\{\frac{\delta S}{\delta\phi_j^*(\vec{r},t)} \overset{!}{=} 0, j = 1, ..., M\}$ one gets (after the elimination of the Lagrange multipliers) the following EOMs for the BMF:

$$\boldsymbol{P} i |\dot{\phi}_k\rangle = \boldsymbol{P} \left[\hat{h} + \lambda_0 (n_k - 1) \hat{J}_k + \sum_{l \neq k}^{M} \lambda_0 n_l (\hat{J}_l + \hat{K}_l) \right] |\phi_k\rangle. \tag{2.42}$$

These EOMs are a coupled set of non-linear integro-differential equations. The details of their derivation, as well as illustrative numerical examples can be found in Refs. [14, 15, 27–29]. In physical situations that are fully described by a single configuration, i.e., one permanent, the BMF theory is a good approach. Note that any initial set of occupations, n_1, ..., n_M, will remain unchanged by the time-evolution under Eq. (2.42). This means that the BMF theory lacks the capability of describing processes in which the many-boson system under consideration undergoes fragmentation or condensation, because the occupation numbers, $n_1, n_2, ..., n_M$, cannot change. The MCTDHB circumvents this flaw of the BMF and will be the topic of Sect. 2.2.4

2.2.4 *The Multiconfigurational Time-Dependent Hartree Method for Bosons*

The natural generalization of the BMF towards a better description of the full Hilbert space of the many-boson system is to consider not only a *single configuration* (see Eqs. (2.39), (2.8)) but, instead, *many configurations*, i.e., all possible configurations that can be formed from a set of M single-particle states. The method thus becomes *multiconfigurational* and, as the time-dependent configurations and derivation come from the Hartree method, its name is the multiconfigurational time-dependent Hartree method for bosons (MCTDHB). There is a wealth of multiconfigurational Hartree theories for mixtures of different species of bosons and fermions, see Refs. [30, 31], with particle conversion and up to three-body interactions. The following introduction considers and sketches only the single-species version as given in Ref. [32, 33] because this version will be amply used, benchmarked with analytical results, and compared with other methods in the field throughout the present work. It is instructive to start from the field operator expanded in the basis of a set of M orthonormal, time-dependent functions (orbitals), $\{\phi_k(\vec{r}, t), k = 1, ..., M\}$:

$$\begin{aligned} \hat{b}_k(t) &= \int \phi_k^*(\vec{r}, t)\hat{\Psi}(\vec{r})d\vec{r}; \qquad k = 1, ..., M, \\ \hat{\Psi}(\vec{r}) &= \sum_k^M \hat{b}_k(t)\phi_k^*(\vec{r}, t). \end{aligned} \tag{2.43}$$

This is the bosonic field operator. The *only* approximation introduced here, is the assumption that the set of M orbitals is sufficient to describe the Hilbert space occupied by the many-boson wave function. Using the $\hat{b}_k(t)$, their commutation relations, $\hat{b}_k(t)\hat{b}_j^\dagger(t) - \hat{b}_j^\dagger(t)\hat{b}_k = \delta_{kj}$, and the abbreviation $\vec{n} = (n_1, n_2, ..., n_M)$, one arrives at the ansatz for the variational derivation of the MCTDHB EOMs:

$$\begin{aligned} |\Psi(t)\rangle &= \sum_{\{\vec{n}\}} C_{\vec{n}}(t)|\vec{n}; t\rangle \qquad (2.44) \\ &= \sum_{\{(n_1,...,n_M)\}} \frac{C_{(n_1,...,n_M)}(t)}{\sqrt{n_1! \cdots n_M!}} \left(\hat{b}_1^\dagger(t)\right)^{n_1} \cdots \left(\hat{b}_M^\dagger(t)\right)^{n_M} |vac\rangle. \end{aligned}$$

Here, $|vac\rangle$, stands for the vacuum state with no boson present and the sum runs over all $N_{conf} = \binom{N+M-1}{N}$ possible configurations, $\{(n_1, ..., n_M)\}$, of $N = \sum_{i=1}^{M} n_i$ particles occupying the M orbitals. Note that both, the coefficients $\{C_{\vec{n}}\}$ and the orbitals $\{\phi_k\}$, are *time-dependent* and both will be used as variational parameters for the following derivation of the equations of motion. Introducing Lagrange multipliers, $\mu_{kj}(t)$, ensuring the orthonormality of the orbitals (as in the BMF case, cf. Eq. (2.40)), the action functional takes the form:

$$S\left[\{C_{\vec{n}}(t)\}, \{\phi_k(\vec{r}, t)\}\right] = \int dt \left[\langle\Psi|\hat{H} - i\partial_t|\Psi\rangle - \sum_{k,j=1}^{M} \mu_{kj}(t) \left[\langle\phi_k|\phi_j\rangle - \delta_{kj}\right] \right]. \tag{2.45}$$

Now, one demands this action to be stationary when varying *all* the N_{conf} coefficients, i.e., $\frac{\delta S}{\delta C^*_{\vec{n}}(t)} \overset{!}{=} 0$ and when varying the M orbitals, i.e., $\frac{\delta S}{\delta \phi^*_k(\vec{r},t)} \overset{!}{=} 0$. The details of the derivation and how the elimination of the Lagrange multipliers results in the emergence of projectors, $\hat{\boldsymbol{P}}$, are given in Ref. [33]. The EOMs for the coefficients reads:

$$\boldsymbol{H}(t)\boldsymbol{C}(t) = i\partial_t\boldsymbol{C}(t); \qquad \boldsymbol{H}(t) = \{H_{\vec{n}\vec{n}'}(t)\} = \{\langle\vec{n}; t|\hat{H}|\vec{n}'; t\rangle\}. \tag{2.46}$$

Here $\boldsymbol{C}(t)$ collects the coefficients $\{C_{\vec{n}}(t)\}$ in a vector. On the other hand, the EOMs for the orbitals read:

$$\begin{aligned} i\partial_t|\phi_j\rangle &= \hat{\boldsymbol{P}} \left[\hat{h}|\phi_j\rangle + \sum_{k,s,q,l=1}^{M} \{\boldsymbol{\rho}(t)\}^{-1}_{jk} \rho_{ksql} \hat{W}_{sl}|\phi_q\rangle \right], \\ \hat{W}_{sl}(\vec{r}, t) &= \int \phi^*_s(\vec{r}', t)\hat{W}(\vec{r} - \vec{r}', t)\phi_l(\vec{r}', t)d\vec{r}', \\ \hat{\boldsymbol{P}} &= 1 - \sum_{i=1}^{M} |\phi_i\rangle\langle\phi_i|. \end{aligned} \tag{2.47}$$

Here $\{\boldsymbol{\rho}\}^{(-1)}$ is the inverse of the reduced one-body matrix elements, the ρ_{ksql} are the matrix elements of the reduced two-body density and the $\hat{W}_{sl}(\vec{r}, t)$ are referred to as *local time-dependent potentials*. The Eqs. (2.46), (2.47) are the core of the MCTDHB and their numerical solution is implemented in a Fortran program package, see Ref. [23], which will be described in Sect. 2.4. It is appropriate to note that the Hilbert space covered by the ansatz of the MCTDHB, Eq. (2.45), is N_{conf} times bigger than the one covered by the TDGP. Yet, one obtains back the TDGP from the MCTDHB for $M = 1$ in the above equations of motion. This could also be deduced already from the field operator, see Eq. (2.43). Extending beyond TDGP, fragmented states (up to M-fold) are described self-consistently by the MCTDHB. The dynamics of fragmentation and condensation processes, which go beyond the realm of the BMF, can be described by MCTDHB because the coefficients of the permanents which assemble the many-boson wave function are time-dependent. A benchmark of the quality and convergence properties of the MCTDHB approximation is the topic of Chap. 3.

2.3 Theoretical Methods Employing Model Hamiltonians

2.3.1 Bose–Hubbard and Time-Evolved Block Decimation

One of the most frequently used models in the field of ultracold bosons is the so-called Bose–Hubbard (BH) model. To arrive at the BH model Hamiltonian (following Ref. [34]) one assumes a periodic potential, such as $V_0(\vec{x}) = \sum_{j=1}^{3} V_{j0} \sin kx_j$, a so-called optical lattice. Furthermore, one uses the zero-range pseudopotential of Eq. (2.3). Now, a deep potential (large coefficients V_{j0}) is assumed and the field operator $\hat{\Psi}(\vec{x})$ is expanded in a Wannier basis. The Wannier functions $w_k(\vec{x} - \vec{x}_i)$ are linear combinations of Bloch waves which are localized at certain lattice sites $\vec{x}_i$. The final assumption is, that the lattice is deep and the higher Wannier functions $k \geq 2$ do not contribute. The resulting field operator reads

$$\hat{\Psi}(\vec{x}) = \sum_i \hat{b}_i w(\vec{x} - \vec{x}_i). \tag{2.48}$$

The resulting so-called BHH reads:

$$\hat{H} = -J \sum_{\{i,j\}} \hat{b}_i^\dagger \hat{b}_j + \sum_i \epsilon_i \hat{n}_i + \frac{U}{2} \sum_i \hat{n}_i (\hat{n}_i - 1). \tag{2.49}$$

Here, the following abbreviations are used:

$$J = \int d\vec{x} w^*(\vec{x} - \vec{x}_i) \hat{h}(\vec{x}) w(\vec{x} - \vec{x}_i); \tag{2.50}$$

$$U = \lambda_0 \int d\vec{x} |w(\vec{x})|^4; \tag{2.51}$$

$$\epsilon_i = \int d\vec{x} V_T(\vec{x}_i) |w(\vec{x} - \vec{x}_i)|^2. \tag{2.52}$$

Here, V_T is some additional external, slowly varying, potential leading to an energy shift, see Ref. [34]. To compute the time-evolution of the BHH an algorithm called time-evolving block decimation (TEBD) is frequently employed. TEBD works for quasi-one-dimensional systems only. Hence, the following discussion of the BHH and TEBD is restricted to one spatial dimension. TEBD relies on the idea, that one achieves a good approximation to a given pure quantum state $|\Psi\rangle$ by rewriting it as $|\Psi\rangle = \sum_{\alpha=1}^{D} \lambda_\alpha^{[l]} |\Phi_\alpha^{[1\cdots l]}\rangle |\Phi_\alpha^{[(l+1)\cdots N]}\rangle$ and restricting D to some D_ϵ [35]. Here, $|\Phi_\alpha^{[1\cdots l]}\rangle$ and $\lambda_\alpha^{[l]}$ are obtained from a Schmidt decomposition of $|\Psi\rangle$ onto subspaces containing less than the total number of particles, $l < N$ and $l - N < N$. For any l, the entries of $\lambda_\cdot^{[l]}$ are the decreasingly ordered Schmidt coefficients. The approximated state reads:

$$|\Psi\rangle = \left(\sum_{\alpha=1}^{D_\epsilon} |\lambda_\alpha^{[l]}|^2 \right)^{-\frac{1}{2}} \sum_{\alpha=1}^{D_\epsilon} \lambda_\alpha^{[l]} |\Phi_\alpha^{[1\cdots l]}\rangle |\Phi_\alpha^{[(l+1)\cdots N]}\rangle. \tag{2.53}$$

For further details see Refs. [35, 36] and References therein. For the BHH it is intuitively a good idea to make such an approximation, because there is only a direct nearest-neighbor interaction and it is a reasonable approximation to consider subsystems as uncorrelated, hence, $D_\epsilon \ll D$. This means, that the computation of the time-evolution of a state under the BHH to a quite good accuracy is cheap, depending on the D_ϵ chosen. The great achievements of these intuitive approximations, see Ref. [37] and References therein, have to be contrasted with the examples where they fail [11, 24, 38, 39]. This failure is mostly due to the incapability of the BH model to properly cover the physics of the considered system which involves higher bands or delocalized states. Such a comparison must rely on a many-body method, such as the MCTDHB, which is able to capture the rich physics beyond the BH model.

2.3.2 The Discrete Non-Linear Schrödinger Equation

In principle, the BH model is capable to describe a system of ultracold bosons which are *not* condensed. Yet, one can imagine, that in the mean-field limit it is feasible to describe the state of the system as a coherent product state. In this mean-field limit, the following assumptions are introduced:

$$N \to \infty; \qquad \frac{NU}{J} = const.; \qquad U \to 0.$$

One can derive the resulting discrete nonlinear Schrödinger equation by replacing the creation and annihilation operators $\hat{b}_i, \hat{b}_j^\dagger$ in the BHH, Eq. (2.49), by complex numbers, b_i, b_j^*. The time evolution of these numbers is then defined solely by their canonical equations of motion, cf. Ref. [40]. The result is the so-called discrete nonlinear Schrödinger equation (DNLS) which can be used to find the coherent dynamics within the BH model. It reads:

$$i\dot{b}_i = -J(b_{i+1} + b_{i-1}) + \frac{U\bar{n}}{2}|b_i|^2 b_i; \qquad \bar{n} = N/L. \tag{2.54}$$

Here $\bar{n} = N/L$ is the number of atoms per lattice site. The physical situation where this approximation to the BH model is applicable is deep optical lattices with a very weak interaction. Nevertheless, the authors of Ref. [41] benchmarked the BHH and the DNLS with each other on a tunneling problem with long-range correlations and delocalized states. It is instructive to perform a check on the validity of the predictions of this benchmark, by a comparison to numerically exact solutions of the same problem obtained with the MCTDHB method, see Chap. 4.

2.4 Numerical Methods

This section provides an overview of the numerical methods applied throughout this work. The focus is on introducing the concepts which are needed to achieve the numerical results presented in later chapters, as well as to give an overview of the current implementation and capabilities of the MCTDHB package [23].

2.4.1 The Multiconfigurational Time-Dependent Hartree for Bosons Software Package

The MCTDHB package is a collection of Fortran programs and Bash-scripts. The current organization of the code consists in two programs: the main program which performs the computation, and the analysis program to extract quantities of interest from the results of a computation.

2.4.1.1 Current Implementation

The current implementation of the MCTDHB package is mostly in FORTRAN 90/95. It has two main parts: a hybridly parallel one for solving the TDSE and one to analyze the many-body properties of the solutions. As discussed in Sect. 2.2.4, MCTDHB is simply a reformulation of the TDSE of many-boson systems into two sets of coupled partial differential equations. To solve the two sets, i.e., the coefficient EOMs and the orbital EOMs, numerical solvers for partial differential equations have been implemented. Namely, the coefficient EOMs are solved with a Krylov subspace method: the short iterative Lanczos (SIL) integrator. Various numerical integrators for the orbital EOMs are available: the 16th order Bullirsch–Stoer method, a Runge–Kutta method of 5th/8th order and an Adams–Bashforth–Moulton predictor–corrector integrator (ABM) of $7th$ order are the implicit methods available – they work well in the case that the orbital EOMs are not stiff. For the case of dominating non-linearity, i.e., stiff orbital EOMs, the so-called ZVODE integrator [42], an implementation of a Gear- type second order backwards differentiation formula (BDF) was chosen.

2.4.1.2 Integrators

The scope of this subsection is to introduce the integrators implemented in the current version of the MCTDHB package and provide the peculiarities of it as well as its specifications. The documentation of most of the integrators is available in the Heidelberg multiconfigurational time-dependent Hartree (MCTDH) package documentation and References therein, see Ref. [43]. The focus here is on the integrators either not provided in the MCTDH package, either the ones which rely on a different implementation, namely, the SIL, the ABM and the BDF. For the details on the other numerical integrators the reader is referred to Ref. [44] and the References therein.

2.4.1.3 The Short Iterative Lanczos

To build the Krylov basis which is needed for the SIL algorithm, one has to apply powers of the Hamiltonian $\hat{H}^k$ depending on the order $k+1$ of the method, to the state vector of the coefficients. The action of the Hamiltonian is computationally the most demanding part in the SIL algorithm and therefore the part which is parallelized. This evaluation can be extremely efficiently done according to the scheme described in Ref. [45]. As soon as the basis of the Krylov subspace is constructed, the problem of the computation of the time-evolution of the coefficient vector is reduced to the diagonalization of the SIL matrix, i.e., a $(k+1) \times (k+1)$ matrix, which is done with a LAPACK routine [46]. The advantage of the SIL algorithm is that it is generally very stable when the ground state or a propagation with high accuracy are desired. Yet, in the case of degeneracies or the computation of excited states more advanced numerical techniques are needed, such as the Arnoldi or Davidson methods, see Ref. [43].

2.4.1.4 The Adams–Bashforth–Moulton Predictor–Corrector Integrator

The ABM implementation in the MCTDHB package is in principle identical to the one in the MCTDH package [43], but it is parallelized using OpenMP. The ABM algorithm is a multistep method, which relies on a polynomial extrapolation of the solution of the partial differential equation tackled. The term "predictor-corrector" stands for the error control mechanism on which it relies: if the prediction of the next order is sufficiently close to the actual next order solution the integration step is accepted; it is otherwise rejected and the step size is adjusted dynamically. It turns out that the most time-consuming parts in the ABM algorithm are the evaluations of the right-hand side of the orbital EOMs and the various products of orbital vectors which have to be evaluated. The evaluation of the right-hand side of the orbital EOMs is done by a hybridly parallel scheme outlined in the following subsection. The evaluation of the products of orbital vectors is done in OpenMP parallelized loops inside the ABM routine. For large grids the evaluation time is greatly reduced by this parallelization, while for small grids the execution time spent in the integrator is negligible.

2.4.1.5 The Gear-type Second Order Backwards Differentiation Formula

In the case of strong interparticle interactions, the set of orbital EOM becomes a stiff set of partial differential equations. For stiff equations the integration schemes mentioned and/or described above become inefficient or even unstable. It was proven that in the case of stiff differential equations an implicit integrator of second order relying on a backwards differentiation formula would globally minimize the introduced error, see Ref. [44]. The essential advantage of this kind of integrator lies in its superior stability which allows for bigger step-sizes as compared to other methods in the case of stiff differential equations. ZVODE from the ODEPACK package, see e.g. [42], is an implementation of the Gear-type second order backwards differentiation scheme and the needed changes for its use in the MCTDHB package were minor. Yet, for the cases of dynamics of strongly interacting bosons, see e.g. Ref. [47], it has proven to be essential.

2.4.1.6 Parallelization

In order to provide most of the numerical results presented in this thesis, the algorithm implemented in the MCTDHB package solving the coupled sets of EOM has to be efficient enough to provide a time-evolution in a reasonable time. The only way to achieve the desired efficiency is to parallelize the algorithm by distributing the computational tasks among several computers in a network. During the development of MCTDHB, all the available platforms were mostly homogeneous clusters, in which several identical computers with multi-core processors are connected by a network of the InfiniBand or Cray Gemini II standard. Hence, the current parallelization is adapted to such platforms. Further parallelization, like the usage of GPU-computing might be of relevance for future developments, but is not part of the current package. The algorithm basically deals with two different sets of equations: a linear one for the coefficients and a non-linear one for the orbitals. Depending on the chosen setup, the overall computational effort can be dominated by the former or the latter, or it might be balanced. For each of the two sets, the solutions of the EOMs is done by integrators which need possibly many evaluations of the complicated right-hand side of the EOMs, Eqs. (2.46), (2.47). The major part of the execution time is hence spent in the evaluation of these right-hand sides. Consequently, the strategy was to parallelize this evaluation, as shown in Fig. 2.1.

Fig. 2.1 Scheme of the Parallelization of the MCTDHB Main Program

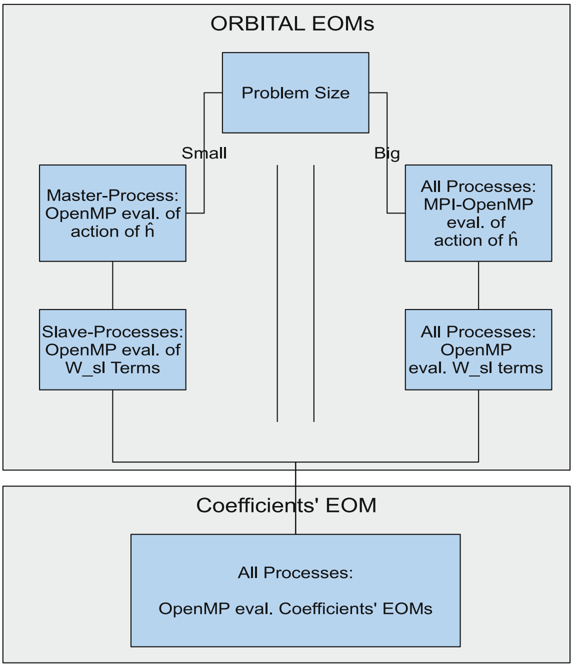

2.4.1.7 The Parallelization of the Orbital EOMs

The parallelization scheme for the orbital EOMs was done by means of a hybrid OpenMP-MPI parallel algorithm and is problem-size adaptive. In the case of rather small problems, i.e., problems with a primitive grid size of less than 1024 functions, the communication time overhead of an MPI-parallel calculation of the one-body Hamiltonian terms was dominating. Hence, it was beneficial not to communicate the needed data and use only OpenMP threads to evaluate the one-body Hamiltonian terms on the master node. The more time consuming evaluation of the two-body Hamiltonian terms is done by distributing the W_{kqsl} terms equally among the slave processes, communicate to them the needed orbital vectors and evaluate the integrals – in principle sums of point wise products of vectors – using OpenMP threads. In the case of larger problems, i.e., problems with a primitive grid size of equal to or more than 1024 functions, the evaluation of the one-body and the two-body Hamiltonian terms is distributed among all MPI-processes and done with OpenMP threads. It is appropriate here to make a remark on the scaling behavior. The number of one-body Hamiltonian terms scales with $\sim M^2$ and the number of two-body terms with $\sim M^4$. Interestingly, so far, no case occurred where the communication overhead actually dominated the benefits of the parallelization scheme implemented. Hence, the more orbitals were taken, the closer to linear the speedup was for both, large and small problem sets. In the current implementation, all the orbitals are communicated to all the MPI processes. In order to achieve the close-to-linear speedup for problems with fewer orbitals as well as to have it for problems with a *very* large number of orbitals, it would be beneficial to further optimize this communication. This optimization is achievable by determining in the initialization phase of the program which orbitals are needed for the computational tasks assigned to a particular MPI process.

2.4.1.8 The Parallelization of the Coefficient EOMs

The coefficient EOMs are propagated using the SIL algorithm described above. This renders the main part of the computation to be the application of the Hamiltonian $\hat{H}$, and its powers, for the construction of the Krylov subspace basis. The many-body basis employed in MCTDHB consists of the time-dependent Fock states with M modes at maximum. If one represents the Hamiltonian in the basis of the corresponding time-dependent creation and annihilation operators, it can be shown that each and every one-body term corresponds to a re-addressing of one element of the vector of coefficients. Similarly, each and every two-body term corresponds to a re-addressing of, at most, two elements of the vector of coefficients. With the knowledge of this re-addressing-scheme (for details, see Ref. [45]), it is no more necessary to build up a Hamiltonian matrix – the action of the Hamiltonian is available by re-addressing the elements according to the representation of the Hamiltonian in terms of the time-dependent creation and annihilation operators. Most importantly, the re-addressings needed for the $N_{1b} = \frac{M(M+1)}{2}$ one- and $N_{2b} = \frac{N_{1b}(N_{1b}+1)}{2}$ two-body operators are independent of each other. Hence, the parallelization distributes the $N_{1b} + N_{2b}$ needed re-addressings among the number of available MPI processes, where they are done with OpenMP threads. The current implementation of this scheme provides all MPI processes with a full copy of the coefficients, which might be a huge array. Therefore, the necessary communication limits the favorable scaling of this parallelization scheme to a few tens of MPI processes. Of course, this depends on the system architecture and the number of coefficients. A further improvement on this scheme would be, in principle, available by finding a suitable partitioning for the coefficients' vector. Yet, the inter-dependencies of the coefficients encoded in the re-addressing scheme are intricate and render a suitable partitioning complicated.

2.4.1.9 IMEST Algorithm

The interaction matrix evaluation by successive transforms is an efficient way to evaluate the two-body matrix elements for two-particle interaction potentials $\hat{W}(\boldsymbol{y})$, which depend only on the distance $\boldsymbol{y} = |\vec{r} - \vec{r}'|$ between the two interacting particles. The IMEST was invented by Kaspar Sakmann and the derivation here follows the one given in his Ph.D. thesis, see Ref. [48]. It is instructive to first consider the case of time-independent $\hat{W}$. For convenience, the matrix elements of the interaction and the local time-dependent potentials are repeated:

$$\begin{aligned} W_{ksql}(t) &= \int\int d\vec{r}' d\vec{r} \phi_k^*(\vec{r},t)\phi_s^*(\vec{r}',t)\hat{W}(\vec{r}-\vec{r}')\phi_q(\vec{r},t)\phi_l(\vec{r},t) \\ &= \int d\vec{r}\phi_k^*(\vec{r},t)\hat{W}_{sl}(\vec{r},t)\phi_q(\vec{r},t), \\ \hat{W}_{sl}(\vec{r},t) &= \int d\vec{r}'\phi_s^*(\vec{r}',t)\hat{W}(\vec{r}-\vec{r}')\phi_l(\vec{r}',t). \end{aligned} \tag{2.55}$$

Here, it is worthwhile to note that the evaluation of the $\hat{W}_{sl}$, as well as the evaluation of the W_{ksql}, is only a single integration on $\vec{r}'$ and $\vec{r}$, respectively. Given that the considered interaction $\hat{W}$ depends only on $\vec{r}-\vec{r}'$, one can write its Fourier and inverse Fourier transforms in the following form:

$$\hat{W}(\vec{r}-\vec{r}') = \frac{1}{\sqrt{2\pi}^D}\int d\vec{k}\tilde{\hat{W}}(\vec{k})e^{i\vec{k}(\vec{r}-\vec{r}')} \tag{2.56}$$

$$\tilde{\hat{W}}(\vec{k}) = \frac{1}{\sqrt{2\pi}^D}\int d\boldsymbol{y}\hat{W}(\boldsymbol{y})e^{-i\vec{k}\boldsymbol{y}}. \tag{2.57}$$

It is now straightforward to insert Eq. (2.56) into the above expression for $\hat{W}_{sl}$. This results in the following expression:

$$\hat{W}_{sl}(\vec{r},t) = \int d\vec{r}'\phi_s^*(\vec{r}',t)\frac{1}{\sqrt{2\pi}^D}\left[\int d\vec{k}\tilde{\hat{W}}(\vec{k})e^{i\vec{k}(\vec{r}-\vec{r}')}\right]\phi_l(\vec{r}',t). \tag{2.58}$$

Here, one can split up the exponential, $e^{i\vec{k}(\vec{r}-\vec{r}')} = e^{-i\vec{k}\vec{r}'} \cdot e^{i\vec{k}\vec{r}}$, in order to collect the terms dependent solely on $\vec{r}'$ and $\vec{k}$:

$$\hat{W}_{sl}(\vec{r},t) = \int d\vec{k}\frac{1}{\sqrt{2\pi}^D}\left[\int d\vec{r}'\phi_s^*(\vec{r}',t)\phi_l(\vec{r}',t)e^{-i\vec{k}\vec{r}'}\right]\tilde{\hat{W}}(\vec{k})e^{i\vec{k}\vec{r}}. \tag{2.59}$$

The expression in square brackets is the Fourier transform $\tilde{f}_{sl}(\vec{k})$ of the function $f_{sl}(\vec{r}',t) = \phi_s^*(\vec{r}',t)\phi_l(\vec{r}',t)$. Revisiting Equation (2.59), the integration on $\vec{k}$ can be canceled by a Fourier transform and a multiplication by $\sqrt{2\pi}^D$, giving an appealing form to the Fourier transform $\tilde{\hat{W}}_{sl}(\vec{k},t)$ of $\hat{W}_{sl}(\vec{r},t)$:

$$\begin{aligned} \tilde{\hat{W}}_{sl}(\vec{k},t) &= \frac{1}{\sqrt{2\pi}^D}\int d\vec{r}\hat{W}_{sl}(\vec{r},t)e^{-i\vec{k}\vec{r}} \\ &= \sqrt{2\pi}^D \tilde{f}_{sl}(\vec{k},t)\tilde{\hat{W}}(\vec{k}). \end{aligned} \tag{2.60}$$

Consequently, the local time-dependent potentials, occurring in the right-hand side of the orbital EOMs of the MCTDHB (cf. Eqs. (2.47), (2.46)) are available as the inverse Fourier transform of the above Eq. (2.60):

$$\hat{W}_{sl}(\vec{r},t) = \frac{1}{\sqrt{2\pi}^D} \int d\vec{k}\, \hat{\tilde{W}}_{sl}(\vec{k},t) e^{i\vec{k}\vec{r}}. \tag{2.61}$$

Equations (2.60) and (2.61) are the working equations of the IMEST. The key advantage here is that, for time-independent $\hat{W}(\vec{r},\vec{r}') = \hat{W}(\vec{r}-\vec{r}')$, it is sufficient to evaluate once the Fourier transform of the interaction potential, $\hat{\tilde{W}}(\vec{k})$ and at each time-step the Fourier transform of $f_{sl}(\vec{r},t)$, $\tilde{f}_{sl}(\vec{k},t)$, and the inverse Fourier transform of the $\hat{\tilde{W}}_{sl}(\vec{k},t)$. This is much more efficient than directly evaluating the integrals needed for the matrix elements $W_{ksql}(t)$, especially when it comes to perform computations with a large number of grid points. For details on the implementation and an assessment of the numerical effort, see Ref. [48]. For time-dependent two-body interactions, $\hat{W}(\vec{r},\vec{r}',t) = \hat{W}(\vec{r}-\vec{r}',t)$, like, e.g., the ones presented in Chap. 3, the computational effort increases because the Fourier transform of the interaction potential $\hat{\tilde{W}}$ is now also a function of time, i.e., $\hat{\tilde{W}} = \hat{\tilde{W}}(\vec{k},t)$. Therefore, it has to be evaluated at each time-step. This implies that, at each time-step, three, instead of two, additional Fourier transforms have to be evaluated. Still, the procedure is much more efficient than the direct evaluation of the integrals. The IMEST algorithm, also in its time-dependent form, were crucial for performing the calculations in Chap. 3 and for comparing the results of Chap. 6 with a zero-range potential to computations with a short-range Gaussian potential.

References

1. C.J. Pethick, H. Smith, *Bose–Einstein Condensation in Dilute Gases*. (Cambridge University Press, 2008)
2. F. Schwabl, *Quantenmechanik für Fortgeschrittene* (Springer, Heidelberg, 2000)
3. M. Olshanii, Atomic Scattering in the Presence of an External Confinement and a Gas of Impenetrable Bosons. Phys. Rev. Lett. **81**, 938 (1998)
4. M. Olshanii, L. Pricoupenko, Rigorous Approach to the Problem of Ultraviolet Divergencies in Dilute Bose Gases. Phys. Rev. Lett. **88**, 010402 (2002)
5. P.A.M. Dirac, The Quantum Theory of the Emission and Absorption of Radiation. Proc. R. Soc. Lond. A **114**, 243–265 (1927)
6. S. Scheel, S.Y. Buhmann, Macroscopic quantum electrodynamics - concepts and applications. Acta Physica Slovaca **58**, 675–809 (2008)
7. S. Scheel, Permanents in linear optical networks. arXiv:quant-ph, 0406127v1 (2004)
8. A. Einstein, Quantentheorie des einatomigen idealen Gases. Sitzungsber. Preuss. Akad. Wiss. Bericht **22**, 261 (1924)
9. A. Einstein, Quantentheorie des einatomigen idealen Gases. II. Sitzungsber. Preuss. Akad. Wiss. Bericht **1**, 3 (1925)
10. O. Penrose, L. Onsager, Bose–Einstein Condensation and Liquid Helium. Phys. Rev. **104**, 576–584 (1956)
11. K. Sakmann, A.I. Streltsov, O.E. Alon, L.S. Cederbaum, Exact Quantum Dynamics of a Bosonic Josephson Junction. Phys. Rev. Lett. **103**, 220601 (2009)
12. L.S. Cederbaum, A.I. Streltsov, O.E. Alon, Fragmented Metastable States Exist in an Attractive Bose–Einstein Condensate for Atom Numbers Well Above the Critical Number of the Gross–Pitaevskii Theory. Phys. Rev. Lett. **100**, 040402 (2008)

13. A.I. Streltsov, O.E. Alon, L.S. Cederbaum, Role of Excited States in the Splitting of a Trapped Interacting Bose–Einstein Condensate by a Time-Dependent Barrier. Phys. Rev. Lett. **99**, 030402 (2007)
14. O.E. Alon, A.I. Streltsov, L.S. Cederbaum, Zoo of Quantum Phases and Excitations of Cold Bosonic Atoms in Optical Lattices. Phys. Rev. Lett. **95**, 030405 (2005)
15. O.E. Alon, L.S. Cederbaum, Pathway from Condensation via Fragmentation to Fermionization of Cold Bosonic Systems. Phys. Rev. Lett. **95**, 140402 (2005)
16. P. Bader, U.R. Fischer, Fragmented Many-Body Ground States for Scalar Bosons in a Single Trap. Phys. Rev. Lett. **103**, 060402 (2009)
17. R.W. Spekkens, J.E. Sipe, Spatial fragmentation of a Bose–Einstein condensate in a double-well potential. Phys. Rev. A **59**, 3868–3877 (1999)
18. E.J. Mueller, T.-L. Ho, M. Ueda, G. Baym, Fragmentation of Bose–Einstein condensates. Phys. Rev. A **74**, 033612 (2006)
19. C. Weiss, Y. Castin, Creation and Detection of a Mesoscopic Gas in a Nonlocal Quantum Superposition. Phys. Rev. Lett. **102**, 010403 (2009)
20. U.M. Titulaer, R.J. Glauber, Correlation Functions for Coherent Fields. Phys. Rev. **140**, B676 (1965)
21. R.J. Glauber, The Quantum Theory of Optical Coherence. Phys. Rev. **130**, 2529 (1963)
22. M. Naraschewski, R.J. Glauber, Spatial coherence and density correlations of trapped Bose gases. Phys. Rev. A **59**, 4595 (1999)
23. A.I. Streltsov, K. Sakmann, A.U.J. Lode, O.E. Alon, L.S. Cederbaum, The Multiconfigurational time-dependent Hartree for Bosons package, version 2.3, Heidelberg, (2012), see http://mctdhb.uni-hd.de
24. K. Sakmann, A.I. Streltsov, O.E. Alon, L.S. Cederbaum, Reduced density matrices and coherence of trapped interacting bosons. Phys. Rev. A, **78**, 023615 (2008)
25. P. Kramer, M. Saraceno, *Geometry of the Time-Dependent Variational Principle* (Springer, Heidelberg, 1981)
26. L.P. Pitaevskii, S. Stringari, *Bose–Einstein Condensation* (Oxford University Press, 2003)
27. O.E. Alon, A.I. Streltsov, L.S. Cederbaum, Time-dependent multiorbital mean-field for fragmented Bose–Einstein condensates. Phys. Lett. A **362**, 453–459 (2007)
28. L.S. Cederbaum, A.I. Streltsov, Best mean-field for condensates. Phys. Lett. A **318**, 564–569 (2003)
29. L.S. Cederbaum, A.I. Streltsov, Y.B. Band, O.E. Alon, Interferences in the Density of Two Bose–Einstein Condensates Consisting of Identical or Different Atoms. Phys. Rev. Lett. **98**, 110405 (2007)
30. O.E. Alon, A.I. Streltsov, L.S. Cederbaum, Many-body theory for systems with particle conversion: Extending the multiconfigurational time-dependent Hartree method. Phys. Rev. A. **79**, 022503 (2009)
31. O.E. Alon, A.I. Streltsov, K. Sakmann, A.U.J. Lode, J. Grond, L.S. Cederbaum, Recursive formulation of the multiconfigurational time-dependent Hartree method for fermions, bosons and mixtures thereof in terms of one-body density operators. Chem. Phys. **401**, 2–14 (2012)
32. A.I. Streltsov, O.E. Alon, L.S. Cederbaum, General variational many-body theory with complete self-consistency for trapped bosonic systems. Phys. Rev. A **73**, 063626 (2006)
33. O.E. Alon, A.I. Streltsov, L.S. Cederbaum, Multiconfigurational time-dependent Hartree method for bosons: Many-body dynamics of bosonic systems. Phys. Rev. A **77**, 033613 (2008)
34. D. Jaksch, C. Bruder, J.I. Cirac, C.W. Gardiner, P. Zoller, Cold Bosonic Atoms in Optical Lattices. Phys. Rev. Lett. **81**, 3108 (1998)
35. G. Vidal, Efficient Simulation of One-Dimensional Quantum Many-Body Systems. Phys. Rev. Lett. **93**, 040502 (2004)
36. M. Zwolak, G. Vidal, Mixed-State Dynamics in One-Dimensional Quantum Lattice Systems: A Time-Dependent Superoperator Renormalization Algorithm. Phys. Rev. Lett. **93**, 207205 (2004)
37. M. Hiller, Parametric Bose–Hubbard Hamiltonians: Quantum Dissipation, Irreversibility, and Pumping. Ph.D. thesis, Georg-August-Universität zu Göttingen, 2007

38. K. Sakmann, A.I. Streltsov, O.E. Alon, L.S. Cederbaum, Quantum dynamics of attractive versus repulsive bosonic josephson junctions: Bose–Hubbard and full-Hamiltonian results. Phys. Rev. A **82**, 013620 (2010)
39. K. Sakmann, A.I. Streltsov, O.E. Alon, L.S. Cederbaum, Optimal time-dependent lattice models for nonequilibrium dynamics. New J. Phys. **13**, 043003 (2011)
40. A.R. Kolovsky, H.J. Korsch, E.-M. Graefe, Bloch oscillations of Bose–Einstein condensates: Quantum counterpart of dynamical instability. Phys. Rev. A **80**, 023617 (2009)
41. J.A. Glick, L.D. Carr, Macroscopic Quantum Tunneling of Solitons in Bose–Einstein Condensates. ArXiv e-prints, May 2011. ArXiv:1105.5164 (2011)
42. A.C. Hindmarsh, A. Odepack, A Systematized Collection of ODE Solvers, in *Scientific Computing*, vol. 1 of IMACS Transactions on Scientific Computation, ed. by R. S. Stepleman (North-Holland, Amsterdam, 1983), pp. 55–64
43. G.A. Worth, M.H. Beck, A. Jäckle, H.D. Meyer, The MCTDH Package, Version 8.2, (2000). H.D. Meyer, Version 8.3 (2002), Version 8.4 (2007), see http://mctdh.uni-hd.de/
44. J. Stoer, R. Bulirsch, *Introduction to Numerical Analysis* (Springer New York, 1993)
45. A.I. Streltsov, O.E. Alon, L.S. Cederbaum, General mapping for bosonic and fermionic operators in Fock space. Phys. Rev. A **81**, 022124 (2010)
46. E. Anderson, Z. Bai, C. Bischof, S. Blackford, J. Demmel, J. Dongarra et al., *LAPACK Users' Guide*, 3rd edn. (Society for Industrial and Applied Mathematics, Philadelphia, PA, 1999). ISBN 0-89871-447-8
47. I. Březinová, A.U.J. Lode, A.I. Streltsov, O.E. Alon, L.S. Cederbaum, J. Burgdörfer, Wave chaos as signature for depletion of a Bose–Einstein condensate. Phys. Rev. A **86**, 013630 (2012)
48. K. Sakmann, Many-Body Schrödinger Dynamics of Bose–Einstein Condensates. Ph.D. thesis, University of Heidelberg (Springer Theses, Berlin Heidelberg, 2011)

Chapter 3
Benchmarks with Analytically Solvable Problems

> *Know thy self, know thy enemies. A thousand battles, a thousand victories.*
>
> Sun Tzu

In order to assess the validity and check the convergence of the MCTDHB method, it is appropriate to benchmark it against some analytically solvable interacting many-body problems. There are only few such problems, like, e.g., the Lieb-Liniger Hamiltonian. The latter is only solvable for the one-dimensional case, see Refs. [1–4]. To treat the dynamics of such systems is a tough problem by itself [5]. For this reason the so-called harmonic interaction model [6] is a better choice for a benchmark: *all* the eigenstates of the Hamiltonian are analytically known [7] for *any* dimensionality of the system, but still the Hamiltonian is a true many-body one which contains repulsive or attractive parabolic long-range two-body interactions. Interestingly, it was amply studied, see Refs. [8, 9], even including temperature, see Ref. [10]. However, there are so far neither studies of the time-evolution within the HIM nor considerations on the time-evolution of coherence, i.e., considerations how well the system is described by a single quantum mechanical one-particle state. As the MCTDHB allows to tackle the dynamics of the HIM, it is of fundamental interest to understand for instance how the system responds to an abrupt change of the interaction parameter, the so-called interaction quench. This chapter reiterates, in principle, the considerations presented in Ref. [11], adds considerations on the two-dimensional HIM and sheds light on the effect of separability in the dynamics of HIM Hamiltonians.

Electronic Supplementary Material Supplementary material is available in the online version of this chapter at http://dx.doi.org/10.1007/978-3-319-07085-8_3. Videos can also be accessed at http://www.springerimages.com/videos/978-3-319-07084-1.

A. U. J. Lode, *Tunneling Dynamics in Open Ultracold Bosonic Systems*,
Springer Theses, DOI: 10.1007/978-3-319-07085-8_3,

3.1 The Harmonic Interaction Model

The Hamiltonian of the HIM is readily obtained by setting the boson-boson interaction potential $\hat{W}$ and the one-body potential V in the many-body Hamiltonian in dimensionless units,

$$\hat{H} = \sum_{i=1}^{N} \left(\hat{T}(\vec{r}_i) + V(\vec{r}_i) \right) + \sum_{i<j}^{N} \hat{W}(\vec{r}_j, \vec{r}_i), \tag{3.1}$$

to be harmonic:

$$\hat{W}(\vec{r}_i, \vec{r}_j) = K \left(\vec{r}_i - \vec{r}_j \right)^2 ; \qquad V(\vec{r}) = \frac{1}{2}\omega^2 \vec{r}^2. \tag{3.2}$$

Here, K accounts for the strength of the two-body interaction and $\hat{T}(\vec{r}) = -\frac{1}{2}\partial_{\vec{r}}^2$ is the kinetic energy operator. A positive value of K corresponds to attraction while a negative value means repulsion. In the case of a parabolic trapping potential, it is easy to see that the system would become unbound when the value of K is negative and big enough for the two-body repulsion to overcome the one-body harmonic trapping, i.e., $K < -\frac{\omega^2}{2N}$. Following the line of Cohen and Lee in Ref. [6] the Hamiltonian, Eq. (3.1), can be separated into N independent harmonic oscillators by the following coordinate transformations:

$$\vec{x}_j = \frac{1}{\sqrt{j(j+1)}} \sum_{i=1}^{j} (\vec{r}_{j+1} - \vec{r}_i), \qquad j = 1, \ldots, N-1; \qquad \vec{x}_N = \sum_{i=1}^{N} \vec{r}_i. \tag{3.3}$$

The resulting Hamiltonian $\hat{H}$ is a sum of the relative and the center of mass Hamiltonians, $\hat{H} = \hat{H}_{rel} + \hat{H}_{CM}$. $\hat{H}_{rel}$ and $\hat{H}_{CM}$ read:

$$\begin{aligned} \hat{H}_{rel} &= \sum_{i=1}^{N-1} (-\frac{1}{2}\partial_{\vec{x}_i}^2 + \frac{1}{2}\delta_N^2 \vec{x}_i^2) \qquad \delta_N = \sqrt{\omega^2 + 2NK}. \\ \hat{H}_{CM} &= -\frac{1}{2}\partial_{\vec{x}_N}^2 + \frac{1}{2}\omega^2 \vec{x}_N^2 \end{aligned} \tag{3.4}$$

To this end, the Hamiltonian in the new coordinates describes $N - 1$ harmonic oscillators with the trapping frequency δ_N in a set of relative coordinates and 1 harmonic oscillator with the frequency ω in a center of mass coordinate.

The Hamiltonian in its separable form, Eq. (3.4), is easy to solve analytically. There is even an analytical solution when a product, i.e., Hartree-type ansatz ($\Psi = \frac{1}{\sqrt{N!}} \prod_{i=1}^{N} \phi(\vec{r}_i)$) is used, see e.g. Refs. [6, 7]. Because this is also the ansatz used to derive the famous Gross–Pitaevskii (GP) equation, it is instructive to refer to the

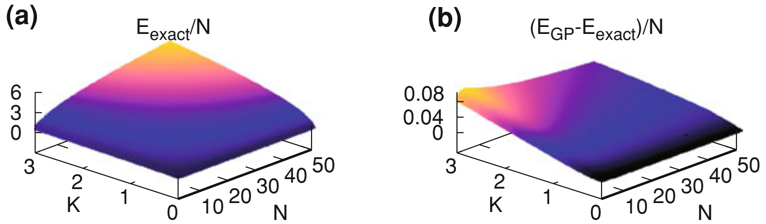

Fig. 3.1 Ground State Energies of the Harmonic Interaction Hamiltonian. The eigenvalues of the harmonic interaction Hamiltonian are depicted as a function of the interparticle interaction K and the particle number N for a trapping potential with $\omega = 1$. *Plot* (**a**) shows the exact energy per particle. *Plot* (**b**) shows the difference of the exact and the GP energies per particle. All quantities shown are dimensionless. See text for discussion

corresponding energies as GP energies and label them E_{GP}. One obtains the equations for the exact and the GP energies (when a product wave function is assumed), E_{exact} and E_{GP} of the Hamiltonian in Eq. (3.1), see e.g. Refs. [6, 7]:

$$E_{exact} = \frac{D}{2}\left((N-1)\delta(N,\omega,K)+\omega\right) \tag{3.5}$$

$$E_{GP} = \frac{ND}{2}\delta(N-1,\omega,K). \tag{3.6}$$

Here, D is the dimensionality of the system. A plot of the energy per particle, E_{exact}/N and the difference $(E_{exact} - E_{GP})/N$ is given in Fig. 3.1.

From the left panel of Fig. 3.1 one can see that the energy per particle is growing when the interaction or the particle number is increased. These features are reproduced by the GP approximation. The difference between the exact and the GP energies per particle increases as a function of interaction and decreases when the particle number is increased [see Fig. 3.1(b)]. It is therefore obvious that the best testing ground for a many-body method such as the MCTDHB is in the parameter region where the difference of the mean-field to the exact energies is the largest: for the benchmark of MCTDHB on the HIM, small N and large K are adequate.

3.2 Benchmark Studies with the Harmonic Interaction Model

Setup and Computational Details

The MCTDHB method relies on a multiconfigurational ansatz for the wave function, i.e., $|\Psi(t)\rangle = \sum_{\vec{n}} C_{\vec{n}}(t)|\vec{n}; t\rangle$. It is noteworthy that *both*, the coefficients $C_{\vec{n}}(t)$ and the permanents $|\vec{n}; t\rangle$ are time-dependent, variationally optimized quantities. The permanents are build up from M time-dependent orbitals. The numerical efficiency of MCTDHB comes from its time-dependent, adaptive orbitals. In total, the variational space is spanned by the N_{conf} coefficients and all N_{conf} possible products of M time-dependent functions. The equations of motion of the MCTDHB are obtained by tackling directly the many-boson TDSE with the above ansatz and the principle of least action [12]. The EOMs are efficiently solved numerically with the MCTDHB program package [13]. In order to obtain ground states, the EOMs are propagated in imaginary time and in order to compute dynamical evolutions, the EOMs are propagated in real time. The current study relies on the propagation of the orbitals' EOM with a shared-memory parallelized implementation of the Adams–Bashforth–Moulton predictor–corrector integrator and the coefficients' EOM with a hybridly OpenMP-MPI parallelized short iterative Lanczos algorithm. As a time-independent representation of the time-dependent orbitals, the numerically efficient and wide-spread fast Fourier transform collocation method was implemented also in a hybridly OpenMP-MPI parallel way – this corresponds to plane waves as (primitive) basis functions.

Of primary interest for the present considerations is the convergence when the number of orbitals is increased. Of course, the time-dependent variational principle guarantees that the solution will be exact for $M \to \infty$. For the studies of the convergence with the number of orbitals one first has to choose an appropriate number of plane wave functions for the used fast Fourier transform collocation. For this purpose, series of calculations, doubling the number of basis functions at each step, were performed until the difference in the obtained energy value was less than 10^{-12} and the last step was taken. Consequently, the primitive basis size in one dimension was $2^8 = 256$, and in two dimensions it was $2^{14} = 2^7 \times 2^7 = 16384$ plane wave functions per time-dependent orbital. The spatial extension of the grid in dimensionless units was chosen such that the ground state densities were less than 10^{-16} on the boundary. This resulted in box extensions of $[-8, 8]$ in one dimension, and $[-6, 6] \times [-6, 6]$ in two dimensions. The largest number of coefficients, N_{conf}, for the presented calculations was for the two-dimensional ground state of $N = 10$ bosons with $M = 18$ orbitals, namely, $N_{\text{conf}} = 8436285$.

In summary, the problem which the MCTDHB is applied to, is a very complex one: a one-, two- or three-dimensional correlated, long-range interacting, many-boson system described by many time-dependent configurations. In the time-dependent benchmarks which follow, even the one- and two-body potentials will be time-dependent. In order to evaluate such a (potentially time-dependent) non-contact two-body interaction numerically efficiently, the interaction matrix evaluation by successive transforms algorithm (IMEST) was used (for a description see Sect. 2.4.1.9 in Chap. 2, and Ref. [14]). It is in place to state here that it was necessary to generalize the IMEST for time-dependent potentials. This was done simply by evaluating the Fourier transform of the time-dependent interaction potential in every integration step. The original formulation in Ref. [14] was for time-independent two-body interactions and requires only a single Fourier transform of the interaction potential in the beginning of the computation. The computational overhead caused by the additional Fourier transform at each step was minimal. With setting up the computation, one is in the position to start the investigation on the ground states of the HIM with the MCTDHB.

Table 3.1 Selected Ground State Energies of the One-Dimensional Harmonic Interaction Hamiltonian: Exact Analytical versus Numerical MCTDHB (M) and TDGP Results

Dimensions	System	E_{exact}	Numerically exact	E_{GP}
1D	N=2, K=0.5	1.36602540	$E_{M=5} = 1.36602543$	$E_{M=1} = 1.41421356$
1D	N=2, K=2.0	2.00000000	$E_{M=8} = 2.00000002$	$E_{M=1} = 2.23606798$
1D	N=10, K=0.5	15.42481156	$E_{M=8} = 15.42481156$	$E_{M=1} = 15.81138870$
1D	N=10, K=2.0	29.31405907	$E_{M=10} = 29.31405908$	$E_{M=1} = 30.41381265$

3.2.1 One-Dimensional HIM

Ground State Benchmarks

To determine the properties of the convergence of the MCTDHB towards the exact results, it is instructive to choose a rather small particle number and a rather strong interaction, because the difference of the exact and the GP energies per particle is largest then, see Fig. 3.1. This means that one has more room to benefit from a many-body method systematically improving from the TDGP by increasing the orbital number M in the MCTDHB treatment in this situation. In order to benchmark MCTDHB with the HIM, the one-body potential $V(x)$, the values of K and the number of particles N have been chosen as $V(\vec{r}) = \frac{1}{2}\vec{r}^2$, $N = 2, N = 10$ and $K = 0.5, K = 2.0$. The exact ground state energies for these values (cf. Refs. [6, 7]) and the values obtained with MCTDHB with a different number of orbitals M for the one-dimensional case are collected in Table 3.1.

The convergence of the MCTDHB towards the exact solution of the HIM, is best seen by increasing the number of orbitals, M, used for the computation and plot the relative difference, $(E_{\text{MCTDHB}} - E_{\text{exact}})/E_{\text{exact}}$, to the corresponding exact energy. The one-dimensional results for these differences are given in Fig. 3.2.

The results prove that numerically exact solutions of the HIM can be obtained using the MCTDHB method with just a few time-adaptive self-consistent orbitals. Another instructive comparison, to check the behavior of the convergence of MCTDHB when changing the particle number, is to vary the particle number and interactions such that the mean-field energy per particle, E_{GP}/N, remains constant. This implies that $\Lambda = K/(N-1)$ is constant. Fig. 3.2(b) shows the relative energy difference for the particle numbers $N = 2, 5, 10, 50$ in the case of $\Lambda = 2.0$. The convergence is faster for larger particle numbers as it can be anticipated already from results in Fig. 3.1(b), cf. Fig. 3.2(b).

Before concluding the benchmark on the ground state of the HIM Hamiltonian it is timely to stress here, that in MCTDHB the many-body wave function is available for all time-points in a given computation in a very compact form which makes it amenable to compute from it one-body and two-body densities, first and second order correlation functions and other quantities of interest. When the energy is converged, also all these invariants describing the quantum many-body system

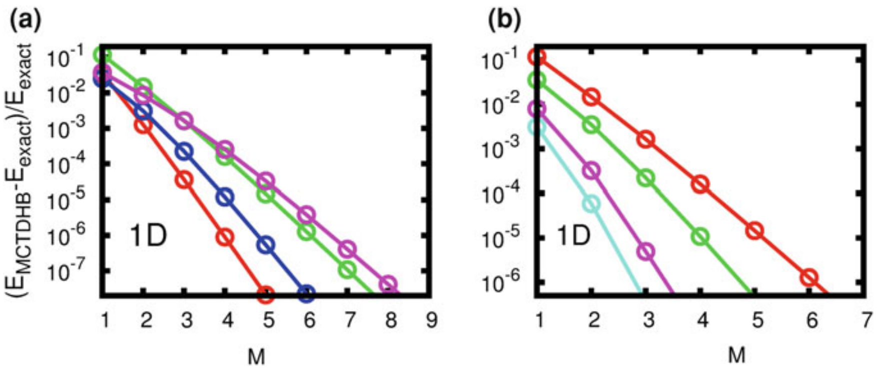

Fig. 3.2 Convergence of MCTDHB and Exact Energies in the Harmonic Interaction Model. The relative difference of the MCTDHB energy and the exact energy, $(E_{\text{MCTDHB}} - E_{\text{exact}})/E_{\text{exact}}$, is shown for the one-dimensional case for different orbital number M. In *panel* (**a**), the *red line* are for the $N = 2, K = 0.5$, the *blue line* for the $N = 10, K = 0.5$, the *green line* for the $N = 2, K = 2.0$ and the *magenta line* for the $N = 10, K = 2.0$ cases. The relative difference is decreasing exponentially with M. *Panel* (**b**) depicts the convergence with M for different particle numbers where $\Lambda = K/(N-1)$ is kept constant for $N = 2$ (*red line*), $N = 5$ (*green line*), $N = 10$ (*magenta line*) and $N = 50$ (*turquoise line*) particles. The pace of the convergence improves when increasing the particle number

converge. This will be shown for the nonequilibrium studies in Sect. 3.2.1. This concludes the benchmark study of the convergence of MCTDHB against the HIM ground state. The overall convergence with orbital number is exponential. In more than one dimension, the number of spherical harmonics is of importance. The convergence is improving, when the number of particles is increased while keeping a fixed $\Lambda = K(N-1)$.

Nonequilibrium Benchmarks in One Dimension

The next step is to compare the nonequilibrium dynamics of a given initial state within the HIM to the respective time-evolution within MCTDHB. As the scope of the present study is to benchmark and find the accuracy of the MCTDHB it is appropriate to select the most involved possible setup: time-dependent one-particle potentials $V(\vec{r}, t)$ and time-dependent two-body interactions $\hat{W}(\vec{r}, \vec{r}', t)$. For this, one has to shortly revisit the Hamiltonian of the HIM. It is given in its time-dependent form as follows:

$$\hat{H}(t) = \sum_{i=1}^{N}(-\frac{1}{2}\partial_{\vec{r}}^2 + \frac{1}{2}\omega(t)^2\vec{r}^2) + K(t)\sum_{i<j}^{j=N}\left(\vec{r}_i - \vec{r}_j\right)^2 = \hat{H}_{CM}(t) + \hat{H}_{rel}(t).$$

It is important to remember, that the $\hat{H}_{CM}$ describes a single particle and H_{rel} describes $N-1$ uncoupled particles, and the corresponding one-particle TDSEs are therefore easy to solve numerically, see Refs. [15, 16], even when the one-body potential is time-dependent. The used time-dependent trapping potential is defined by:

$$\omega \equiv \omega(t) = \omega_0 \left[1 + f(t)\right]. \tag{3.7}$$

In order to have a simple relation to the HIM Hamiltonian, one can choose δ_N such that $\hat{H}_{rel}$ remains time-independent. This can be achieved by making the interaction strength K time-dependent as follows:

$$K \equiv K(t) = K_0 \left[1 - \frac{\omega_0^2}{2NK_0} f(t)\right]. \tag{3.8}$$

With the two time-dependencies, Eqs. (3.7), (3.8), $\delta_N = \sqrt{\omega_0^2 + 2NK_0}$ is time-independent. Since the Hamiltonian is now time-dependent, the energy is no longer conserved. The expectation value of the Hamiltonian in Eq. (3.4) is (cf. e.g. Refs. [6, 7]):

$$\langle \Psi(t) | \hat{H}_{CM}(t) + \hat{H}_{rel} | \Psi(t) \rangle = \epsilon(t) + \frac{D}{2}(N-1)\delta_N. \tag{3.9}$$

$\epsilon(t)$ is obtained by integrating the one-body center of mass Schrödinger equation with the Hamiltonian $\hat{H}_{CM}(t) = -\frac{1}{2}\partial_{\vec{r}}^2 + \frac{1}{2}\omega_0^2(1+f(t))^2\vec{r}^2$. It is instructive to state here that the time-dependencies, Eqs. (3.7), (3.8), can be more general and it is of course not necessary to choose them such that the relative Hamiltonian H_{rel} is time-independent. Yet, there are two advantages to this particular choice: first, only a single additional one-particle Schrödinger equation has to be integrated and second, the convergence in the untransformed Hamiltonian which is solved within the MCTDHB, is more difficult to achieve. A very high fidelity of the method is needed in order to accurately reproduce the complex dynamics of only a small fraction of the system, i.e., one particle out of N. This is obvious from the coordinate transformations, see Eqs. (3.3), which decompose the original HIM Hamiltonian into subsystems made of $N-1$ identical effective particles in relative motion and to a quasi-particle representing the center of mass motion. In the chosen setup, one can picture the total system as a medium formed by $N-1$ identical, uncoupled particles. This medium is in a relative, oscillatory motion with a time-independent frequency δ_N, where the effective particle with coordinate x_N, representing the center of mass, is moving with a different time-dependent frequency ω. In what follows, two different time-dependent trapping and interaction potentials are chosen as

$$\begin{aligned} f_1(t) &= 0.2\sin^2(t) \\ f_2(t) &= \sin(t)\cos(2t)\sin(0.5t)\sin(0.4t). \end{aligned} \tag{3.10}$$

The one-body center of mass Schrödinger equation with the respective time-dependent potentials is solved to obtain the corresponding one-body energies $\epsilon_1(t)$, $\epsilon_2(t)$. See Figs. 3.3, and 3.4 for a plot of these quantities.

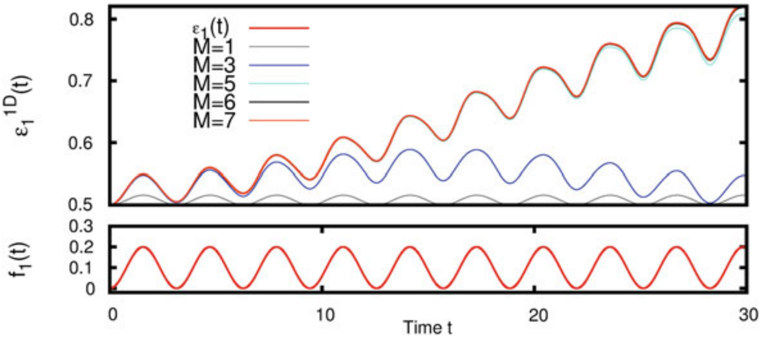

Fig. 3.3 Time-Dependent Energy $\epsilon_1(t)$ and Time-Dependence $f_1(t)$ to Modify the Harmonic Interaction Hamiltonian. The convergence of $\epsilon_1(t)$ when increasing the number of orbitals M is depicted for the one-dimensional case in the *upper panel*. For convenience, the time-dependency entering the Hamiltonian, $f_1(t)$, is plotted in the *lower panel*. The difference to the exact result is decreasing to 0 when increasing M. See text for discussion

The agreement of the time-dependent parts of the energies corresponding to $\epsilon_1(t)$ in one dimension is striking, see Fig. 3.3, even for the wildly oscillatory $\epsilon_2(t)$, see Fig. 3.4. It is obvious from the convergence studies with $\epsilon_1(t)$ that the MCTDHB converges very well when one increases the number of variational parameters, i.e., orbitals and coefficients, even for the present cases with time-dependent one-body *and* two-body potentials. The reason for the slight differences at bigger times in the $\epsilon_2(t)$ case is that the strong time-dependence of the potential *and* the interaction force the system to fragment quickly and the number of orbitals is insufficient to achieve convergence for times larger than $t \sim 25$ in the $N = 10, M = 6$ and $N = 50, M = 5$ cases with $K = 0.5$. When increasing M to $N = 10, M = 7$ and $N = 50, M = 6$, convergence improves, see Fig. 3.4 and its inset. The oscillatory motion of the center of mass results in a relatively small contribution to the total energy: the values of $\epsilon_1(t), \epsilon_2(t)$ are roughly one to two orders of magnitude smaller than the energies in Table 3.1. It is noteworthy, that this implies that a high fidelity is needed to describe accurately the motion of a small fraction of the system (as discussed above). This makes the number of orbitals for the convergence higher compared to the other calculations. In general, a calculation can be considered as *numerically exact* when the least occupied orbital has a population of less than 10^{-3}. In the high fidelity cases with small energy oscillations and long-range interactions presented here 10^{-6} or less is needed. An appropriate measure for the fidelity of the MCTDHB method is the absolute relative error $\Delta E_1^{1D}(t)$ of the time-dependent total energies, $E_{\mathrm{MCTDHB}}^{1D/2D}(t)$ for the one-dimensional calculations with the time-dependency $f_1(t)$, respectively,

$$\Delta E_1^{1D}(t) = \sqrt{\left(\frac{E_{\mathrm{MCTDHB},1}^{1D}(t) - E_{\mathrm{exact},1}^{1D}(t)}{E_{\mathrm{exact},1}^{1D}(t)}\right)^2}. \tag{3.11}$$

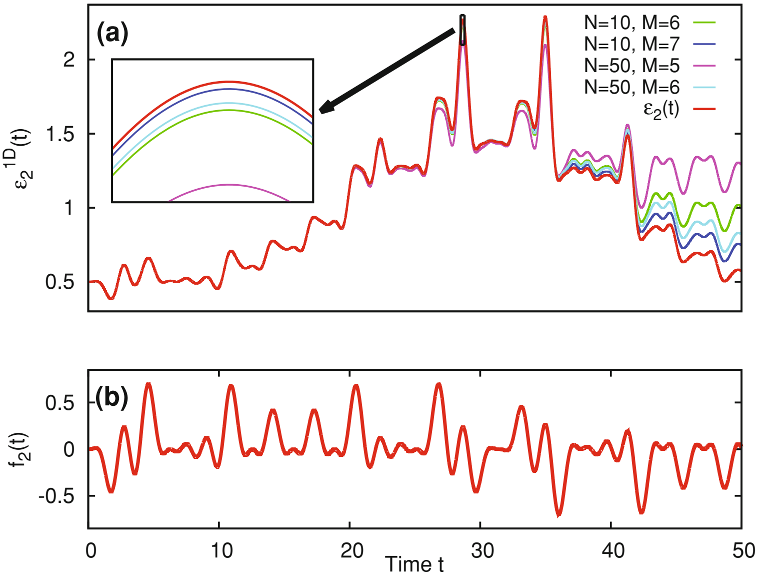

Fig. 3.4 Time-Dependent Energy $\epsilon_2(t)$ and Time-Dependence $f_2(t)$ to Modify the Harmonic Interaction Model.* In *panel* (**a**) the time-dependent contribution in the energy of the MCTDHB calculation for $N = 10$, $M = 6/7$ and $N = 50$, $M = 5/6$ is shown for the case of $f_2(t)$. The *red line* is the exact solution. Small discrepancies start to occur when the number of orbitals becomes insufficient to account for the large amount of energy pumped into the system. In *panel* (**b**) the time-dependency $f_2(t)$ chosen for the HIM Hamiltonian is plotted for convenience. See Video 1 for the time-evolution of the density and the coherence computed with MCTDHB. See text for discussion

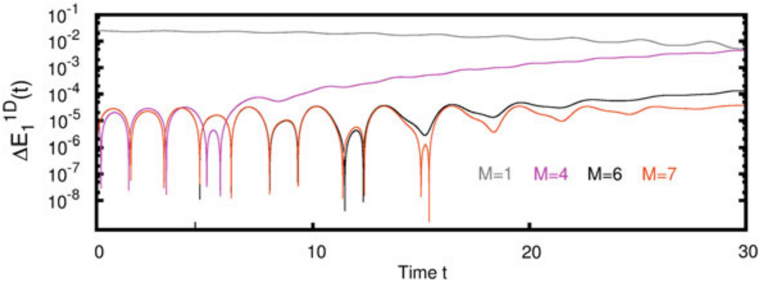

Fig. 3.5 Absolute Relative Error of the Time-Dependent Total Energies Computed with MCTDHB. This *plot* depicts the relative total error in the time-dependent energies, $\Delta E_1^{1D}(t)$, for $N = 10$, $K = 0.5$ with the time-dependency $f_1(t)$ in one dimension. See text for further discussion

Here, $E^{1D}_{\text{MCTDHB},1}(t)$ is the computed MCTDHB energy at time t and $E^{1D}_{\text{exact},1}(t)$ is the exact energy, obtained from solving the relative one-body problem with the Hamiltonian $\hat{H}_{rel}$ and the time-dependent center of mass one-body problem with the Hamiltonian $\hat{H}_{CM}$ with the time-dependency $f_1(t)$. For a plot of $\Delta E_1^{1D}(t)$ see Fig. 3.5.

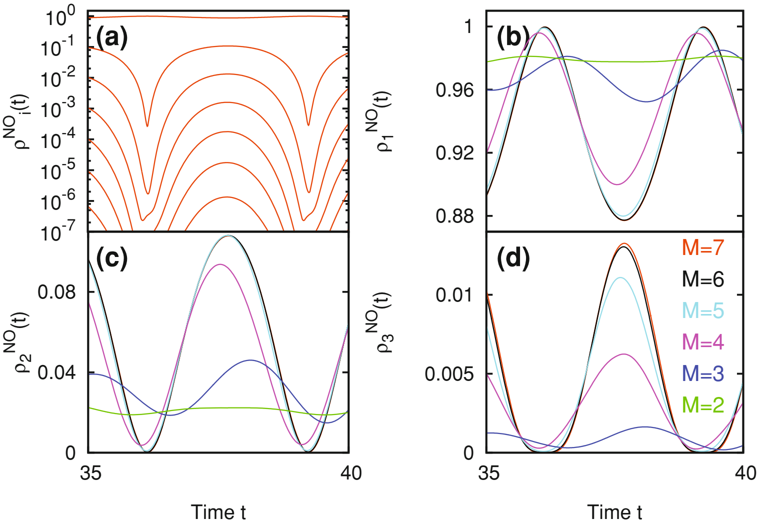

Fig. 3.6 Convergence of the Occupation Numbers for the Time-Dependent Potentials in One Dimension. *Panel* (**a**) shows all occupations of the converged $N = 10, K = 0.5$ time-dependent study with $M = 7$. *Panel* (**b**–**d**) show how the time-evolution of the first three occupation numbers $\rho_1^{NO}(t)$, $\rho_2^{NO}(t)$ and $\rho_3^{NO}(t)$ converges for increasing orbital number M. The *color code* indicated by the labels in *panel* (**d**) holds also for *panels* (**b**) and (**c**). See text for discussion

From this figure it can be clearly seen that the MCTDHB method reveals this high fidelity and grasps the highly oscillatory motion of the center of mass quasi-particle through the harmonic oscillators of the relative motion with great accuracy. Given the small depletion, one could assume that the TDGP would provide a reasonable description of the system in some cases. Yet, the TDGP result plotted in Fig. 3.3 shows that only the higher frequency of the dynamics is covered but the lower one is not captured at all. So, even in the situation where one assumes the validity of the TDGP mean-field, the proper description of the many-boson system can be obtained only within the framework of exact many-body methods. To display a general way to find out if a given calculation with MCTDHB is converged it is appropriate to check on the convergence of the natural occupation numbers $\rho_i{}^{(NO)}(t), i = 1, \ldots, M$, see Eq. (2.26) for their definition. A plot of those for the respective time-dependent potential is given in Fig. 3.6 that for the present one-dimensional study.

One can deduce from Figs. 3.3, 3.4, 3.6 that the convergence of the natural occupations $\rho_i^{(NO)}$ implies the convergence of the energies. Generally, the occupations of the least occupied orbitals are very small. As their sum is normalized, it is obvious that the higher occupations do not change anymore when the lowest ones become negligibly small. Depending on the desired accuracy of a given calculation it is therefore appropriate to use the size of the smallest occupation as a measure for the convergence. In the present example, the energies were *numerically exact* when the smallest occupation was below 10^{-6}. It has to be stressed, that this holds for the

Table 3.2 Selected Ground State Energies of the Two-Dimensional Harmonic Interaction Hamiltonian: Exact Analytical versus Numerical MCTDHB(M) and TDGP Results

2D	N=2, K=0.5	2.73205081	$E_{M=10} = 2.73205682$	$E_{M=1} = 2.82842712$
2D	N=2, K=2.0	4.00000000	$E_{M=18} = 4.00008958$	$E_{M=1} = 4.47213595$
2D	N=10, K=0.5	30.84962311	$E_{M=18} = 30.84964834$	$E_{M=1} = 31.62277660$
2D	N=10, K=2.0	58.62811814	$E_{M=18} = 58.63132065$	$E_{M=1} = 60.82762530$

present examples with time-dependent *one-body* and *long-range two-body* potentials only; in the much more usual case of dynamics without those time-dependencies, and for short-range interaction potentials, convergence is achievable easier, i.e., already when the smallest occupation is below 10^{-3}.

3.2.2 Two-Dimensional HIM

To complement the previous subsection on the one-dimensional HIM model (Sect. 3.2.1) and show the applicability of the MCTDHB method to the many-particle problem also in higher dimensionalities $D \geq 2$, the present subsection illustrates the results obtained in the application of MCTDHB to the two-dimensional HIM. This is achieved by following the same strategy as in the one-dimensional case. First the MCTDHB accuracy for two-dimensional ground states and thereafter for the time-dependent variation of the HIM Hamiltonian (cf. Eqs. (3.4), (3.10)) is quantified.

Ground State Benchmarks

Table 3.2 collects several representative values for the energies of the two-dimensional HIM Hamiltonian and compares the MCTDHB energies to the exact and the TDGP ones. As it can be deduced from the comparison of numerical to the exact values in Table 3.2, the convergence towards the exact eigenenergies of the HIM Hamiltonian of MCTDHB is outstanding also in the present two-dimensional case. To continue the analysis of the convergence properties of MCTDHB, it is instructive to plot the eigenenergies of the two-dimensional HIM Hamiltonian obtained for different orbital numbers M. See Fig. 3.7 for a plot. One can see from Fig. 3.7 that in the two-dimensional case, the respective number of spherical harmonics shows up as a staircase in the plots. This is of course due to the spherical symmetry of the problem, i.e., because an isotropic parabolic trap $V(\vec{r})$ was chosen as the one-body potential. The benefit in accuracy is larger, when a new shell in the set of two-dimensional spherical harmonics is opened by a respective new orbital. It now remains to check if the good convergence properties of the MCTDHB method prevail in the case of the time-dependent one-body and two-body potentials in two dimensions studied in Sect. 3.2.1 for the one-dimensional case.

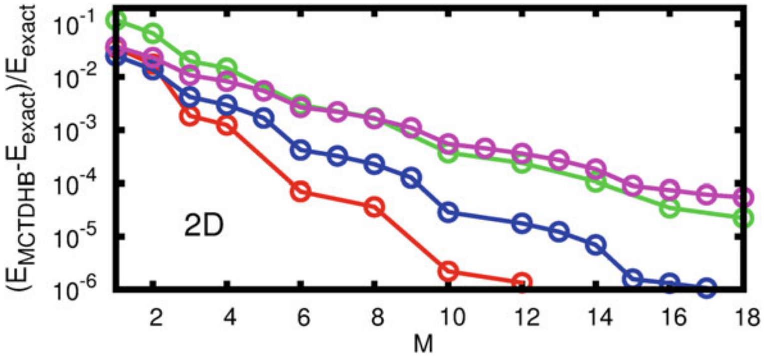

Fig. 3.7 Convergence of MCTDHB and Exact Energies in the Harmonic Interaction Model. The relative difference of the MCTDHB energy and the exact energy, $(E_{\text{MCTDHB}} - E_{\text{exact}})/E_{\text{exact}}$, is shown for the two-dimensional case for different orbital number M. The *red line* are for the $N = 2$, $K = 0.5$, the *blue line* for the $N = 10$, $K = 0.5$, the *green line* for the $N = 2$, $K = 2.0$ and the *magenta line* for the $N = 10$, $K = 2.0$ case. The relative difference is decreasing exponentially with M. For the two-dimensional systems, the number of spherical harmonics is of importance. See text for further discussion

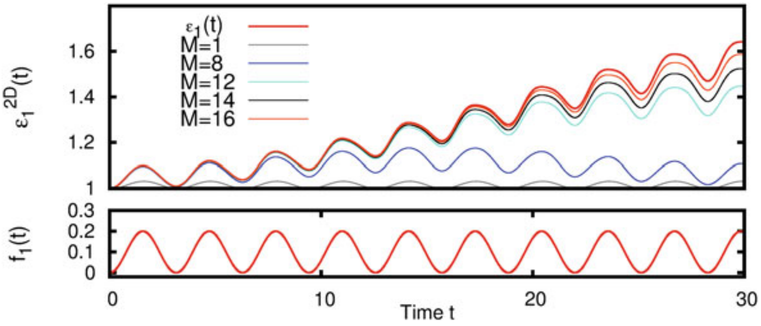

Fig. 3.8 Time-Dependent Energy $\epsilon_1(t)$ and Time-Dependence $f_1(t)$ to Modify the Two-Dimensional Harmonic Interaction Hamiltonian. The convergence of $\epsilon_1(t)$ when increasing the number of orbitals M is depicted for the two-dimensional case in the *upper panel*. For convenience, the time-dependency entering the Hamiltonian, $f_1(t)$, is plotted in the *lower panel*. The difference to the exact result is decreasing to 0 when increasing M. See text for discussion

Nonequilibrium Benchmarks in Two Dimensions

For the study of the time-dependent Hamiltonian of the HIM in two dimensions, one can straightforwardly apply the transforms in Eqs. (3.7), (3.8). Because of brevity, this section is restricted to the simple time-dependency $f_1(t)$ in Eq. (3.10). For a plot of the time-dependent energy $\epsilon_1^{(2D)}$ and the time-dependence $f_1(t)$, see Fig. 3.8. It is seen from this Figure, that an exact solution of the two dimensional time-dependent HIM model is more difficult to achieve. Heuristically, this comes from the fact that the excitation energy compared to the total energy of the system is much smaller in the

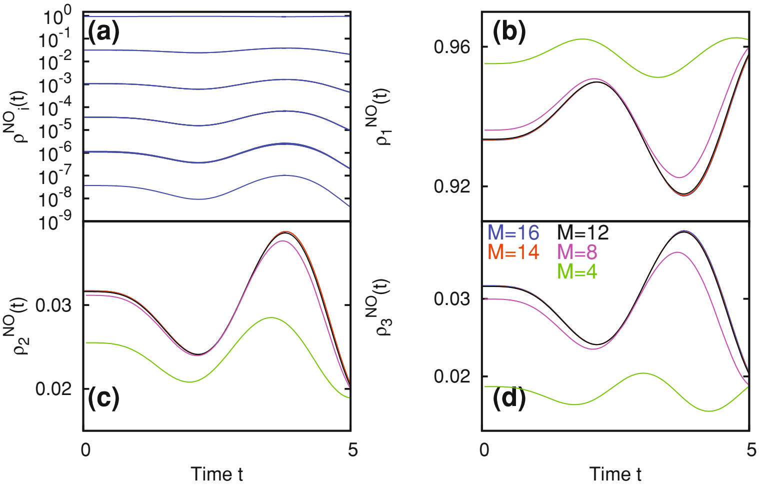

Fig. 3.9 Convergence of the Occupation Numbers for the Time-Dependent Potentials in Two Dimensions. *Panel* (**a**) shows all occupations of the converged $N = 10, K = 0.5$ time-dependent study with $M = 16$. *Panel* (**b**–**d**) show how the time-evolution of the first three occupation numbers $\rho_1^{NO}(t)$, $\rho_2^{NO}(t)$ and $\rho_3^{NO}(t)$ converges for increasing orbital number M. The *color code* indicated by the labels in *panel* (**d**) holds also for *panels* (**b**) and (**c**). See text for discussion

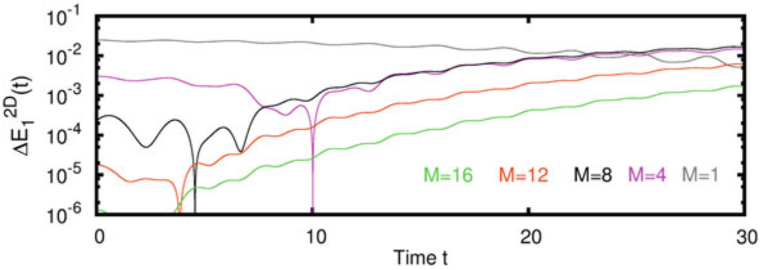

Fig. 3.10 Absolute Relative Error of the Time-Dependent Total Energies in Two Dimensions Computed with MCTDHB. The *plot* depicts $\Delta E_1^{2D}(t)$ for $N = 10, K = 0.5$ in two dimensions. To achieve the same relative total error in the time-dependent energies more orbitals are needed in the respective two-dimensional systems. See text for further discussion

two-dimensional case as in the one-dimensional one discussed in Sect. 3.2.1. Because of this, the number of orbitals needed to treat the time-dependent two-dimensional HIM Hamiltonians numerically, is larger, see Fig. 3.8. To quantify this observation, it is interesting to graph the time-evolution of the natural occupations $\rho_i^{(NO)}(t)$ as well as the relative error of the time-dependent energy $\epsilon_1^{(2D)}(t)$, $\Delta E^{(2D)}_{MCTDHB}(t)$ which is defined analogous to Eq. (3.11). For a plot, see Figs. 3.9 and 3.10, respectively.

It is seen nicely from Fig. 3.9 that the occupation numbers are converging to the exact solution when the number of orbitals is increased and the occupations of the lowest ones become negligibly small. This resembles the behavior in the one-dimensional case (cf. Sect. 3.2.1) and is as expected for a treatment of the TDSE using the TDVP. The next Fig. 3.10 shows the time-dependent relative error and thereby further quantifies this observation.

It is seen from Fig. 3.10 that the time-dependent relative error $E_1^{2D}(t)$ tends to 0 when the orbital number M is increased also in the present case. Numerically exact solutions of the problem can hence be achieved by increasing M also in the two-dimensional cases with time-dependent one- and two-body interactions. Taking a closer look at the scale in Figs. 3.10 and 3.5 which shows the E_1^{1D}, i.e., the time-dependent relative error in the one-dimensional case, one notes that the error in the two-dimensional case is roughly twice as large as in the one-dimensional ones, i.e., $E_1^{2D} \approx 2 \cdot E_1^{1D}$ when twice the number of orbitals are used for in the respective two-dimensional computation. This can be explained by arguing with the separability of the isotropic problem studied here, see Sect. 3.4.

3.3 Dynamics of an Interaction Quench in the Harmonic Interaction Model

The HIM features a lot of the physics of the Hamiltonian with contact interactions. One of these, which can be nicely shown by applying the MCTDHB, is the dynamical change of the occupation numbers, when quenching the interaction. To investigate it, one sets up a solution of the HIM Hamiltonian, Eqs. (3.1), (3.2), with a certain interaction K^i as the initial guess. Subsequently, the interaction is abruptly switched to another value K^f. This *interaction quench* causes the dynamics, which are the topic of this section. As an illustrative example $N = 10$ one- and two-dimensional bosons with initial interactions $K_1^i = 0.5$, $K_2^i = 2.0$ were chosen as initial guesses. The interactions were quenched to the values $K_1^f = 2.0(\equiv K_2^i)$ and $K_2^f = 0.5(\equiv K_1^i)$, respectively. See Fig. 3.11 for a plot of the time-evolution of the fragmentation, i.e., the first occupation number $\rho_1^{(NO)}(t)$ for the respective one- and two-dimensional cases. The behavior of the fragmentation in Fig. 3.11 is oscillatory with a bigger frequency for the $K_1^i \to K_1^f$ quench (Q1) than for the $K_2^i \to K_2^f$ quench (Q2). The frequency is the same for the one-dimensional and two-dimensional cases. Intuitively, the fragmentation decreases, first, when one decreases the interaction, and the wave function becomes more condensed in Q2 initially. Correspondingly, in Q1, by increasing the interaction, the wave function becomes more fragmented initially. In both cases the fragmentation is roughly twice larger in the two-dimensional compared to the one-dimensional cases. This can be explained by the energetics of the system. Simply, because the dimensionality is a global factor in the total energy and consequently the change in energy by the interaction quench is twice larger in the two-dimensional cases compared to the one-dimensional cases for Q1 and Q2, respectively. The degree of fragmentation hence is roughly proportional to the change in the total energy, i.e., proportional to the energy pumped into the system by the interaction quench. Because the interaction and the trapping potential are isotropic, the quench

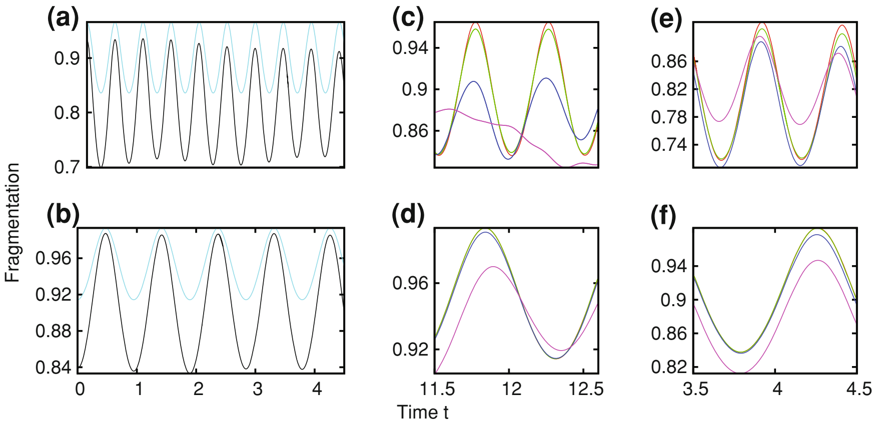

Fig. 3.11 Interaction Quench Dynamics for $N = 10$ Particles. *Panels* (**a**), (**c**) and (**e**) depict the time evolution of the fragmentation for the interaction quench from $K_1^i = 0.5 \rightarrow K_1^f = 2.0$ and *panels* (**b**), (**d**) and (**f**) depict the time-evolution of the fragmentation for the interaction quench from $K_2^i = 2.0 \rightarrow K_2^f = 0.5$. In (**a**) and (**b**) the fragmentation for both the one-dimensional (*turquoise lines*) and the two-dimensional (*gray lines*) are oscillatory. The fragmentation is roughly twice as large in the two-dimensional case than in the one-dimensional one—this can be explained from the separability of the problem when using center-of-mass and relative coordinates, cf. Sect. 3.4. For convenience, the convergence of the fragmentation for the one- [*panels* (**c**), (**d**)] and two-dimensional [*panels* (**e**), (**f**)] cases is depicted also. The *color code* is (**c**): $M = 3/5/7/8$, *magenta/blue/green/red line*, respectively, (**d**): as in (**c**), (**e**): $M = 10/14/15/16$, *magenta/blue/green/red line*, respectively, (**f**): $M = 6/10/15/16$, *magenta/blue/green/red line*, respectively. The *red curves* in *panels* (**c**–**f**) are the converged results and are identical with the respective *gray/turquoise lines* in *panels* (**a**), (**b**). See text for further discussion

dynamics are dynamics in the relative coordinates. That the fragmentation is roughly twice as large as in the two-dimensional case means that roughly twice as many particles are excited to move relatively to each other. One can estimate the frequencies of the oscillations from the difference $\Delta E_{Q1/2} = E^f_{Q1/2} - E_{K^f_{1/2}}$ of the energy after the quench $E^f_{Q1/2}$ to the respective ground state energy at the interaction $K^f_{1/2}$, $E_{K^f_{1/2}}$. The oscillatory frequencies $\nu_{Q1/2}$ are obtained by $\nu_{Q1/2} = \frac{\Delta E_{Q1/2}}{2\pi}$ (remind that $\hbar = 1$ in the units used). In the one-dimensional case one finds $\nu_{Q1} = \frac{3.3475}{2\pi} = 0.5328$ and $\nu_{Q2} = \frac{6.4628}{2\pi} = 1.0286$. The agreement with the frequencies in Fig. 3.11(a) and (b) is satisfactory.

Transferring the finding for the HIM to the corresponding systems with shorter-ranged, contact-like interaction, one would expect the coherence of systems of higher dimensionality to be more sensitive to changes of external parameters, such as the interaction strength or the trap geometry, because the change in the total energy is larger for bigger dimensionality. This is true also for parabolically confined three- and two-dimensional ultracold bosons and their one-dimensional counterparts with short-range interactions.

3.4 Comment on the Effects of the Separability of the Harmonic Interaction Model

The solutions of the TDSE with the two-dimensional HIM Hamiltonian, Eqs. (3.1), (3.2), is separable because one can write this Hamiltonian in the form

$$\hat{H}(\vec{X}, \vec{Y}) = \hat{H}^X(\vec{X}) + \hat{H}^Y(\vec{Y}). \tag{3.12}$$

Here, $\vec{X}$ and $\vec{Y}$ are collective coordinates of all N particles in the x and y directions, i.e., $\vec{X} = (x_1, \ldots, x_N)$ and $\vec{Y} = (y_1, \ldots, y_N)$, respectively. If one considers a quench scenario, as done above in Sect. 3.3, where the initial state is an eigenstate of an Hamiltonian as in Eq. (3.12), then this initial state is separable, i.e.,

$$\Psi(\vec{X}, \vec{Y}; t = 0) = \Psi^X(\vec{X}, t = 0)\Psi^Y(\vec{Y}, t = 0).$$

Furthermore, the time evolution of such an initial state with any Hamiltonian of the form in Eq. (3.12), will preserve this separability. Therefore, one obtains that the above equation holds for any time $t \geq 0$, i.e.,

$$\Psi(\vec{X}, \vec{Y}; t) = \Psi^x(\vec{X}, t)\Psi^y(\vec{Y}, t) \tag{3.13}$$

holds for the interaction quench studied in the previous Sect. 3.3. It follows, that the RDM $\rho(\vec{X}, \vec{Y}|\vec{X}', \vec{Y}'; t)$ also is separable in the same way:

$$\rho(\vec{r}|\vec{r}'; t) = \rho^x(x|x'; t)\rho^y(y|y'; t). \tag{3.14}$$

Note, that the reduced one-body density ρ and its factors ρ^x and ρ^y depend not on collective coordinates $\vec{X}', \vec{X}, \vec{Y}', \vec{Y}$ but on single ones $\vec{r}, \vec{r}', x, x'$, and y, y', respectively. For these RDMs ρ^x, ρ^y, and ρ in Eq. (3.14) one can of course find a diagonal representation (for reference, see the paragraph on natural occupations and natural orbitals in Sect. 2.1.2). One obtains

$$\begin{aligned}
\rho(\vec{r}|\vec{r}'; t) = &\left[\sum_j \rho_j^{(NO,x)}(t)\phi_j^{(NO)}(x, t)\phi_j^{*(NO)}(x', t)\right] \\
&\times \left[\sum_k \rho_k^{(NO,y)}(t)\phi_k^{(NO)}(y, t)\phi_k^{*(NO)}(y', t)\right] \qquad (3.15)\\
= &\sum_{j,k}\left(\left[\rho_j^{(NO,x)}(t)\rho_j^{(NO,y)}(t)\right]\right. \qquad (3.16)\\
&\left.\times \left[\phi_j^{(NO)}(x, t)\phi_k^{(NO)}(y, t)\right] \times \left[\phi_j^{*(NO)}(x', t)\phi_k^{*(NO)}(y', t)\right]\right).
\end{aligned}$$

In the above equations, there is only a single set of natural orbitals $\phi_j^{(NO)}$, as the problem is assumed to be isotropic. A few comments on (i) the fragmentation and (ii) an estimate of the relation of the errors in one-dimensional computations to the error in two-dimensional ones are in place here. For (i) the fragmentation it is interesting to note, that if one of the factors in the density matrix above, say ρ^x, has a small fragmentation, i.e., let

$$\rho_1^{(NO,x)}(t) = 1 - \left[\sum_{j>1} \rho_j^{(NO,x)}(t) \right] \approx 1 - \epsilon. \tag{3.17}$$

It straightforwardly follows that in the two dimensional computation for the isotropic case of an interaction quench the fragmentation must be roughly twice as big when ϵ is not too large, i.e.,

$$\rho_1^{(NO,x)}(t)\rho_j^{(NO,y)}(t) \approx (1-\epsilon)^2 = 1 - 2\epsilon + \epsilon^2 \approx 1 - 2\epsilon. \tag{3.18}$$

The first approximation here is that one assumes the *fragmentations in x and y direction* to be roughly the same. Especially, in the case of an isotropic potential and for a quench scenario as the one studied above, where the initial state is also an eigenfunction of an Hamiltonian with an isotropic potential this is true up to numerical accuracy. The second approximation consists in assuming the smallness of the fragmentation in both, x and y directions, i.e., the negligibility of $\mathcal{O}(\epsilon^2)$, which is appropriate in the case of weak to moderate interparticle interaction K. This explains (i) the observation of double the fragmentation for two-dimensional cases made in the above Sect. 3.3. For the observation (ii) that the error in the two-dimensional case is roughly twice larger for computations with twice the number of orbitals than in a respective one-dimensional computation. This can be seen easily from the above estimate, when one associates ϵ not with the fragmentation, but with the error that remains when approximating each of the density matrices ρ^x and ρ^y with a given number of orbitals $M_x = M_y$, respectively. It remains to stress that in view of the conjectures lined out above it would be very interesting to study the dynamics of a nonisotropic system or nonisotropic quench, since then the separability for the analytics which was exploited throughout the present subsection is not given.

3.5 Discussion and Summary of the Benchmark with the Harmonic Interaction Model

Throughout this work, the youngest method in the family of the MCTDH methods, namely MCTDHB, has been benchmarked with the HIM for the convergence of ground states and dynamics in one and two spatial dimensions. Furthermore, an application of MCTDHB to the fragmentation dynamics occurring within the HIM in the case of an interaction quench was provided.

In conclusion, it was proven that the MCTDHB, like the other members of the MCTDH family of methods, can be used to obtain *numerically exact* solutions of the many-body TDSE for one-, and two-dimensional systems. The considered many-boson systems can be described in a numerically exact way when the interaction is arbitrary (weak to strong, attractive or repulsive) and the particle number is small enough to allow one to use enough orbitals to achieve convergence, even in the present case of parabolic long-range interactions. In the case of large orbital and small particle number, the numerically most demanding part is to propagate the coupled integro-differential EOMs for the orbitals, as given in Ref. [12] and Eqs. (2.46 and 2.47). Numerically exact solutions are also possible if the particle number is large enough to make convergence achievable with a small number of orbitals, as shown in Fig. 3.2(b). In this case, the numerically most demanding part is the propagation of the equations for the coefficients as given in Ref. [12] and Eq. (2.46).

The convergence is improving roughly exponentially with the number of orbitals. Less orbitals are needed for constant $\Lambda = K(N-1)$ and a large particle number. Higher dimensionality and the long-range interactions of the HIM require more orbitals for convergence than the respective problems with short-range interactions. The respective number of spherical harmonics becomes of importance for more than one-dimensional studies in spherically symmetric setups.

Numerically exact solutions are obtainable even for smoothly varying, time-dependent one- *and* long-range two-body potentials. For stronger oscillatory behavior convergence is harder to achieve, and the necessary number of orbitals is larger in this case. The dynamics of the time-dependent Hamiltonians with time-dependent one-body and time-dependent two-body potentials are of course more difficult to describe.

As an application the fragmentation dynamics of an interaction quench scenario was studied. The behavior found is oscillatory and tends towards less fragmentation first in the case of lowering the interaction and towards stronger fragmentation first in the case of increasing the interaction. The oscillation frequencies are determined by the difference of the energy after the quench to the respective ground state energies at the final interaction strength. In the comparison of the one-dimensional and two-dimensional quenches the fragmentation is about twice larger than in the latter case. This is a manifestation of the relation of the change in the total energy in one dimension and two dimensions [cf. Eq. (3.5)]. The interaction quench imposes a change in energy two times larger in two dimensions compared to that in one dimension.

The relation of the change in energy for different dimensionalities of the problem is in turn caused by the separability of the problem in the isotropic case studied. In fact, it was shown that the wave function as well as the 1-RDM of the problem factor in the two-dimensional case and the above observation for the fragmentation in the isotropic quench scenario could be deduced. It would hence be very interesting to e.g. study a nonisotropic quench scenario, but this is beyond the scope of the present considerations.

References

1. E.H. Lieb, W. Liniger, Exact Analysis of an Interacting Bose Gas. I. The General Solution and the Ground State. Phys. Rev. **130**, 1605 (1963)
2. E.H. Lieb, Exact Analysis of an Interacting Bose Gas. II. The Excitation Spectrum. Phys. Rev. **130**, 1616 (1963)
3. J.G. Muga, R.F. Snider, Solvable three-boson model with attractive δ-function interactions. Phys. Rev. A **57**, 3317 (1998)
4. K. Sakmann, A.I. Streltsov, O.E. Alon, L.S. Cederbaum, Exact groundstate of finite Bose–Einstein condensates on a ring. Phys. Rev. A **72**, 033613 (2005)
5. D. Jukić, B. Klajn, H. Buljan, Momentum distribution of a freely expanding Lieb-Liniger gas. Phys. Rev. A **79**, 033612 (2009)
6. L. Cohen, C. Lee, Exact reduced density matrices for a model problem. J. Math. Phys. **26**, 3105 (1985)
7. Y.A.N. Jun, Harmonic Interaction Model and Its Applications in Bose–Einstein Condensation. J. Stat. Phys. **113**, 623 (2003)
8. S. Pruski, J. Maćkowiak, O. Missuno, Reduced density matrices of a system of N coupled oscillators. 2. Eigenstructure of the 1-particle matrix for the canonical ensemble. Rep. Math. Phys. **3**, 227 (1972)
9. S. Pruski, J. Maćkowiak, O. Missuno, Reduced density matrices of a system of N coupled oscillators. 3. The eigenstructure of the p-particle matrix for the ground-state. Rep. Math. Phys. **3**, 241 (1972)
10. J. Maćkowiak, O. Missuno, S. Pruski, Reduced density matrices of a system of N coupled oscillators. 4. The eigenstructure of the p-particle matrices for the two-temperature canonical ensemble. Rep. Math. Phys. **5**, 327 (1974)
11. A.U.J. Lode, K. Sakmann, O.E. Alon, L.S. Cederbaum, A.I. Streltsov, Numerically exact quantum dynamics of bosons with time-dependent interactions of harmonic type. Phys. Rev. A **86**, 063606 (2012)
12. O.E. Alon, A.I. Streltsov, L.S. Cederbaum, Multiconfigurational time-dependent Hartree method for bosons: Many-Body dynamics of bosonic systems. Phys. Rev. A **77**, 033613 (2008)
13. A.I. Streltsov, K. Sakmann, A.U.J. Lode, O.E. Alon, L.S. Cederbaum, *The multiconfigurational time-dependent Hartree for Bosons package, version 2.3* (Heidelberg, 2012), see http://mctdhb.uni-hd.de
14. K. Sakmann, *Many-body Schrödinger dynamics of Bose–Einstein condensates*. Ph.D. thesis, University of Heidelberg (Springer Theses, Berlin Heidelberg, 2011)
15. W.H. Press, S.A. Teukolsky, W.T. Vetterling, B.P. Flannery, *Numerical Recipes in Fortran* (Cambridge University Press, Cambridge, 1992)
16. R. Kosloff, Time-Dependent Quantum-Mechanical Methods for Molecular Dynamics. J. Phys. Chem. **92**, 2087 (1988)

Chapter 4
A Case Study with an Attractive BEC: Comparison of Lattice Model, Gross–Pitaevskii, and MCTDHB Predictions on a Tunneling Process

> *It is a mistake to think you can solve any major problems just with potatoes.*
>
> Douglas Adams, Life, the Universe and Everything

After the previous assessment of the numerical exactness of MCTDHB (M) in the case of convergence with the number of orbitals, see Chap. 3, it remains to compare MCTDHB to other methods in the field. For this comparison the continuous methods MCTDHB and TDGP [i.e., MCTDHB $(M = 1)$] and the lattice methods DNLS and TEBD/BH are used. It is of great interest to compare the predictions these amply applied discrete and continuous space theories and their numerical implementations. With this comparison, light is shed on the effects and the importance of the way that a given many-boson problem is discretized and numerically handled. In the lattice models DNLS and TEBD/BH, the spatial representation of the wave function is discretized using Wannier functions whereas the spatial representation of the wave function for TDGP and MCTDHB is continuous and uses functions determined according to the time-dependent variational principle. In that, these methods approximate the solutions of the full many-body problem in a self-consistent manner. The importance of this self-consistency will become evident throughout the present chapter. In Ref. [1] the two lattice methods' predictions on the decay by tunneling dynamics of an initially trapped bosonic system comprised of different particle numbers N, varying from $N = 2$ to $N = 70$ particles, are compared. The delicate question, whether and how such studies with discretized space relate to scenarios in continuous space is in the focus of the present chapter. One case, where the mapping of a discretized BH simulation to several corresponding simulations and analytical predictions in continuous space was successful is Ref. [2]. Hence, the straightforward strategy to perform the comparison of the self-consistent continuous space methods

---

Electronic Supplementary Material Supplementary material is available in the online version of this chapter at http://dx.doi.org/10.1007/978-3-319-07085-8_4. Videos can also be accessed at http://www.springerimages.com/videos/978-3-319-07084-1.

A. U. J. Lode, *Tunneling Dynamics in Open Ultracold Bosonic Systems*,
Springer Theses, DOI: 10.1007/978-3-319-07085-8_4,

TDGP and MCTDHB with the discrete models BH and DNLS in this section is thus to apply the discrete-to-continuous-space-mapping of Ref. [2] to the potential given in Ref. [1] and solve the corresponding Schrödinger equation in continuous space (i.e., self-consistently) approximately by the TDGP and exactly by the MCTDHB method. The comparison will be done in terms of a quantitative comparison of the escape times and the coherence dynamics and many-body physics in the process.

4.1 Mapping of Discrete and Continuous Space Problems

Following Ref. [2], the many-body Hamiltonian of a one-dimensional Bose gas,

$$\hat{H} = \int dx \quad \hat{\Psi}^{\dagger} \left[-\frac{1}{2}\partial_x^2 + V(x) + \frac{g}{2}\hat{\Psi}^{\dagger}\hat{\Psi} \right] \hat{\Psi}, \tag{4.1}$$

where again $\hbar = m = 1$, can be transformed to the BHH, see Eq. (2.49), by replacing the integrals by sums and approximating the second spatial derivative in the kinetic energy operator with a difference quotient, i.e.,

$$\partial_x^2 \hat{\Psi} \approx \left[\hat{\Psi}(x_{j+1}) + \hat{\Psi}(x_{j-1}) - 2\Psi(x_j) \right] \cdot \frac{1}{2\Delta x^2}. \tag{4.2}$$

The parameters of the BHH, U and J, are then

$$J = \frac{1}{2\Delta x^2}; \qquad U = \frac{g}{\Delta x}. \tag{4.3}$$

In order to get a continuous version of a desired discrete BHH problem only the Δx in the above equation has to be chosen according to Ref. [2]. In Ref. [1] on the BHH and the DNLS, so-called hopping units are used, i.e., $J \equiv 1$ is set and all quantities are expressed in units of J. By this choice, in the mapping of Ref. [2], as outlined above, Δx and the interaction parameter g are defined and read

$$\Delta x = \frac{1}{\sqrt{2}}; \qquad g = U\Delta x = \frac{U}{\sqrt{2}}. \tag{4.4}$$

To define the many-body Hamiltonian which can be studied within the continuous TDGP and MCTDHB methods it remains to express the discrete potential V_i^{ext}, given in Ref. [1], as a function $V(x)$ in continuous x-space. The potential given in Fig. 1 of Ref. [1] is of rectangular shape for the initial state, i.e., at times $t < 0$,

$$V_i^{ext,t<0} = \begin{cases} \infty & \text{for } i \leq 0 \\ 0.05J & \text{for } i \geq x_s \\ 0 & \text{otherwise} \end{cases} \tag{4.5}$$

while for the time evolution

$$V_i^{ext,t\geq 0} = \begin{cases} \infty & \text{for } i \leq 0 \\ 0.05J & \text{for } x_s \leq i \leq x_e \\ 0 & \text{otherwise.} \end{cases} \quad . \tag{4.6}$$

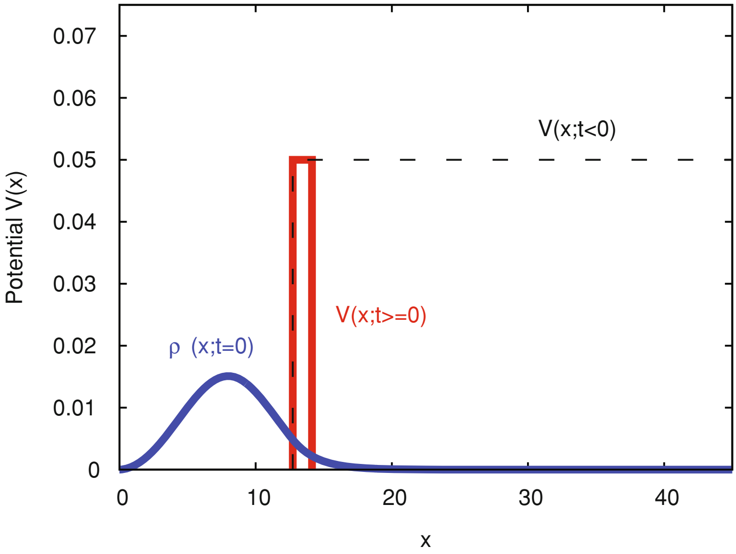

Fig. 4.1 Rectangular Continuous Space Potential for the Comparison of the DNLS, BH, TDGP and MCTDHB Approaches. The potential for the generation of the initial guess is given by the *black-dashed line* and the *red line* indicates the potential for the propagation. To guide the eye, an initial density, $\rho(x, t = 0)$, obtained from MCTDHB is plotted in *blue*. All quantities shown are in dimensionless units

Here x_s marks the start of the barrier and x_e the end of the barrier. Such rectangular potentials can be modeled conveniently by Heaviside step functions $\Theta(\cdot)$. Yet, to get the proper continuous space potential $V(x)$, the start/stop of the barrier, $x_{s/e}$, has to be translated via the specified $\Delta x = \frac{1}{\sqrt{2}}$. Finally, one obtains:

$$V(x; t < 0) = \begin{cases} \infty & \text{for } x \le 0 \\ 0.05 & \text{for } x \ge \frac{x_s}{\sqrt(2)} \\ 0 & \text{otherwise} \end{cases} \tag{4.7}$$

for the continuous space potential for the initial state and

$$V(x; t \ge 0) = \begin{cases} \infty & \text{for } x \le 0 \\ 0.05 & \text{for } \frac{x_s}{\sqrt(2)} \le x \le \frac{x_e}{\sqrt(2)} \\ 0 & \text{otherwise} \end{cases} \tag{4.8}$$

as the potential for the dynamics. For a plot of these potentials, see Fig. 4.1. This concludes the description of the mapping of discretized and continuous-space Hamiltonians in general and for the particular decay by tunneling example in Ref. [1]. For further details, see Ref. [2] and References therein.

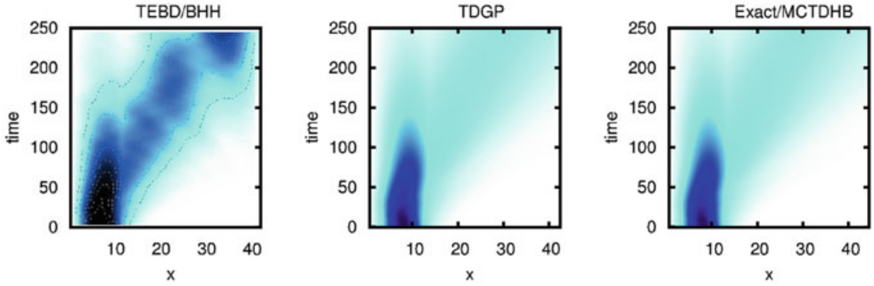

Fig. 4.2 BH, TDGP and Exact Density for the Decay by Tunneling of an Attractive System of 70 Bosons from a Rectangular Well.* The darker the color the bigger the particle density. The *left panel* (BH dynamics) shows more structure than the *middle* (TDGP) and the *right* one (MCTDHB). There is no noticeable difference between the TDGP and MCTDHB solutions. The data of the BH plot was extracted from Fig. 2b of Ref. [1] and is printed here with the permission of the authors of Ref. [1]. See Video 2 for the time-evolution of the spatial and momentum densities in the MCTDHB simulation depicted in the *right panel*. See text for further discussion

4.2 Comparison of DNLS, BH, TDGP and MCTDHB Dynamics

In order to compare the dynamics of the model Hamiltonians introduced in this section, i.e., the BH and the DNLS, with the TDGP description and the full many-body Schrödinger equation (solved exactly with MCTDHB) it is timely to first specify the interaction and the potential $V(x;t)$. For convenience, the parameters are chosen identically to the ones used to produce Fig. 3c of Ref. [1]: the interaction in this subsection is given by $\frac{UN}{J} = -0.15$ in discretized space and by $\lambda_0(N-1) = 0.15 \cdot \Delta x = \frac{0.15}{\sqrt{2}}$ in continuous space dimensionless units [cf. Eq. (4.4)]. Furthermore, the barrier is chosen from discretized $x_s = 18$ to $x_e = 20$—or, in continuous, dimensionless units from $\frac{18}{\sqrt{2}}$ to $\frac{20}{\sqrt{2}}$. With these parameters specified, the TDGP and MCTDHB dynamics *should* (in accordance with Ref. [2]) correspond to the respective DNLS and BH ones. It is instructive to first compare the time-evolution of the one-body density of the discrete systems with the continuous ones. For a plot of the BH, TDGP and exact density, see Fig. 4.2.

Qualitatively, the decay of the initially localized state is covered by all three theoretical approaches. It's very interesting to note that the middle and right panels of Fig. 4.2 which show the TDGP and exact MCTDHB solutions, respectively, are practically indistinguishable. This can only be the case if the dynamics are fully coherent, i.e., the correlation functions are all equal to 1 because all the particles occupy one single-particle state.

It's instructive to measure the decay times depicted in Fig. 3c of Ref. [1] for the DNLS and BHH models also with the continuous and self-consistent TDGP and MCTDHB methods in order to quantify how accurately the dynamics of the density $\rho(x,t)$ are captured. Figure 4.3 shows a plot of the nonescape times t_{esc} obtained with

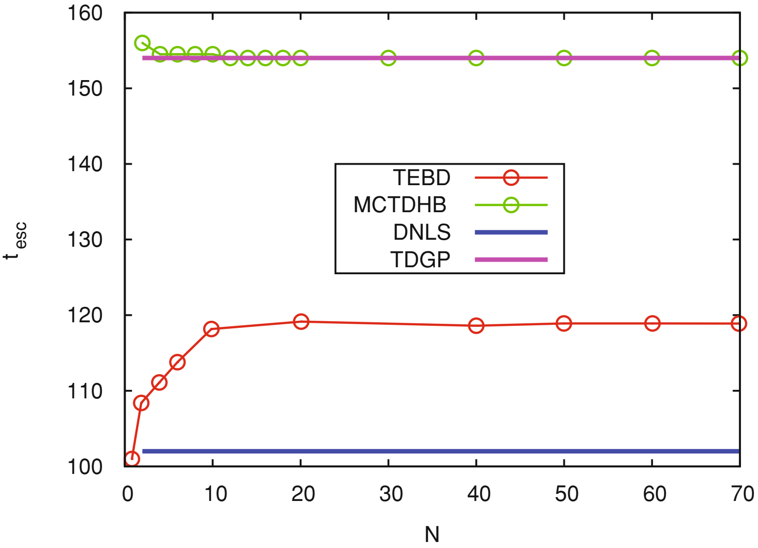

Fig. 4.3 Nonescape Times Obtained with the BHH/TEBD, DNLS, TDGP and Exact MCTDHB. The mean-field methods, DNLS and TDGP, do not distinguish different particle numbers. The many-body methods, TEBD/BHH and MCTDHB are sensitive to the particle number. The exact MCTDHB solutions differ only at the most by 1 % from the TDGP ones. The discrepancy of the continuous and self-consistent methods to the discrete ones is ∼50 % and ∼30 % for the DNLS and the TEBD/BHH, respectively. Both discrete methods, TEBD/BHH and DNLS seem to underestimate the escape times. Data points for TEBD/BHH and the DNLS have been extracted from Ref. [1]. See text for further discussion

the methods in question for various particle numbers between $N = 2$ and $N = 70$. The quantity t_{esc} is defined such that the integral $\int_{-\infty}^{x_e} dx\rho(x; t_{esc})$ is equal to e^{-1}.

From this figure one can read on one hand, that the many-body dynamics are very close to full coherence because of the close proximity of the escape times for the TDGP and the MCTDHB methods. On the other hand, it shows that the discrete methods TEBD/BHH and DNLS on the present example seem not to describe the escape by tunneling accurately. First, they underestimate the escape times (by 30 and 50 %, respectively) and second, the prediction of the many-body properties is qualitatively different: while the exact description reveals the full coherence of the process and the insensitivity of the escape times also to a change in the particle number N, a discrepancy of 20 % in the escape times t_{esc} is predicted between the DNLS and the TEBD/BHH. Hence, the TEBD/BHH description predicts a departure of the process from coherence, which is unphysical. This behavior underlines the importance of a self-consistent treatment of the many-boson problem in this case. The description with TEBD/BH and DNLS is qualitatively appropriate for the decay times but fails to capture the many-body features of the process.

To further corroborate the above statements and to investigate the dynamics of the coherence in the present example it is instructive to plot the first order correlation

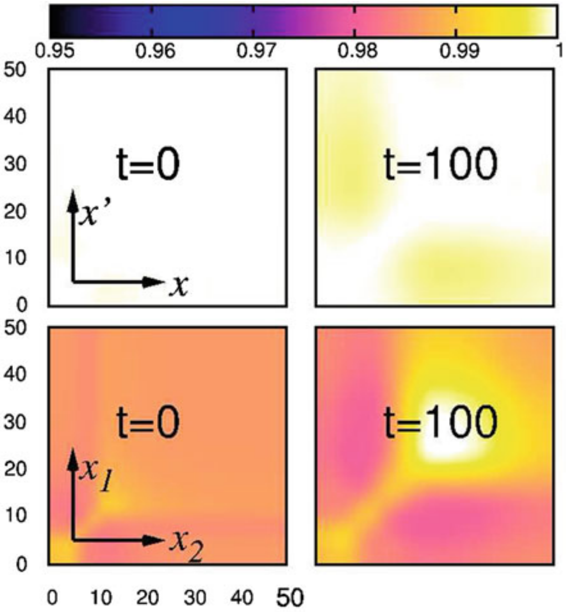

Fig. 4.4 Coherence of the Tunneling Process from Normalized Correlation Functions.* *Top Panels*: Normalized first-order correlation function $|g^{(1)}(x', x, t)|^2$ of $N = 70$ bosons for $t = 0$ and $t = 100$. The dynamics do not depart from coherence, i.e., $|g^{(1)}|^2 \approx 1$ holds for all space and time with a deviation not greater than 1 %. See text for further discussion. *Bottom Panel*: Diagonal of the normalized second-order correlation function $|g^{(2)}(x_1, x_2, t)|^2$ of $N = 70$ bosons for $t = 0$ and $t = 100$. The dynamics show almost full second-order coherence, i.e., $|g^{(2)}|^2 \approx 1$ holds for all space and time with a deviation not greater than 3 %. See Video 3 for the time-evolution of the normalized first- and second-order coherence computed with MCTDHB. See text for further discussion

function $g^{(1)}$. $|g^{(1)}|^2$ describes the fringe visibility in interference experiments and is, hence, a direct measure for the first order coherence. For the MCTDHB a plot of $g^{(1)}$ is provided in Fig. 4.4 in the two upper panels for representative times.

From the top panels of Fig. 4.4 it can be read that the process can indeed be viewed as fully first order coherent, as it was already inferred from the dynamics of the density in Fig. 4.2. This means that, to a very good approximation, one can apply the TDGP, i.e., a self-consistent continuous space mean-field description, to the process. It has, hence, no *collective* many-body characteristics which would result in a loss of coherence and a departure of $|g^{(1)}(x', x, t)|^2$ from 1. This is corroborated by the fact that the process is also almost completely second-order coherent, as it can be read from the graphs of $g^{(2)}$ in the bottom panels of Fig. 4.4. $g^{(2)}$ defines the bunching or anti-bunching properties of a quantum field [3–5]. If $g^{(2)}$ is larger than unity, the particles are likely to be in these positions together and if $g^{(2)}$ is smaller than unity, the particles are unlikely to be in the these positions together. The former situation is referred to as bunching and the latter situation is referred to as anti-bunching. The plots in Fig. 4.4 show that the tunneling process does not show any bunching or anti-bunching characteristics and is, hence, fully second-order coherent. Reference [1] attributes the differences found between the two discrete DNLS and BHH models to a "many-body nature of the process". Further, Ref. [1] concludes that the "study shows that many-body effects in macroscopic quantum tunneling can be observed via number fluctuations and density-density correlations as well as the increased escape time". This is of course true only when one uses the discretized models TEBD/BH or DNLS and in that implies a tight-binding single-band lattice potential. The self-consistent continuous space TDGP and MCTDHB treatment shows, that it is difficult to which continuous space potential's dynamics to attribute these discrete model descriptions to.

The lattice/discrete models that have been applied in Ref. [1], i.e., the DNLS and TEBD, expand the governing Hamiltonian in a basis which is time-independent and adapted to a situation in which there is a periodic potential for which the lowest band and nearest neighbor coupling is a sufficient description. The potential that Ref. [1] suggests to treat (cf. Fig. 1 in Ref. [1]), *is not* a continuous space potential. It solely shows the on-site offset of the lattice potential considered. The dynamics in continuous space are different and the effects found in Ref. [1] do not correspond to a continuous space scenario of the many-boson tunneling process to open space. These dynamics correspond rather to bosons in a deep optical lattice of which one cannot straightforwardly recover a continuous space form. The mapping of reference [2] is not applicable in the tunneling process considered here and in [1] because the lattice potential implied by the usage of the TEBD/BHH and DNLS treatment has a considerable influence on the dynamics. In summary, the DNLS and BHH treatment of the problem of many-boson tunneling to open space with the current setup yields qualitative descriptions of which the predicted many-body features are not reliable. The self-consistency and a faithful description of continuous space seems to be of great importance in tunneling to open space scenarios.

References

1. J.A. Glick, L.D. Carr, Macroscopic Quantum Tunneling of Solitons in Bose–Einstein Condensates. ArXiv e-prints (May 2011). ArXiv:1105.5164
2. B. Schmidt, M. Fleischhauer, Exact numerical simulations of a one-dimensional trapped Bose gas. Phys. Rev. A **75**, 21601 (2007)
3. R. Hanbury Brown, R.Q. Twiss, A Test of a New Type of Stellar Interferometer on Sirius. Nature **178**(1046), 1956 (1048)
4. R. Hanbury Brown, R.Q. Twiss, Interferometry of the Intensity Fluctuations in Light. I. Basic Theory: The Correlation between Photons in Coherent Beams of Radiation. Proc. Roy. Soc. Lond. A **242**(1230), 300324 (1957)
5. R. Hanbury Brown, R.Q. Twiss, Interferometry of the Intensity Fluctuations in Light. II. An Experimental Test of the Theory for Partially Coherent Light. Proc. Roy. Soc. Lond. A **243**(1234), 291319 (1958)

Chapter 5
Theoretical Considerations and Analytical Models on the Many-Body Physics of Tunneling Bosons

> *All you really need to know for the moment is that the universe is a lot more complicated than you might think, even if you start from a position of thinking it's pretty damn complicated in the first place.*
>
> Douglas Adams, Mostly Harmless

In this Chapter, various (analytical) model consideration and general characteristics of the methods introduced in Chap. 2 are discussed. This is done in order to put the later numerical results in a wider context and to familiarize the reader with the key concepts of the quantum many-boson dynamics of tunneling to open space. The first part of this Chapter is a proof that the TDGP does not account for correlations and coherence properly. In the second part the physics of tunneling are assessed from a many-body point of view by including correlations and coherence. This is done by starting out from basic assumptions on the orbitals assembling the basis of many-boson Hilbert space or a possible decomposition of the Hilbert space of the considered dynamics. The following considerations are specified for one-dimensional systems and the respective labeling of variables, i.e., x, and k, instead of $\vec{r}$, and $\vec{k}$, is used. Note that this restriction is for simplicity and the considerations can be generalized to two- and three-dimensional systems in a straightforward manner.

5.1 Analytical Considerations within the Gross–Pitaevskii Approximation

In the TDGP approximation a wave packet of a System is constructed by a product of a single orbital with different spatial coordinates and proper normalization. Thus TDGP is built upon the assumption that all bosons reside in one single quantum state which is directly equivalent to the statement that the bosons form a *fully coherent condensate*. The normalized Ansatz for the wave function reads:

A. U. J. Lode, *Tunneling Dynamics in Open Ultracold Bosonic Systems*,
Springer Theses, DOI: 10.1007/978-3-319-07085-8_5,

$$\Psi_{GP}(x_1, \ldots, x_N, t) = \prod_{k=1}^{N} \Phi(x_k, t). \tag{5.1}$$

When one plugs this GP ansatz for the wave function, Ψ_{GP}, in the definition of the RDM $\rho^{(1)}$, see Eq. (2.24), it reads (the dependency on time is henceforward omitted where appropriate to simplify the reading):

$$\begin{aligned}
\rho^{(1)}(x_1 \mid x_1^{'}) &= \frac{N!}{(N-1)!} \int \Psi_{GP}(x_1, \ldots, x_N) \cdot \Psi^*_{GP}(x_1^{'}, x_2, \ldots, x_N) dx_2 \cdots dx_N \\
&= \frac{N!}{(N-1)!} \int \left(\prod_{k=1}^{N} \Phi(x_k) \right) \left(\Phi^*(x_1^{'}) \right) \left(\prod_{k=2}^{N} \Phi^*(x_k) \right) dx_2 \cdots dx_N \\
&= N \cdot \Phi(x_1) \cdot \Phi^*(x_1^{'}).
\end{aligned} \tag{5.2}$$

This RDM is simply a product of the orbital Φ at x_1 and its complex conjugate at $x_1^{'}$.

To determine what are the implications for the coherence properties of such a wave function, it is instructive to compute from the found RDM, Eq. (5.2), the correlation functions of the TDGP ansatz. The first order correlation function $g^{(1)}(x_1, x_1^{'})$ reads:

$$g^{(1)}(x_1, x_1^{'}) = \frac{\rho^{(1)}(x_1 \mid x_1^{'})}{\sqrt{\rho^{(1)}(x_1 \mid x_1) \cdot \rho^{(1)}(x_1^{'} \mid x_1^{'})}} \tag{5.3}$$

$$= \frac{\Phi(x_1) \cdot \Phi^*(x_1^{'})}{\sqrt{\Phi(x_1^{'}) \cdot \Phi^*(x_1^{'}) \cdot \Phi(x_1) \cdot \Phi^*(x_1)}} \tag{5.4}$$

$$|g^{(1)}(x_1, x_1^{'}; t)| = 1 \quad \forall\, x_1, x_1^{'}, t. \tag{5.5}$$

Intuitively, Eq. (5.5) is already clear from the way the GP-ansatz for the wave function is constructed. The TDGP theory has no feature for first order decoherence because the first order correlation function will always be independent of the spatial coordinates and constant within this model. This is because the denominator and nominator of $g^{(1)}$ are always a product of a *single* complex valued function (the orbital). The diagonal of the two-body reduced density matrix, i.e., the two-body density is obtained analogously:

$$\begin{aligned}
\rho^{(2)}(x_1, x_2 \mid x_1^{'}, x_2^{'}) = \frac{N!}{(N-2)!} \int \quad & \Psi_{GP}(x_1, \ldots, x_N) \cdot \\
& \Psi^*_{GP}(x_1^{'}, x_2^{'}, x_3, \ldots, x_N) dx_3 \cdots dx_N.
\end{aligned}$$

Which once again can only be the product of a *single* complex valued function: the orbital in the TDGP-ansatz. The diagonal of $\rho^{(2)}$ reads:

$$\rho^{(2)}(x_1, x_2 \mid x_1, x_2) = N(N-1) \mid \Phi(x_1) \mid^2 \cdot \mid \Phi(x_2) \mid^2 . \tag{5.6}$$

The two-body density is a product of the same complex valued function as the RDM and hence the two-body density is a product of one-body densities. This accounts for the fact that the system in this model is bound to be *condensed*.

The higher order coherence is measured by a system's n-th order correlation function $|g^{(n)}|^2$ (see e.g. [1, 2]). If it is close to (far from) 1, the system is n-th order coherent (incoherent). The fact that the GP wave function is constructed as a product of one orbital yields that all-order RDMs are also constructed of the same orbital. As the correlation functions are ratios of different RDMs, the first order correlation function is bound to be $|g^{(1)}|^2 = 1$ everywhere at any time. Similarly, the n-th $(n > 1)$ order correlation function is bound to be constant everywhere at any time. One can obtain this from writing down $g^{(p)}(x_1, \ldots, x_p|x_1^{'}, \ldots, x_2^{'})$ in terms of bosonic field creation and annihilation operators $\hat{\Psi}(x)$, $\hat{\Psi}^\dagger(x)$:

$$\hat{\Psi}(x)|N;t\rangle = \sqrt{N}\Phi(x,t)|N-1;t\rangle \quad \hat{\Psi}^\dagger(x)|N;t\rangle = \sqrt{N}\Phi^*(x,t)|N+1;t\rangle. \tag{5.7}$$

Therefore the p-th order normalized correlation function reads:

$$\begin{aligned} g^{(p)} &= \frac{\rho^{(p)}(x_1, \ldots, x_p|x_1^{'}, \ldots, x_p^{'})}{\sqrt{\prod_{\xi=1}^{p} \rho^{(1)}(x_\xi|x_\xi)\rho^{(1)}(x_\xi^{'}|x_\xi^{'})}} \qquad (5.8)\\ &= \frac{\langle\Psi(t)|\hat{\Psi}^\dagger(x_1^{'})\ldots\hat{\Psi}^\dagger(x_p^{'})\hat{\Psi}(x_p)\ldots\hat{\Psi}(x_1)|\Psi(t)\rangle}{\prod_{\xi=1}^{p}\left(\sqrt{\langle\Psi(t)|\hat{\Psi}^\dagger(x_\xi)\hat{\Psi}(x_\xi)|\Psi(t)\rangle\langle\Psi(t)|\hat{\Psi}^\dagger(x_\xi^{'})\hat{\Psi}(x_\xi^{'})|\Psi(t)\rangle}\right)}. \end{aligned}$$

For convenience, some time-dependencies have been omitted in Eq. (5.8). Recalling the commutation relations of bosonic field operators

$$\left[\hat{\Psi}(x_i), \hat{\Psi}^\dagger(x_j)\right] = \delta(x_i - x_j), \quad \left[\hat{\Psi}(x_i), \hat{\Psi}(x_j)\right] = 0, \tag{5.9}$$

one finds, as before, for the diagonal of the first order RDM:

$$\langle\Psi(t)|\hat{\Psi}^\dagger(x)\hat{\Psi}(x)|\Psi(t)\rangle = N|\Phi(x)|^2. \tag{5.10}$$

The above diagonal of the one-body RDM, needed for the denominator of Eq. (5.8) within the TDGP approximation, makes $g^{(p)}$ take on the form:

$$g^{(p)} = \frac{\langle\Psi(t)|\hat{\Psi}^\dagger(x_1^{'})\ldots\hat{\Psi}^\dagger(x_p^{'})\hat{\Psi}(x_p)\ldots\hat{\Psi}(x_1)|\Psi(t)\rangle}{\sqrt{\prod_{\xi=1}^{p}\left(N|\Phi(x_\xi)|^2 \cdot N|\Phi(x_\xi^{'})|^2\right)}}. \tag{5.11}$$

Also the numerator of Eq. (5.8) can be evaluated with the help of Eq. (5.7). $g^{(p)}$ then reads:

$$\begin{aligned} g^{(p)} &= \frac{\prod_{\xi=1}^{p}\left(\sqrt{(N+1-\xi)}\Phi(x_\xi)\sqrt{(N+1-\xi)}\Phi(x'_\xi)\right)}{N^p \prod_{\xi=1}^{p}\sqrt{\left(|\Phi(x_\xi)|^2 \cdot |\Phi(x'_\xi)|^2\right)}} \\ &= \frac{N\cdot(N-1)\cdots(N-p)}{N^p} = \frac{N!}{N^p \cdot p!}. \end{aligned} \tag{5.12}$$

When one considers an interacting many-body system whose dynamics is most likely described by a time-dependent wave function of big complexity, this result would be at least surprising. A constant correlation function of any order, everywhere at any time is equivalent to the statement that the wave packet, from which it was derived, has defined, constant coherence properties for all times and everywhere. This, of course is only a good model if one wishes to describe phenomenologically a Bose–Einstein condensate, which is in a good approximation, a coherent many-body object. This result clarifies the fact, that the TDGP model will fail to describe the dynamics and effects of first or higher order (anti-)correlations and first or higher order coherence or decoherence. Furthermore, a nice way to analyze the dynamics of many-boson systems starts from the above considerations: if one finds a deviation (in whatever quantity) of a many-boson system from the approximative description with the TDGP approximation, this means that the system is no longer fully coherent and its correlation functions impact its physics.

5.2 Analytical Considerations Beyond Gross–Pitaevskii

5.2.1 Decomposition of Hilbert Space into Subspaces

As found in many cases of the dynamics of ultracold bosons, initially coherent states develop fragmentation throughout their dynamics, see e.g. Refs [3–5]. In this section an analytical model is constructed for the dynamics one would expect if an initially coherent and parabolically trapped system tunnels to open space with two momenta k_1 and k_2 involved in the process. As a first step it is instructive to consider the full Hilbert space of the problem as partitioned in an inside part and an outside part. Then one pursues a description of the tunneling process which covers the fragmentation in the interior subspace containing initially the main part of the density *and* fragmentation in the exterior subspace which initially contains the lesser fraction of the density outside the well.

By making this assumption on the partitioning of space, one assumes that the system is completely separable, i.e., lives in two orthogonal subspaces P (the interior) and Q (the exterior). The wave function in P, Ψ_P, is an (a linear combination of) eigenfunction(s) of the Hamiltonian

$$\hat{H}_P = \hat{P}\left\{\sum_{i=1}^{N}\left[-\frac{1}{2}\partial_{x_i}^2 + \frac{1}{2}x_i^2\right] + \sum_{j<k}\hat{W}(x_j - x_k)\right\} \tag{5.13}$$

on the P subspace and the wave function Ψ_Q is an (a linear combination of) eigenfunction(s) of the Hamiltonian $\hat{H}_Q = \hat{Q}\{\sum_{i=1}^{N}\left[-\frac{1}{2}\partial_{x_i}^2\right] + \sum_{j<k}\hat{W}(x_j - x_k)\}$ on the Q subspace - here $\hat{P}$, $\hat{Q}$ denote the projectors onto the orthogonal subspaces. Obviously, one can write the whole Hilbert space of the system then as a direct sum of P and Q: $\mathcal{H} = P \oplus Q$. In fact one can write down the wave function Ψ of this separable problem. If one assumes that the only effect of the interparticle interaction potential $\hat{W}$ in Q is to force the system to occupy two eigenfunctions of the kinetic energy operator (i.e. two plane waves), it is obvious that the difference of the two momenta, k_1 and k_2 must relate to the interaction. In P the wave function can be described by *mollifying* the Gaussian constructing, together with the Hermite polynomials K_n, the eigenfunctions of the parabolic trap in P. Hence, the following wave function is obtained:

$$|\Psi_P(t)\rangle = \sum_{\vec{n}_P}\left(\hat{p}_1^\dagger(t)\right)^{N_{q_1}}\cdots\left(\hat{p}_M^\dagger(t)\right)^{N_{M_p}}|vac\rangle \tag{5.14}$$

$$|\Psi_Q(t)\rangle = \sum_{\vec{n}_Q}\left(\hat{q}_1^\dagger(t)\right)^{N_{p_1}}\cdots\left(\hat{q}_M^\dagger(t)\right)^{N_{M_q}}|vac\rangle \tag{5.15}$$

$$|\Psi(t)\rangle = |\Psi_Q\rangle \otimes |\Psi_P\rangle \tag{5.16}$$

$$\Rightarrow \Psi(x_1, \ldots, x_N, t) = \Psi_P(x_1, \ldots, x_{N_P}, t)\Psi_Q(x_1, \ldots, x_{N_Q}, t). \tag{5.17}$$

Where the vector of all possible configurations of N_P/N_Q bosons over M_ξ orbitals, $\vec{n} := \left(N_1, \ldots, N_{M_\xi}\right)$; $\{N_i | \sum_{k=1}^{M_\xi} N_k = N_\xi; \xi = P, Q\}$, the P and Q subspace boson creation operators for the i-th orbital $\{\hat{q}_i^\dagger(t), \hat{p}_i^\dagger(t)\}$, the numbers of bosons in P and Q, N_P and N_Q, the number of orbitals to represent the wave function in P and Q, M_P and M_Q, and the vacuum state $|vac\rangle$ have been used. If one represents this in the Fock-space notation for the P-subspace, i.e. $|n_1, n_2, \ldots\rangle$, where one omits the P-subscripts for the sake of simplicity, one gets:

$$\hat{p}_k^\dagger(t)|vac\rangle = \hat{P}e^{-i\varphi_k t}K_{k-1}(x)e^{-\frac{x^2}{2}w_k}|0, \ldots, 0, \underbrace{1}_{\text{k-th position}}, 0, \ldots\rangle$$

$$K_0 = 1\ ;\ K_1(x) = x\ ;\ K_{n+1} = xK_n(x) - K_{n-1}(x)\ ;\ \hat{P} = \Theta(x - x_P) \tag{5.18}$$

$$\Rightarrow \hat{p}_1^\dagger(t)|vac\rangle = \hat{P}e^{-i\varphi_1 t}e^{-\frac{x^2}{2}w_1}|1, 0, \ldots\rangle \tag{5.19}$$

$$\hat{p}_2^\dagger(t)|vac\rangle = \hat{P}e^{-i\varphi_2 t}xe^{-\frac{x^2}{2}w_2}|0, 1, 0, \ldots\rangle \tag{5.20}$$

$$\vdots$$

In a further analytical considerations the $\{w_i\}$ could be e.g. determined by minimizing the energy functional with respect to these parameters. The tunneled density in Q is forged from creation operators $\hat{q}_k^\dagger$. Because the potential in the Q subspace is assumed to have no structure (i.e. it is constant) and the absolute density is small, it is timely to neglect the interaction part $W(x_i - x_j)$ of the Hamiltonian H_Q, i.e.,

$$\hat{H}_Q = \hat{Q} \sum_{i=1}^{N} \left[-\frac{1}{2} \partial_{x_i}^2 \right]. \tag{5.21}$$

Under this assumption the $\hat{q}_k^\dagger$ operators create plane waves, the eigenfunctions of the kinetic energy operator. Basically, in modeling the density this way one implies that the interaction forces the bosons to occupy more than one state macroscopically. This is quite easy for the bosons as there is no potential but their repulsive interactions. Still, the interactions are weak enough such that the shape of the eigenfunctions of $\hat{H}_Q$ is the same as if there was no repulsion. Hence, the eigenfunctions are very close to those of free, noninteracting particles and are plane waves, therefore. This assumption is justified only for weak interactions and when the density in the Q subspace is small. Hence, one can write for the action of the $\hat{q}_k^\dagger$, while omitting the Q-subscripts for the permanents for simplicity:

$$\hat{q}_j^\dagger(t)|vac\rangle = \hat{Q} e^{-i\nu_j t} e^{-ik_j x} = \hat{Q}|0, \ldots, 0, \underbrace{1}_{\text{j-th position}}, 0, \ldots\rangle. \tag{5.22}$$

Here, too, the only time dependence inherits in a phase factor. Now all the ingredients to write down the wave function of the whole system, $|\Psi\rangle = |\Psi_P\rangle \otimes |\Psi_Q\rangle$ are at hand. As an example the model wave function for the case of two natural orbitals describing the Q and one modeling the P subspace is given below.

$$|\Psi\rangle = \sum_{\vec{n}_p, \vec{n}_q} C_{\vec{n}_p} C_{\vec{n}_q} \left(\hat{p}_1^\dagger(t)\right)^{N_p} \left(\hat{q}_1^\dagger(t)\right)^{N_{q_1}} \left(\hat{q}_2^\dagger(t)\right)^{N_{q_2}} |vac\rangle. \tag{5.23}$$

Here, the coefficients $C_{\vec{n}_i}$ for the $i = P, Q$ subspace-configurations, and the combined vacuum $|vac\rangle = |vac\rangle_Q |vac\rangle_P$ were used. $\vec{n}_p = (N_P) = (N - N_Q)$ has to hold because there is only one natural orbital for the condensate inside the trap and $\vec{n}_q = (N_{q_1}, N_{q_2}) = (N_{q_1}, N_Q - N_{q_1})$ has to hold as one uses two orbitals for the outside region.

The above considerations feature several nice physical properties. The tunneling process from the P to the Q subspace can be described in this model even if the escaping particles have several different momenta and even if the trapped bosons form a (locally) fragmented object (see Appendix B for a concise definition of local fragmentation/coherence). The density of the considered wave functions resembles a sample of parabolically trapped bosons in P and interfering plane waves with different momenta on the exterior Q. In the specific case introduced in Eq. (5.23), one finds a locally condensed fraction in P and an interference pattern formed by permanents built from two plane waves with momenta k_1 and k_2 in Q—which is in general (locally) fragmented, i.e., not coherent. The spatial density of the wave function in Eq. (5.23) is a spatially extended oscillatory part in Q and a Gaussian part in the interior P. The momentum density of such a wave function will be a convolution of a structure peaked at k_1 and k_2 from the exterior part of the wave function and a Gaussian part from the trapped, interior part of the wave function. It is timely to stress here, that these features were found in the numerically exact simulations (discussed in Chaps. 6 and 7) and it is hence justified to look at the problem in this way. Of course, all the above considerations do not account properly for the tunneling dynamics. The dynamics are caused by a coupling of the P and Q spaces which makes the particle numbers N_Q and N_P time-dependent. To account for such a coupling the model Hamiltonian needed to be modified. The above form is block-diagonal. To include the dynamics one needed to introduce a coupling of the P to the Q block. Yet, the presented considerations will be helpful to analyze the many-boson tunneling process from the point of view of the energetics of the interior and exterior subsystems. The energies can be approximately found from the above Hamiltonians $\hat{H}_P$ and $\hat{H}_Q$.

5.2.2 *Model for the Energetics of the Many-Body Physics of Tunneling to Open Space*

Starting from the model in the previous section it is interesting to consider and formulate the consequences for the physics from the point of view of the energies which particles have in the interior or exterior part of space. Basically, the model in this subsection comes from the de facto splitting of space by a barrier in tunneling processes. The idea introduced and formalized above and applied here is to indeed consider the *interior* and *exterior* subsystems as separate (interacting) many-boson systems and find the physics that are to be expected. The strategy pursued is to assemble the many-body process from basic transfer processes of single particle or multiple particles. To analyze these basic transfer processes the above defined Hamiltonians' $\hat{H}_P$, $\hat{H}_Q$, cf. Eqs. (5.13), (5.21), eigenfunctions and corresponding energies are used. For convenience, the interior, P-subspace is referred to as "IN" subspace and the exterior, Q-subspace is referred to as the "OUT" subspace.

5.2.2.1 Basic Static Processes Assembling the Many-Body Physics

The initial and final physical situations in the "IN" and "OUT" subspaces are intuitively clear. The totally condensed initial state lives in the "IN" region and is confined by a harmonic potential. Therefore, it can be described by a harmonic oscillator-like product state, cf. e.g. Ref. [6]. In the final state all the bosons have tunneled out

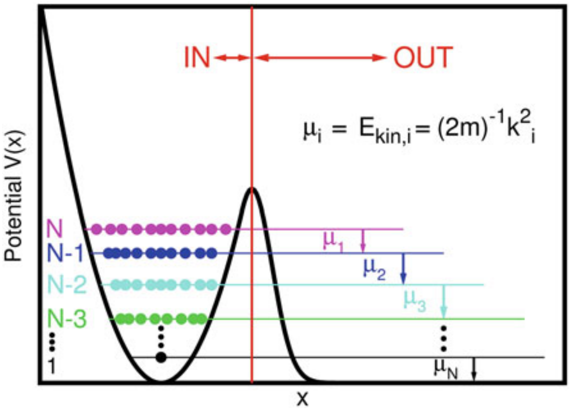

Fig. 5.1 Sequential Mean-Field Scheme to Model the Tunneling Processes. The bosons are ejected from the "IN" to the "OUT" subspace (indicated by the red line). The chemical potential μ_i is converted to kinetic energy $E_{kin,i}$. *All* the momenta corresponding to the chemical potentials $k_i = \sqrt{2mE_{kin,i}} = \sqrt{2m\mu_i}$; $i = N, N-1, \ldots, 1$ appear in the momentum distribution, see Figs. 6.4, 6.8, 6.9. All quantities shown are dimensionless

and live entirely in the semi-infinite "OUT" region. According to Ref. [7] the static many-body solution of the one-dimensional bosonic system with short range repulsive interaction on a semi-infinite axis can be constructed as a linear combination of many correlated (incoherent) states. This implies that the dynamical final state of our system is incoherent.

To model the steps translating the fully coherent systems to complete incoherence, let us first consider the situation in which exactly one boson has tunneled through the barrier from "IN" to "OUT" and has no more connection with the interior. The "IN"-system now has $N-1$ particles and the "OUT"-system has 1 particle. By assuming that no excitations have been produced in the "IN"-system, the trapped bosons' energy is exactly reduced by the chemical potential $\mu_1 = E^N - E^{N-1}$, see Fig. 5.1.

Here E^i is the energy of the trapped harmonic oscillator product state with the distribution of i bosons in the "IN" subspace. One assumes that the chemical potential does not depend on the number of emitted bosons, because in "OUT" $V(x) \approx 0$. Let us further ignore the inter-particle interaction in the exterior system. Energy conservation requires then, that the chemical potential μ_1 of the first boson tunneled from the "IN" to the "OUT" region must be converted to kinetic energy. A free particle has the kinetic energy $E_{kin} = \frac{k^2}{2m}$. We thus expect the first emitted boson to have the momentum $k_1 = \sqrt{2mE_{kin,1}} = \sqrt{2m\mu_1}$. The above considerations imply that the many-body wave function can be considered in a localized basis $|IN; OUT\rangle$. The process of emission of the first boson in this basis reads $|N; 0\rangle \rightarrow |N-1; 1^{k_1}\rangle$. Here the k_1 superscript indicates that the emitted boson occupies a state which is very similar to a plane wave with momentum k_1 in the

"OUT" subspace. Now one can prescribe the process of the emission of the second boson as $|N-1;1^{k_1}\rangle \rightarrow |N-2;1^{k_1},1^{k_2}\rangle$. By neglecting the interactions between the first and second emitted bosons we can define the second chemical potential as $\mu_2 = E_{IN}(N-1) - E_{IN}(N-2)$. Thus, a second kinetic energy $E_{kin,2} = \mu_2$ gives rise to the momentum peak at $k_2 = \sqrt{2m\mu_2}$. Generally, the chemical potentials of the systems made of $N-i$ and $N-i-1$, $i = 0, \ldots, N-1$, particles are different, so the corresponding peaks should appear at different positions in the momentum spectra. One can continue to apply the above scheme until the last boson is emitted $|1;1^{k_1}\cdots 1^{k_{N-1}}\rangle \rightarrow |0;1^{k_1}\cdots 1^{k_N}\rangle$. Figure 5.1 indicates the chemical potentials for these one-particle mean-field processes by horizontal lines and the processes by the vertical arrows. This simplified mean-field picture of the tunneling dynamics is analogous to N processes of ionization, where the momenta of each independent process or channel are defined by the chemical potential of the respective sources made of N, $N-1$, $N-2$, etc. particles.

5.2.3 *Model with Two Momenta from Single-Particle States*

After the previous sections' presented considerations on the mechanism in many-boson tunneling to open space, the present paragraph is to shed light on the shape and properties of the wave functions and densities of the process. It was found, that the situation in the exterior is well-described by a discrete peak-structure in the momentum distribution and the situation in the interior is well-described by a coherent, Gaussian-like density. Such a situation can be straightforwardly modeled by constructing a many-boson wave function from the following two single-particle states:

$$\phi_1 = \mu(x) + \theta(x-C)e^{ik_1x} \quad ; \quad \phi_2 = \nu(x) + \theta(x-C)e^{ik_2x}. \tag{5.24}$$

$\mu(x)$, $\nu(x)$ are assumed to be localized inside the well such that $\mu(x) = \nu(x) \approx 0$ if $x > C$ holds.

From here on it remains only to derive the two particle RDM with this density after symmetrizing it. For this lengthy but straight forward calculation as well as the definition of the coefficients we refer the reader to Appendices D, E and display only the result for the diagonal of the two-body RDM, $diag(\rho^{(2)})$, here:

$$\begin{aligned} diag(\rho^{(2)}) = A & \left[\hat{P} C_{N_P} C^*_{N_P} \exp\left(-w\left(x_1^2+x_2^2\right)\right)\right] \\ \times B \quad & \hat{Q}\Big(|C_{2,0}|^2 + |C_{0,2}|^2 + |C_{1,1}|^2 \\ & + \alpha \cos((k_2-k_1)(x_2-x_1)) \\ & + \beta \cos\left(\frac{(k_2-k_1)(x_1+x_2)}{2}\right)\cos\left(\frac{(k_2-k_1)(x_1-x_2)}{2}\right)\Big) \end{aligned} \tag{5.25}$$

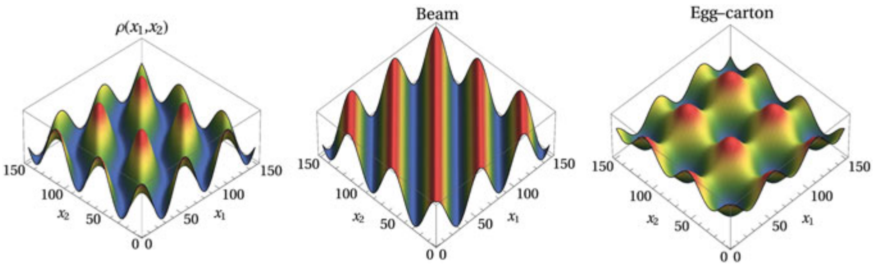

Fig. 5.2 Structures in the Two-Body Density of a Two-Momentum Tunneling Process. The *left* plot shows the two-body density with equal coefficients, the *middle* plot shows the beam pattern, and the *right* one the egg-carton pattern. It is evident, that the tunneling dynamics which incorporate two momenta rather than a single momentum must have an interesting structure in their two-body density and correlations

One ends up having three main parts of the diagonal of the reduced two-body density matrix, a beam pattern which is weighted by α, an egg-carton pattern, weighted by β and the trapped part of the density which resembles a condensate wave function of a parabolic trap. See Fig. 5.2 for a plot of the structure.

The two-body correlation function, $g^{(2)}$, can also be calculated within this model, it is deferred to Appendix F. This model does not include the decay dynamics so far, but one could do this by adding a negative complex term $-i\Gamma_P$ to the Hamiltonian operator for the interior space which will result in an exponential decay with the rate $\exp(-\Gamma)$. Then, to keep the total wave function normalized it would be necessary to include another complex part in the exterior subspace, i.e. add $+i\Gamma$ in the exterior. Yet, the above model consideration nicely shows—with very basic assumptions on the one-particle states—how an intricate bunching and antibunching [8–10] structure must arise in the tunneling of systems with more than one momentum.

To conclude this section, it remains to mention that a reformulation of the above model is possible using a single-particle basis which consists in functions which are products of a function in the interior and the plane wave exterior part:

$$\phi_1 = \mu(x) \cdot e^{ik_1 x} \quad ; \quad \phi_2 = \mu(x) \cdot e^{ik_2 x}. \tag{5.26}$$

This ansatz is somewhat more realistic, because it turned out that in all the numerical computations presented in the later Chaps. 6 and 7, the natural orbitals are delocalized and have a shape like the one in Eq. (5.26). Explicitly, the orbitals have very similar Gaussian like structures in the interior part of space, i.e., $\mu(x) \propto e^{-\frac{x^2}{2}}$. The calculation of the full densities $\rho^{(1)}$ and $\rho^{(2)}$ is a bit more cumbersome and lengthy and is, like the results of it, deferred to the Appendix G. In essence, its two-body density $\rho^{(2)}$ is the one of the above model (cf. Eq. (5.24)), but decaying exponentially in space. One important advantage is, that the model in Eq. (5.26) and Appendix G reproduces also the natural occupations, $\rho^{(NO)}_{1/2}$, of the numerical simulations reliably. It is interesting to note here, that it's in principle also possible to construct densities and momentum distributions with almost identical features from coherent product states (see Appendix C). Although these coherent model densities are seemingly correct, they do not capture the many-body features and the wave function in the process as obtained numerically exactly in the following Chaps. 6 and 7. The fragmented states in this Chapter and Appendix G are the ones that contribute to the dynamics in the system. This is due to the TDVP selecting states that minimize the action [11]—such states are hence delocalized and fragmented ones in the case of many-body tunneling to open space.

References

1. U.M. Titulaer, R.J. Glauber, Correlation Functions for Coherent Fields. Phys. Rev. **140**, B676 (1965)
2. R.J. Glauber, The Quantum Theory of Optical Coherence. Phys. Rev. **130**, 2529 (1963)
3. A.U.J. Lode, K. Sakmann, O.E. Alon, L.S. Cederbaum, A.I. Streltsov, Numerically exact quantum dynamics of bosons with time-dependent interactions of harmonic type. Phys. Rev. A **86**, 063606 (2012)
4. I. Březinová, A.U.J. Lode, A.I. Streltsov, O.E. Alon, L.S. Cederbaum, J. Burgdörfer, Wave chaos as signature for depletion of a Bose–Einstein condensate. Phys. Rev. A **86**, 013630 (2012)
5. A.U.J. Lode, A.I. Streltsov, K. Sakmann, O.E. Alon, L.S. Cederbaum, How an interacting many-body system tunnels through a potential barrier to open space. Proc. Natl. Acad. Sci. USA **109**, 13521 (2012)
6. L.P. Pitaevskii, S. Stringari, *Bose–Einstein Condensation* (Oxford University Press, Oxford, 2003)
7. M. Gaudin, Boundary Energy of a Bose Gas in One Dimension. Phys. Rev. A **4**, 386–394 (1971)
8. R.H. Brown, R.Q. Twiss, A Test of a New Type of Stellar Interferometer on Sirius. Nature **178**, 1046–1048 (1956)
9. R.H. Brown, R.Q. Twiss, Interferometry of the intensity fluctuations in light. I. Basic theory: the correlation between photons in coherent beams of radiation. Proc. Roy. Soc. London A **242**(1230), 300–324 (1957)
10. R.H. Brown, R.Q. Twiss, Interferometry of the intensity fluctuations in light. II. An experimental test of the theory for partially coherent light. Proc. Roy. Soc. London A **243**(1234), 291–319 (1958)
11. P. Kramer, M. Saraceno, *Geometry of the Time-Dependent Variational Principle* (Springer, Heidelberg, 1981)

Chapter 6
Tunneling of a Many-Boson System to Open Space Without a Threshold

> *There is a theory which states that if ever anyone discovers exactly what the Universe is for and why it is here, it will instantly disappear and be replaced by something even more bizarre and inexplicable. There is another theory which states that this has already happened.*
>
> Douglas Adams, The Restaurant at the End of the Universe

The scope of this chapter is to analyze the tunneling process of initially parabolically trapped many-boson systems to open space. A scheme of the process is depicted in Fig. 6.1. In order to really observe a tunneling process the energy of the system has to have a value such that the one-body potential $V(x, t)$ has *classically forbidden* as well as *classically allowed* domains. In the numerical example considered the energies per particle are close to $\epsilon \approx \frac{1}{2}$ and the height of the barrier is ≈ 2.26. This makes the potential well and the asymptotic part (where $x \to \infty$) classically allowed, because $V(x, t > 0) < \epsilon$ holds. Consequently the barrier region where $V(x, t) > \epsilon$ is classically forbidden. Such a situation is the paradigmatic example for the tunneling effect to occur: due to the probabilistic nature of quantum mechanics the particles' probability to be present on the other side of the barrier *is not* zero although they do not have sufficient energy to *pass over the barrier*. This chapter (re-)considers the study presented in Ref. [1].

The tunneling effect lies at the very heart of quantum mechanics (QM), as there is no classical analogon to it and there is plenty of realizations of it in nature: α-decay, fusion and fission in nuclear physics, photoassociation and photodissociation in biology and chemistry [2–6] and many others more. The effect has been a matter of discussion since the advent of QM, see Refs. [7–9] and a theoretical overview in Ref. [10]. The physical analysis is usually made under the assumption

---

Electronic Supplementary Material Supplementary material is available in the online version of this chapter at http://dx.doi.org/10.1007/978-3-319-07085-8_6. Videos can also be accessed at http://www.springerimages.com/videos/978-3-319-07084-1.

A. U. J. Lode, *Tunneling Dynamics in Open Ultracold Bosonic Systems*,
Springer Theses, DOI: 10.1007/978-3-319-07085-8_6,

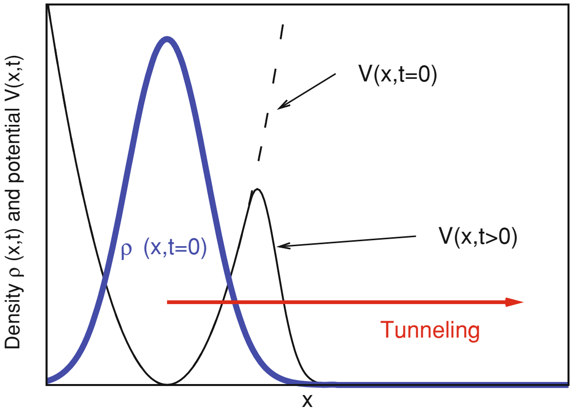

Fig. 6.1 Protocol of the Tunneling Process. An initial density $\rho(x, t < 0)$ (*blue line*) is prepared as the ground state of a parabolic trap $V(x, t < 0)$ (*dashed black line*). The trap is transformed to the open shape $V(x, t \geq 0)$ (*black line*), which allows the system to tunnel to open space. All quantities shown are dimensionless

that the correlation between decay products (i.e., between the remaining and emitted fractions of particles) can be neglected. However, it has to be stressed first that, at any finite decay time, the remaining *and* emitted particles still constitute *one* total many-body wave function and, therefore, can be correlated. Second, in contrast to the tunneling of an isolated single particle into open space, which has been amply studied and understood [10], nearly nothing is known about the tunneling of a many-body system. To shed light onto this process the initial state of an ultracold atomic gas of bosons is prepared coherently in a parabolic trapping potential [11] which is subsequently transformed to an open shape allowing for tunneling (see the Fig. 6.1). In this tunneling system the correlation between the remaining and emitted particles can be monitored by measuring deviations from the initial coherence of the wave function. This is because the final state is entirely in open space to the right of the barrier, where the bosons populate many many-body states, related to Lieb-Liniger states [12–14], which are generally not coherent. It is instructive to ask the following guiding questions for this chapter: what happens in between these two extremes of complete coherence and complete incoherence? And how does the correlation (coherence) between the emitted particles and the source evolve? Finding the answers to these questions will allow for a deeper theoretical understanding of many-body tunneling and explains whether the studied ultracold atomic clouds qualify as candidates for atomic lasers [15–20] or as a toolbox for the study of ionization or decay processes [2–5]. An instructive way to start investigating is to analyze the many-body dynamics for $N = 2$, $N = 4$, $N = 101$ weakly repulsive ($\lambda_0 = \frac{0.3}{N-1}$) bosons computed numerically exactly with the MCTDHB. The outline of the remainder of this chapter is first to investigate the one-body density $\rho(x, t)$, see Eq. (2.25), and integrals on it, $P^x_{not}(t)$, $P^k_{not}(t)$, derived from Eq. (2.28). Subsequently one finds the characteristic momenta involved in the process by investigating the one-body momentum density $\rho(k, t)$, see Eq. (2.25) and last one can learn on the coherence of the process by analyzing the natural occupations, see Eq. (2.26), and correlation functions, see Eq. (2.27).

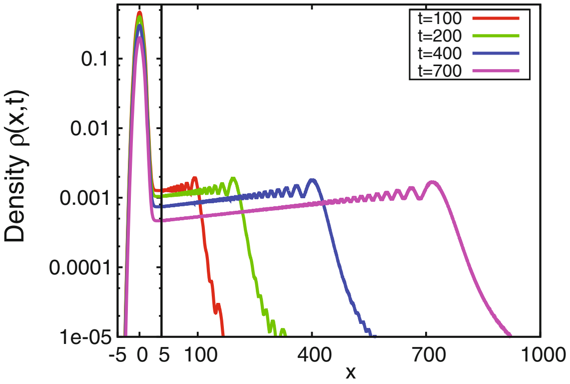

Fig. 6.2 Density of Many-Body Tunneling to Open Space for $N = 101$.* To represent the overall decay dynamics, the density $\rho(x, t)$ is plotted for various times t on logarithmic scale. The shape of the internal parts in the *left* inset is almost unchanged throughout the time evolution and the velocity of the *wavefront* is seemingly constant. See Video 4 for the time-evolution of the spatial and momentum densities in the depicted MCTDHB simulation. All quantities shown are dimensionless

6.1 One-Body Density and Integrals on It

To get an overall impression of the dynamics a plot of the time-evolution of the density of the decay by tunneling process is given in Fig. 6.2.

With time the source of bosons leaks to open space. During the process it preserves its shape, but its absolute value decays. The constant velocity of the wavefront propagating away from the well suggests that the underlying involved momenta are not time-dependent. Qualitatively the process is identical for the other particle numbers. To assess the nature of the decay and to study the correlation between the source and emitted bosons with the densities it's natural to decompose the one-dimensional space into the internal "IN" and external "OUT" regions with respect to the top of the barrier in Fig. 6.1. With this decomposition one is able to compute $P^x_{not,\rho}(t)$ which measures the probability to find a particle in the IN region:

$$P^x_{not,\rho}(t) = \int_{-\infty}^{C} \rho(x, t)dx, \tag{6.1}$$

where C is the position of the barrier [cf. Eq. (2.28)]. Its counterpart in momentum space, $P^k_{not,\rho}(t)$, corresponds to the fraction of the momentum distribution which is associated with a harmonic oscillator eigenstate:

$$P^k_{not,\rho}(t) = \int \rho^{Gauss}(k, t)dk, \tag{6.2}$$

where $\rho^{Gauss}(k, t)$ is obtained by least-squares fitting a Gaussian function $\rho^{Gauss}(k, t) = A(t)exp(-(B(t)x)^2)$ to the $k < 0$ portion of the momentum density $\rho(k, t)$. For a plot of these quantities for $N = 2$, $N = 101$, see Fig. 6.3.

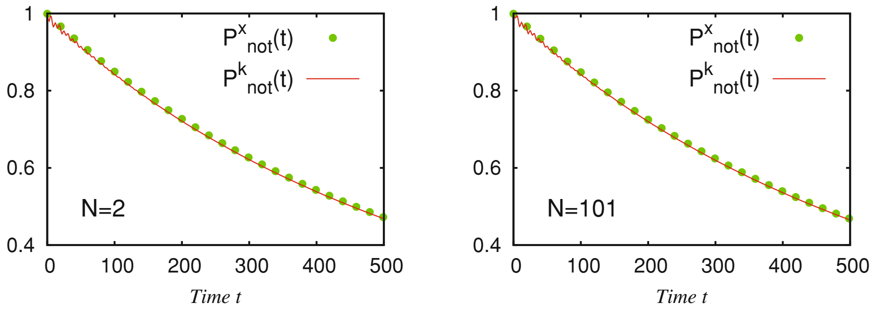

Fig. 6.3 Many-Body Tunneling to Open Space as a Fundamental Decay Process. To picture how the fraction of atoms remaining in the trap decays with time the density related nonescape probabilities $P^x_{not,\rho}(t)$ in real and $P^k_{not,\rho}(t)$ in momentum space are depicted, indicated by the respective *green dots* and *solid red* lines. All quantities shown are dimensionless

A first main observation is that the tunneling of bosonic systems to open space resembles an exponential decay process—a least squares fit shows slight differences, though: they can be attributed to the interaction. The close similarity of the $P^x_{not,\rho}(t)$, characterizing the amount of particles remaining in the internal region in real space, and $P^k_{not,\rho}(t)$ confirms the validity of the natural decomposition of Hilbert space into "IN" and "OUT", cf. Sect. 5.2.1. This means that it is of interest to analyze the *local properties* of the many-boson wave function in these sub-spaces (see also Appendix B). A good point to start from is the quantities from which the $P^k_{not,\rho}$ were extracted: the momentum distributions.

6.2 Momentum Distributions

The key features of the dynamics of quantum mechanical systems manifest themselves very often in characteristic momenta. Therefore, it is worthwhile to compute and compare evolutions of the momentum distributions $\rho(k, t)$ of the interacting bosonic systems. Figure 6.4 depicts $\rho(k, t)$ for $N = 2, 4, 101$ bosons. At $t = 0$ all the initial real space densities have Gaussian-shaped profiles resting in the internal region (see Fig. 6.1). Therefore, their distributions in momentum space are also Gaussian-shaped and centered around $k = 0$. With time, the bosons start to tunnel out of the trap. This manifests itself in the appearance of a pronounced peak structure on top of the Gaussian-shaped background, see central upper panel of Fig. 6.4. The peak structure is very narrow—similar to a laser or an ionization process, the bosons seem to be emitted with a very well defined momentum. For longer propagation times a larger fraction of bosons is emitted and more intensity is transferred to the peak structure from the Gaussian background. Thus, one can relate the growing peak structures in the momentum distributions to the emitted bosons and the Gaussian background to the bosons in the source. The value of the estimated momentum from

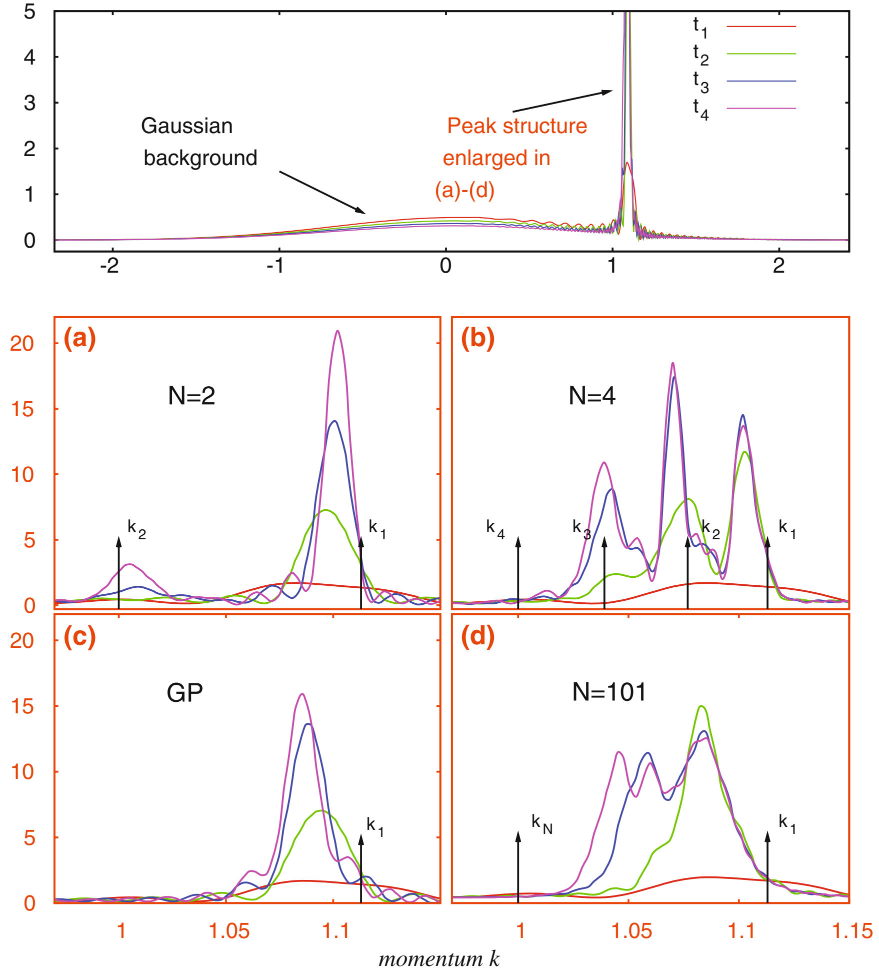

Fig. 6.4 The Peak Structures in the Momentum Distributions Characterize the Physics of Many-Body Tunneling to Open Space.* The total momentum distributions $\rho(k, t)$ for $N = 101$ (*top center*) and their peak structures for $N = 2$ (**a**), $N = 4$ (**b**), $N = 101$ (**d**), and the respective Gross–Pitaevskii solutions (**c**), at times $t_1 < t_2 < t_3 < t_4$. The broad *Gaussian-shaped* backgrounds correspond to the bosons remaining in the trap, the sharp peaks with positive momenta can be associated with the emitted bosons. For $N = 2$ one finds two peaks in panel (**a**), for $N = 4$ one finds three peaks and an emerging fourth peak at longer times, in panel (**b**). In panel (**d**) one finds three *washed out* peaks for $N = 101$. The corresponding GP dynamics reveal only a single peak for all times in (**c**). The arrows in the plots mark the momenta obtained from the model consideration, cf. Sect. 5.2.1. See Video 5 for the time-evolution of the momentum density and its decomposition into internal and external parts of the MCTDHB simulation in panel (**d**). All quantities shown are dimensionless

the model consideration, see Sect. 5.2.1, agrees excellently with the position of the peak in the computed exact momentum distributions, see the arrows marked k_1 in Fig. 6.4(a)–(d). This agreement allows us to interpret the peak structures in $\rho(k,t)$ as the momenta of the emitted bosons. As a striking feature, also other peaks with smaller k appear in these spectra at later tunneling times (see Fig. 6.4(a), (b) and (c)). These correspond to the momenta associated with the next chemical potentials μ_2, etc., see model in Chap. 5, Sect. 5.2.1. The momentum spectrum for $N = 101$ bosons shows a similar behavior—the multi-peak structures gradually develop with time starting from a single-peak to two-peaks and so on, see Fig. 6.4(d). The close proximity of the chemical potentials $\{\mu_i\}$ for a big particle number makes the peaks corresponding to the trapped subsystems of different particle numbers overlap. Still, the emission momenta are always enclosed by the first and the last chemical potentials, μ_1 and μ_N. However, from this figure one can see that the positions of the peaks' maxima, and with them the momenta of the emitted bosons change slightly with time. On the one hand one can see that the considered tunneling bosonic systems can not be utilized as an atomic laser: the initially coherent bosonic source emits particles with different, weakly time-dependent momenta. In optics a source behaving like the bosons momentum spectrums would be called polychromatic. On the other hand one can associate the peaks with different channels of an ionization process and their time-dependency with the channels' coupling. Thus, one can conclude that it is possible to model and investigate ionization processes with tunneling ultracold bosonic systems. To investigate the coherence of the tunneling process itself a comparison to the TDGP approximation is instructive. The above analysis of the momentum spectra relied on the exact numerical solutions of the TDSE for $N = 2, 4, 101$ bosons. In the context of ultracold atoms the Gross–Pitaevskii (GP) theory is a popular and widely used mean-field approximation describing systems under the assumption that they stay fully coherent for all times, cf. Sect. 5.1. The GP approximation assumes that the ultracold atomic cloud coherently emits the bosons to open space and keeps the source and emitted bosons coherent all the time. To learn about the coherence properties of the ongoing dynamics it is thus instructive to compare exact many-body solutions of the TDSE with the idealized GP results, see Fig. 6.4(c). The strengths of the inter-boson repulsion have deliberately been chosen such that the GP gives identical dynamics for all N studied. It is clearly seen that for short initial propagation times the dynamics is indeed coherent. The respective momentum spectra obtained at the many-body and GP levels are very similar, see Fig. 6.4(a)–(d) for $\rho(k, t_1 = 100)$. At longer propagation times ($t > t_1$), however, the spectra become considerably different. This means that with time, the process of emission of bosons becomes less coherent. To assess the mechanism of this loss of coherence, it is giving to analyze the natural occupations and the correlation functions of the process.

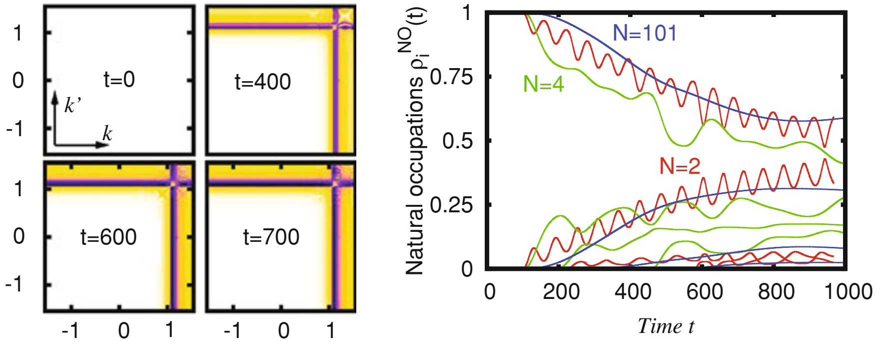

Fig. 6.5 Monitoring the Coherence of the System. *Left* The first order correlation functions in momentum space $|g^{(1)}(k'|k;t)|^2$ for $N = 101$ are plotted at $t = 0, 400, 600, 700$. At $t = 0$ the system is totally coherent, i.e., $|g^{(1)}|^2 = 1$. At times $t > 0$, the system remains coherent everywhere in k-space apart from the region around $k = 1$, where the peaks in the momentum distributions appear. The loss of coherence, $|g^{(1)}|^2 \approx 0$ only in these regions allows one to conclude that the source (*trapped*) bosons remain coherent at all times while the emitted ones are incoherent. *Right* The time evolution of the first few natural occupation numbers $\rho_i^{NO}(t)$ for $N = 2$, $N = 4$, and $N = 101$ bosons. The coherence in the systems is gradually lost with time. The systems fragment because more and more natural orbitals become populated. All quantities shown are dimensionless

6.3 Coherence from Natural Occupations and Correlation Functions

To quantify the coherence and correlations between the source and emitted bosons the momentum correlation functions $|g^{(1)}(k', k|t)|^2$ are computed and plotted in the left panel of Fig. 6.5 for $N = 101$ (for $N = 2, 4$ they look almost the same).

It has to be stressed here that the proper correlation properties cannot be accounted for by approximate methods. For example the GP solution of the problem gives $|g^{(1)}|^2 = 1$, i.e., full coherence for all times, cf. Chap. 5, Sect. 5.1 for a proof. For the exact solution one also obtains that at $t = 0$ the system is fully coherent, and thus $|g^{(1)}(k'|k; t = 0)|^2 = 1$. Hence, the top left panel of Fig. 6.5 is also a plot for the GP time-evolution. However, during the tunneling process the many-body evolution of the system becomes incoherent, i.e., $|g^{(1)}|^2 \to 0$. The coherence is lost *only* in the momentum-space domain where the momentum distributions are peaked, the k-region associated with the emitted bosons (see left panel of Fig. 6.5). In the remainder of k-space the wave function stays coherent for all times. The conclusion is that the trapped bosons within the source remain coherent. The emitted bosons become incoherent with their source *and* among each other. Therefore, the coherence between the source and the emitted bosons is lost. A complementary argumentation with the normalized real-space correlation functions is also possible and given below. The finding of a loss of coherence from the correlation functions among the emitted bosons and between the emitted bosons and the source is featured

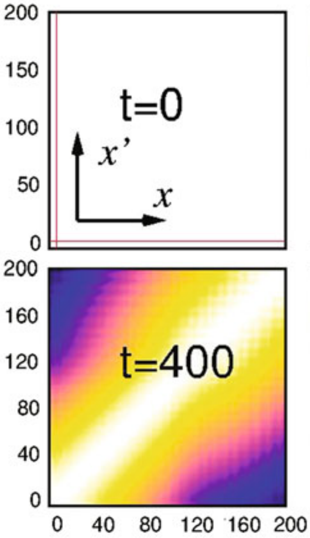

Fig. 6.6 The Real-Space Normalized Correlation Function of the Tunneling to Open Space Process. $|g^{(1)}(x_1'|x_1;t)|^2$ is used to measure the spatial coherence in the decaying system of N=101 bosons at various tunneling times. White corresponds to $|g^{(1)}|^2 = 1$ and black to $|g^{(1)}|^2 = 0$ The *red lines* in the *top left part* separate the "IN" and "OUT" regions. Here white corresponds to full coherence and black to complete incoherence. In the "OUT" region the spatial coherence is lost with time, i.e., $|g^{(1)}|^2 \approx 0$ on the off-diagonal $|g^{(1)}(x_1' \neq x_1|x_1;t)|^2$. The coherence of the source bosons is conserved, because in the "IN" part $|g^{(1)}|^2 = 1$ for all times. See text for discussion

also in the time-evolution of the occupation numbers $\rho_i^{(NO)}(t)$ (see Eq. (2.26) for their definition), as shown in the right panel of Fig. 6.5. This time-evolution for all particle numbers $N = 2$, $N = 4$, and $N = 101$ shows a similar overall behavior: Initially $\rho_1^{(NO)} \approx 1$ up to $t \approx 100$ signifies coherent dynamics. Subsequently, the system loses its coherence gradually until it becomes fully fragmented, eventually, several $\rho_i^{(NO)}$ are of a similar order of magnitude. To characterize the coherence of the tunneling many-boson system in real space one needs to compute the normalized real space first order correlation function $g^{(1)}(x_1'|x_1;t)$ at various times t. It is depicted for the system of $N = 101$ boson in Fig. 6.6.

From this figure one can see that initially the system is fully coherent, namely $|g^{(1)}(x_1'|x_1;t=0)|^2 = 1$. For $t > 0$ $|g^{(1)}(x_1'|x_1;t)|^2 < 1$ *only* in the "OUT" region, indicating that only the emitted bosons quickly lose their coherence. In contrast, the source bosons living in the interior around $x_1 = x_1' = 0$ remain coherent for all times. This corroborates the findings from the first order normalized momentum correlation function $g^{(1)}(k_1'|k_1;t)$ analyzed before: the bosons are ejected incoherently from a source, which preserves its initial coherence already for the weak inter-particle interactions $\lambda = 0.3$.

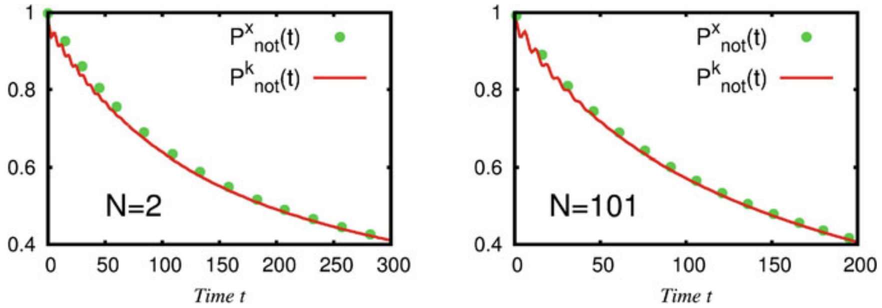

Fig. 6.7 Nonescape Probability for Sevenfold Stronger Interactions. To confirm that the fraction of atoms remaining in the trap decays exponentially with time, the density-related nonescape probabilities $P^x_{not,\rho}(t)$ in real and $P^k_{not,\rho}(t)$ in momentum space are depicted, indicated by the respective *green dots* and *solid red lines*. Even for stronger interactions the many-body tunneling to open space is a close to exponential decay process

6.4 Tunneling without a Threshold and Stronger Interactions

The previous section focused on the many-body tunneling process of an initially-coherent weakly interacting bosonic cloud. In this section, the generality of the found mechanism of many-body tunneling is shown by first analyzing what happens in the case of seven-times stronger interactions, $\lambda = 2.1$, when the initial state is still mostly condensed, but exhibits a larger depletion. The nonescape probabilities $P^{x/k}_{not}(t)$ for $N = 2, 101$ in are shown in Fig. 6.7.

The decay is faster than in the case of the weak $\lambda = 0.3$ interactions. The real space quantity P^x_{not} is also very close to the momentum space quantity P^k_{not}. To investigate the mechanism of the decay, the momentum distributions for $N = 2, 4, 101$ bosons and the respective TDGP calculation are plotted in Fig. 6.8 in the same way as in Fig. 6.4 of the previous section on weak interactions.

The model described in Sect. 5.2.1 predicts well the characteristic momenta of the dynamics also in the present case of seven-times stronger interactions, see the black arrows in Fig. 6.8. Of course, since the interaction is stronger, the positions of the peaks in the momentum distributions shift to higher values, compare Figs. 6.8 and 6.4. Even, when one turns to the case of two-hundred-times stronger interactions, where the initial state is fermionized, the model predicts well the occurring momenta in the momentum distributions as shown in Fig. 6.9 and the black arrows therein.

To conclude, this shows the generality of the found mechanism of many-body tunneling to open space as illustrated in Fig. 6.1 of the previous section on the weak interactions $\lambda = 0.3$.

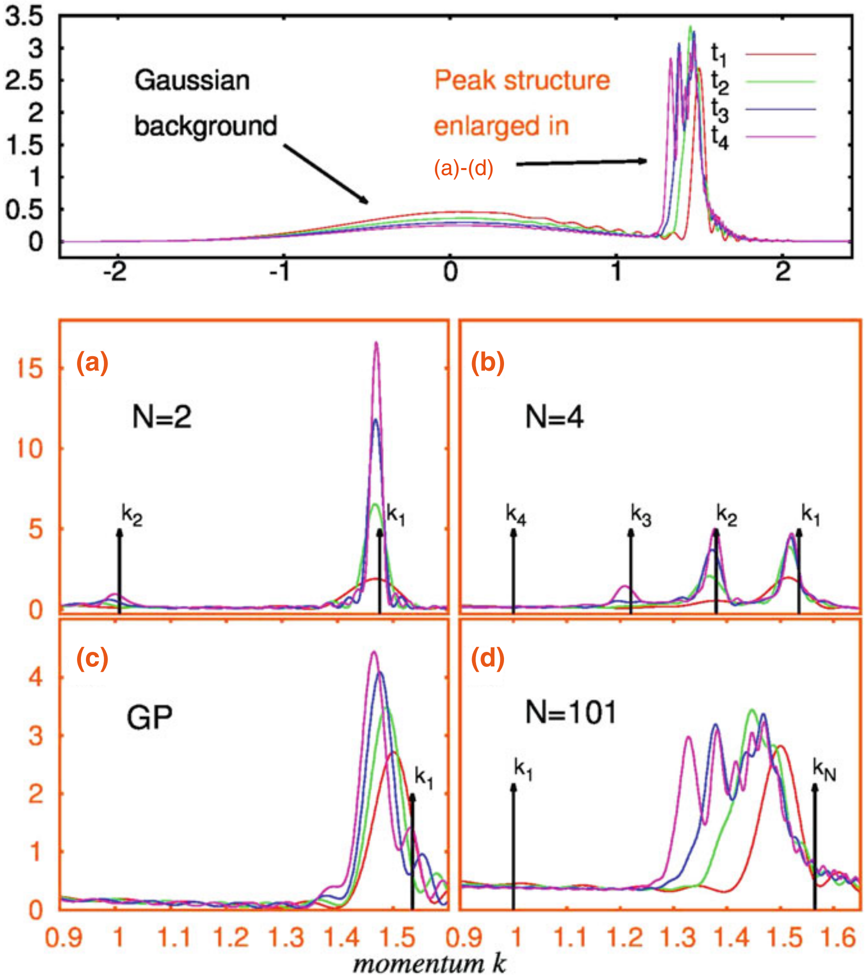

Fig. 6.8 Momentum Distributions for Sevenfold Stronger Interaction.* The total momentum distributions $\rho(k, t)$ for $N = 101$ (*top center*) and their peak structures for $N = 2$ (a), $N = 4$ (b), $N = 101$ (d), and the respective Gross–Pitaevskii solutions (c). The *arrows* in the plots mark the momenta obtained from the model consideration. Even for stronger interactions the peak structures in the momentum distributions characterize the physics of many-body tunneling to open space. See Video 6 for the time-evolution of the momentum density and momentum coherence for the MCTDHB simulation shown in panel (a)

6.5 Direct Detection of the Momentum Spectra

It remains to line out the possible straightforward experimental verification of the emerged physical picture. In typical experiments the bosons are ultracold many-electron atoms in a very-well defined electronic state. According to the conjectures

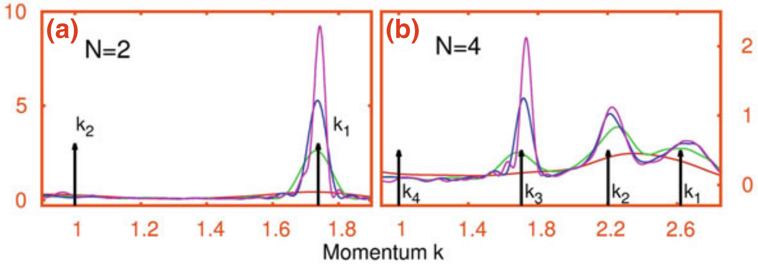

Fig. 6.9 The Peak Structures in the Momentum Distributions Characterize the Physics of Strongly-Interacting Bosons Tunneling to Open Space.* The total momentum distributions' peak structures for the $N = 2$ (a) and $N = 4$ (b) bosons with $\lambda = 60$ (the color code is as in Fig. 6.8). The *arrows* in the plots mark the momenta obtained from the model consideration. See Video 7 for the time-evolution of the momentum density and momentum coherence for the MCTDHB simulation shown in panel (b)

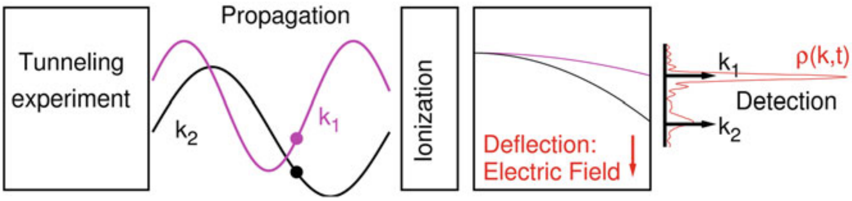

Fig. 6.10 Proposed Experimental Realization of the Momentum Spectroscopy of the Many-Boson System Tunneling to Open Space. At some propagation distance from the experiment (*left panel*) the bosons are ionized by, e.g., a laser beam. Subsequently, the ions/electrons are deflected by a static electric field and counted by a detector (*center right*). The momentum distribution can be obtained as histogram from different realizations of the few- or many-boson tunneling process by detection of the deflected particles (*right*)

put forward in Sect. 6.4 and Chap. 5, Sect. 5.2.2 above, the bosons will tunnel to open space with definite kinetic energy. To detect the kinetic energy of the emitted bosons one can utilize the techniques and principles of mass-spectrometry as schematically depicted in Fig. 6.10.

One can place an ionization chamber at some distance from the trapping potential to ionize the propagating bosonic atoms suddenly. The respective experimental ionization techniques are presently available, see e.g. Ref. [21] and references therein. The now charged particle will, by application of a static electric field, experience a corresponding driving force and change its trajectory. The trajectory of the ionized atom or, alternatively, the trajectory of the ionized electron are completely described by the respective driving force, the electronic state of the atom and its initial kinetic energy. By using a detector capable to detect the charged atom or a photoelectron multiplier for the electrons one can monitor the deflection of the ionized particle from the initial direction of propagation. The kinetic energy and, therefore, the momentum of the emitted boson can be calculated. By this one can detect *in situ* the momentum spectra $\rho(k, t)$ corresponding to different tunneling times and study the tunneling to open space as a function of time.

For the few-particle case it is especially interesting not only to obtain the momentum spectra, but also to monitor the time-ordering in which the peaks appear, i.e., to monitor the time evolution of the momentum peak densities $\rho(k, t)$. In such an experiment one can see whether the signals corresponding to the different k_i, $i = 1, \ldots, N$, will be detected sequentially, starting from the largest momentum, or they appear to some degree simultaneously. The latter case is a clear indication that the tunneling is a combination of several single particle tunneling processes happening *simultaneously*, as predicted in the previous section. Additionally, this measurement would be among the first direct observations of the dynamics of coherence and normalized correlations in ultracold bosonic systems.

To summarize, the deterministic preparation of few particle ultracold systems is now possible, see Ref. [22]. Mass-spectrometry is one of the most well-studied techniques and working tools available and even more sophisticated detection schemes have been developed on atom chips (see Ref. [23]). The combination of these facilities makes the detailed experimental time-resolved study of the tunneling mechanism feasible at present time.

6.6 Connection of the Numerical Experiment to Prior Model Considerations

Let us first compute the momenta available in the system of $N = 2$ bosons with interparticle interaction strength $\lambda_0 = 0.3$, following Ref. [24]. The difference between the total energies of the trapped system made of $N = 2$ and $N = 1$ bosons provides $k_1 = 1.106$. The second momentum associated with the emission of the last boson from the parabolic trap gives $k_2 = 1.000$. A similar analysis done for the system of $N = 4$ bosons with the interparticle interaction strength $\lambda_0 = 0.1$ $[\lambda_0(N-1) = 0.3]$ gives $k_1 = 1.106$, $k_2 = 1.075$, $k_3 = 1.038$ and $k_4 = 1.000$ for the first, second, third and fourth momentum, respectively. To relate the model and the full many-body results we draw the momenta estimated from the respective chemical potentials in Figs. 6.4, 6.8 and 6.9 by vertical arrows. The agreement between the momenta obtained from the model and the respective ones from the dynamics is very good, see the arrows and the peaks in the orange framed plots in Figs. 6.4(a) and (b). From this figure it is clearly seen that the later in time we look at the momentum distributions $\rho(k, t)$, the closer the peaks' maxima locate to the estimated results. Moreover, our model explains why for $N = 101$ the peaks are washed out. The chemical potentials of neighboring systems made of a big particle number (101 and 100, for instance) become very close and, as a result, the corresponding peaks start to overlap and become blurred. Nevertheless, they are always enclosed by the first and last chemical potentials contributing, see the labels k_1 and k_N in Fig. 6.4(d).

The good agreement between our model and full numerical experiments validates the applicability of the emerged physical picture to the tunneling to open space. We continue by excluding the possibility that the observed peaks in the momentum spectra can be associated with excitations inside the initial parabolic trap potential. This can be done straightforwardly by calculating the chemical potentials associated with the configurations where one or several bosons reside in the second, third, etc. excited orbitals of the trapped system. It is easy to demonstrate that the bosons emitted from these excited orbitals would have higher kinetic energies resulting in spectral features with higher momenta. Since the computed spectra depicted in Figs. 6.4, 6.8 and 6.9 do not reveal such spectral features we conclude that the excitations inside the initial parabolic trap potential do not contribute to the tunneling process in a visible manner.

The above analysis suggests that the overall many-body tunneling to open space process is assembled by the elementary mean-field-like tunneling processes analogous to the ionization of the systems made of different particle numbers which are happening *simultaneously*. We also are in the position to deduce now that every elementary contributing process is of a single-particle type. Indeed, if it were a two-particle process, the kinetic energy of the emitted bosons would have been $E_{2b}^{kin} = \frac{(k_1^{2b})^2+(k_2^{2b})^2}{2\cdot 2m}$. For large N one can assume that the chemical potentials of the first two processes are almost equal, i.e., $\mu_1^{2b} \approx \mu_2^{2b} \approx 2\mu_1$. The momentum associated with a two-particle tunneling process would be $k_{tot}^{2b} = \sqrt{4m\mu_1} = \sqrt{2}k_1$—which is far out of the domain where the peaks occur in the exact solutions.

In conclusion this chapter has shown how the many-body tunneling to open space process is built up by concurrently happening single-boson ejections. These emerge from sources with different particle numbers and convert the respective different chemical potentials to kinetic energies. Model predictions agree extremely well with the exact solution of the TDSE. The mechanism of fragmentation is explained by a loss of the coherence of the emitted bosons both among each other and with the source.

References

1. A.U.J. Lode, A.I. Streltsov, K. Sakmann, O.E. Alon, L.S. Cederbaum, How an interacting many-body system tunnels through a potential barrier to open space. Proc. Natl. Acad. Sci. USA **109**, 13521 (2012)
2. G. Gamow, Zur Quantentheorie Des Atomkernes. Z. F. Phys. **51**(3–4), 204–212 (1928)
3. B.S. Bhandari, Resonant tunneling and the bimodal symmetric fission of ^{258}Fm. Phys. Rev. Lett. **66**, 1034–1037 (1991)
4. N. Takigawa, A.B. Balantekin, Quantum tunneling in nuclear fusion. Rev. Mod. Phys. **70**, 77–100 (1998)
5. J. Keller, J. Weiner, Direct measurement of the potential-barrier height in the $B^1\Pi_u$ state of the sodium dimer. Phys. Rev. A **29**, 2943–2945 (1984)
6. M. Vatasescu et al., Multichannel tunneling in the $Cs_2 0_g^-$ photoassociation spectrum. Phys. Rev. A **61**, 044701 (2000)

7. R.W. Gurney, E.U. Condon, Quantum Mechanics and Radioactive Disintegration. Nature **122**, 439 (1928)
8. R.W. Gurney, E.U. Condon, Quantum Mechanics and Radioactive Disintegration. Phys. Rev. **33**, 127–140 (1929)
9. H.A. Kramers, Wellenmechanik und halbzählige Quantisierung. Zeitschr. F. Physik A **39** (10–11), 828–840 (1926)
10. M. Razavy, *Quantum Theory of Tunneling* (World Scientific Publishing Co., Singapore, 2003)
11. L.P. Pitaevskii, S. Stringari, *Bose–Einstein Condensation*. (Oxford University Press, Oxford, 2003)
12. E.H. Lieb, W. Liniger, Exact Analysis of an Interacting Bose Gas. I. The General Solution and the Ground State. Phys. Rev. **130**, 1605 (1963)
13. E.H. Lieb, Exact Analysis of an Interacting Bose Gas. II. The Excitation Spectrum. Phys. Rev. **130**, 1616 (1963)
14. M. Gaudin, Boundary Energy of a Bose Gas in One Dimension. Phys. Rev. A **4**, 386–394 (1971)
15. A. Öttl, S. Ritter, M. Köhl, T. Esslinger, Correlations and Counting Statistics of an Atom Laser. Phys. Rev. Lett. **95**, 090404 (2005)
16. I. Bloch, T.W. Hänsch, T. Esslinger, Atom Laser with a cw Output Coupler. Phys. Rev. Lett. **82**, 3008 (1999)
17. A. Del Campo, I. Lizuain, M. Pons, J.G. Muga, M. Moshinsky, Atom laser dynamics in a tight-waveguide. J. Phys. Conf. Ser. **99**, 012003 (2008)
18. M. Köhl, Th. Busch, K. Mølmer, T.W. Hänsch, T. Esslinger, Observing the profile of an atom laser beam. Phys. Rev. A **72**, 063618 (2005)
19. W. Ketterle, Nobel lecture: When atoms behave as waves: Bose–Einstein condensation and the atom laser. Rev. Mod. Phys. **74**, 1131–1151 (2002)
20. W. Ketterle and H.-J. Miesner, Coherence properties of Bose–Einstein condensates and atom lasers. Phys. Rev. A **56**, 3291 (1997)
21. T. Gericke, P. Würtz, D. Reitz, T. Langen, H. Ott, High-resolution scanning electron microscopy of an ultracold quantum gas. Nat. Phys. **4**, 949–953 (2008)
22. F. Serwane et al., Deterministic Preparation of a Tunable Few-Fermion System. Science **332**(6027), 336–338 (2011)
23. D. Heine et al., A single-atom detector integrated on an atom chip: fabrication, characterization and application. New J. Phys. **12**, 095005 (2010)
24. L.S. Cederbaum, A.I. Streltsov, Best mean-field for condensates. Phys. Lett. A **318**, 564–569 (2003)

Chapter 7
Tunneling of a Many-Boson System to Open Space with a Threshold

> *When we remember that we are all mad, the mysteries disappear and life stands explained.*
>
> Mark Twain

This chapter is dedicated to investigate how to control the tunneling process of the many-body system by introducing a threshold in the one-body potential of the Hamiltonian of the system. In the present case this is done by setting the potential to a constant value in the asymptotic region: The threshold T. The considerations presented in this chapter are related and extend [1]. The protocol for the process is unaltered: the ground state of an interacting system in a parabolic trap is prepared, then the potential is abruptly transformed to an open shape and finally the dynamics are analyzed from a many-body perspective and for different interaction strengths λ_0. To describe and assess the impact of the threshold on the occurring dynamics, it is appropriate to find a suitable smooth shape for the potential and then to analyze the energetics in this new potential. This can be achieved starting out from the conjectures presented in Chap. 6 and the model in Sect. 5.2.1. The viewpoint of available energies in the problem is subsequently used to control the final state as well as the correlation dynamics of the process with the threshold T and the interaction strength λ_0. Illustrative numerical examples are given and discussed. In the wider context of atom lasers [2–6] and ionization processes, the modification of the threshold T and the interaction strength λ_0 result in a modification of the ionization threshold, the characteristic velocity of the emission and the distance of the peaks in the momentum distribution. Hence, manipulating the threshold and the interaction, one is in the position to configure the dynamics of the ultracold atoms such that these dynamics simulate the desired ionization or atom laser process.

Electronic Supplementary Material Supplementary material is available in the online version of this chapter at http://dx.doi.org/10.1007/978-3-319-07085-8_7. Videos can also be accessed at http://www.springerimages.com/videos/978-3-319-07084-1.

A. U. J. Lode, *Tunneling Dynamics in Open Ultracold Bosonic Systems*,
Springer Theses, DOI: 10.1007/978-3-319-07085-8_7,

7.1 Setup

The setup of the system is very similar to the setup of the tunneling with zero threshold. The aim of this section is to give an outline of the changes with respect to the potential used for the tunneling dynamics with zero threshold in Chap. 6, Sect. 6.1.

The Potentials

In order to be flexible with the threshold T it is practical to use a smooth polynomial continuation of the harmonic trap $V_h(x) = \frac{1}{2}x^2$ from $x_{c1} = 2$ to $x_{c2} = 4$. There are four constraints to the polynomial continuation, namely: the polynomial and its first derivative have to be equal to the potential and its derivative at both connection points x_{c1} and x_{c2}. Therefore, a polynomial of at least third order with four coefficients, A, B, C, D, to satisfy the four constraints is required:

$$P(x) = Ax^3 + Bx^2 + Cx + D \tag{7.1}$$

With the constraints

$$P(x_{c1}) = Ax_{c1}^3 + Bx_{c1}^2 + Cx_{c1} + D = V_h(x_{c1}) = 2 \tag{7.2}$$

$$\frac{d}{dx}P(x)\mid_{x=x_{c1}} = 3Ax_{c1}^2 + 2Bx_{c1} + C = \frac{d}{dx}V_h(x)\mid_{x=x_{c1}} = 2 \tag{7.3}$$

for the connection at x_{c1} to the harmonic trapping potential $V_h(x)$ and

$$P(x_{c2}) = Ax_{c2}^3 + Bx_{c2}^2 + Cx_{c2} + D = T \tag{7.4}$$

$$\frac{d}{dx}P(x)\mid_{x=x_{c2}} = 3Ax_{c2}^2 + 2Bx_{c2} + C = \frac{d}{dx}T = 0 \tag{7.5}$$

for the connection to the constant threshold T at x_{c2}. From these four equations the coefficients $A(T)$, $B(T)$, $C(T)$, $D(T)$ are obtained. Hence, one can manipulate the threshold T arbitrarily while maintaining a smooth potential. The coefficients are collected in Table 7.1.

The overall potential then reads:

$$V(x) = \Theta(x_{c1} - x) \cdot \frac{1}{2}x^2 + \Theta(x - x_{c1}) \cdot \Theta(x_{c2} - x) \cdot P(x) + \Theta(x - x_{c2}) \cdot T \tag{7.6}$$

where $\Theta(\cdot)$ is the Heaviside step function. Plots of the potential with $T = 0.1, \ldots,$ 2.0 are depicted in Figure 7.1.

By using a polynomial continuation to the threshold, the position of the maximum of the potential (x_m) now depends on the threshold T as follows:

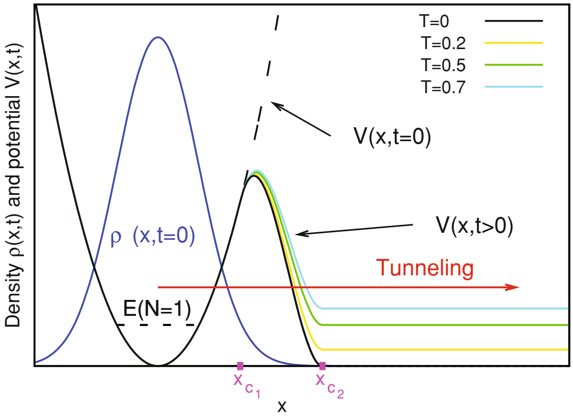

Fig. 7.1 Protocol for the Tunneling Dynamics with Non-Zero Threshold. The initial density (*blue line*) is prepared as the ground state of the parabolic trap (*black dashed* $V(x, t = 0)$). Subsequently, the potential is transformed to its open form with a threshold (various *solid colored lines*, $V(x, t > 0)$). This allows for a tunneling process to open space—inhibited by a threshold—to occur. The energy of a single, parabolically trapped particle, $E(N = 1)$, is indicated by the horizontal *black dashed line*. The initial potential, $V(x, t = 0)$, is the same as in the tunneling dynamics with zero threshold. Between x_{c_1} and x_{c_2} (indicated in magenta on the x-axis) the potential is the polynomial $P(x)$ of Eq. (7.1) with the coefficients as given in Table 7.1. Figure reprinted from Ref. [1]

Table 7.1 Parameters of the Potential with a Threshold

Coefficient	Dependency on T	Value at T = 0.5
A	$A(T) = -\frac{1}{4}T + 1$	0.875
B	$B(T) = \frac{9}{4}T - \frac{19}{2}$	8.375
C	$C(T) = -6T + 28$	25.0
D	$D(T) = 5T - 24$	21.5

$$x_m(T) = 2 + \frac{1}{3 - \frac{3}{4}T}. \tag{7.7}$$

Some quantities of interest now depend on the threshold, such as the nonescape probability

$$P_{not}(T, t) = \int_{-\infty}^{x_m(T)} \rho(x, t)dx, \tag{7.8}$$

because it should measure the remaining density up to the maximum of the barrier $x_m(T)$ defined in Eq. (7.7).

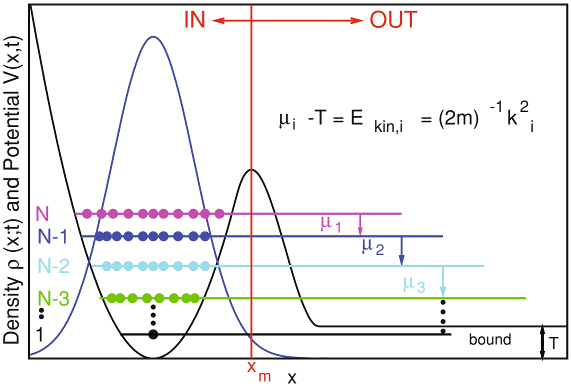

Fig. 7.2 Scheme to Model the Tunneling with a Threshold T by Concurrent Mean-Field Processes. The bosons are tunneling from the "IN" to the "OUT" subspace (indicated by the *red line*). If the threshold is large enough, some particles might become bound (see e.g. the $N = 1$ state indicated by the *lowest black line* in the above plot). The chemical potential μ_i is first used to overcome the threshold T and the remainder is transformed to the kinetic energy $E_{kin,i}$ if the state is not bound. The momenta corresponding to the chemical potentials $k_i = \sqrt{2m(E_{kin,i})} = \sqrt{2m(\mu_i - T)}; i = N, N-1, \ldots, 1$ appear in the momentum distribution, see the arrows in Fig. 7.5 and lines in Fig. 7.6. All quantities shown are dimensionless. Figure reprinted from Ref. [1]

7.2 Threshold Potentials and Their Dynamics from the Point of View of Energetics

Starting from the model consideration in Sect. 5.2.1 and its successful description of the tunneling dynamics of systems with zero threshold in Chap. 6, it is straightforward to adapt the model to the present potentials with a threshold. One can conveniently do that by going through the steps of the model consideration in Sect. 5.2.1 again, carefully taking into account the impact of the threshold onto the energetics—especially in the external part of the potential.

As a first step, it is natural to consider the system as split into an "IN" part, to the left of the maximum of the barrier at x_m, and an "OUT" part to the right of the maximum of the barrier at x_m. For a depiction, see Fig. 7.2. Consider the situation, when a single boson has escaped from the "IN" to the "OUT" region. According to the previous consideration in Sect. 5.2.1, the available energy of this boson must come from the energy difference of the trapped systems with N and with $N-1$ particles, $E^N - E^{N-1} = \mu_1$ — the chemical potential of the N-particle system. With this energy available, the ejected boson has to overcome the threshold T—hence, it remains with an energy $\mu_1 - T$ in the "OUT" part of the potential to the right of the barrier. As the potential in the "OUT" part is flat the ejected boson will convert its available energy to kinetic energy. Because the density can be assumed to be small, the effects of the interaction on the plane wave nature of the wave function can be neglected. Analogous to the model in Sect. 5.2.1, the other particles, hence, are ejected taking their available energy from the chemical potentials μ_i. One can derive momenta k_i from the related kinetic energies and the threshold:

$$E_{kin,i} = \mu_i - T = \frac{k_i^2}{2m} \quad \Rightarrow \quad k_i^T = \sqrt{2m(E_{kin,i})} = \sqrt{2m(\mu_i - T)}. \quad (7.9)$$

This assumes that the interaction in the exterior only forces the bosons to occupy different single-particle states and ignores the effect of the interaction on the shape of these states in the "OUT" part of space. It is further evident, that in the case of the absence of interaction, all chemical potentials are equal, i.e., $\mu_1 = \mu_2 = \cdots = \mu_N$.

A particularly interesting feature of the class of potentials with non-zero asymptotic value is that they can have bound states. If one raises the threshold T beyond the chemical potential μ_l of a certain parabolically trapped L-boson system then the boson to be ejected does not have enough energy to overcome T and stays trapped—hence, the system is in a bound state (cf. Fig. 7.2 and Eq. (7.9)). One can thus control the number of bound particles with the interaction λ_0 and the threshold T. By manipulating the interaction λ_0 the energies and particularly the chemical potentials can be controlled, and by adjusting the threshold T, the number of bound particles can be regulated. In the case of a vanishing interaction, the threshold T controls whether *the whole* system is bound or not. It is convenient to adopt the $|IN, OUT\rangle$ notation of the model in Sect. 5.2.1. The energy for the "IN" subsystem, E_{IN}, is given by the energy of N_{IN} interacting bosons in a parabolic potential, $E_{HO}(N_{IN})$. The minimal energy for the "OUT" system, E_{OUT}, is given by N_{OUT} bosons at rest, i.e., with momentum $k_j = 0$, at threshold potential energy, hence, $E_{OUT} = N_{OUT} \cdot T$. It follows for the total energy E_{TOT}:

$$E_{TOT}(N_{IN}, N_{OUT}, T, \lambda_0) = E_{HO}(N_{IN}) + N_{OUT} \cdot T. \quad (7.10)$$

To summarize, one can adjust the energies of the initial states, E_{IN} by tuning the interaction and the energies of the final states, E_{OUT}, by tuning the threshold T. The following subsections explore these possibilities for the tunneling bosonic systems with a threshold constituted by $N = 2$,$N = 3$, and $N = 101$ particles, respectively.

7.3 Controlling the Dynamics of Two Bosons by the Threshold

As a first step to explore the dynamics in the new potential with a threshold and the physics of the above model it is instructive to fix the interaction λ_0 and vary the potentials' threshold. Fig. 7.3 shows the energies of the possible final states with constant interaction and variable threshold, i.e., $E_{TOT}(N_{IN}, N_{OUT}, T, \lambda_0 = 1.0)|_{N_{IN}+N_{OUT}=2}$.

The respective lowest line in Fig. 7.3 shows the energetically favorable final state for the dynamics. Hence, the crossing points of the lines define critical thresholds at which the energetically favorable final state of the dynamics is changing. It would

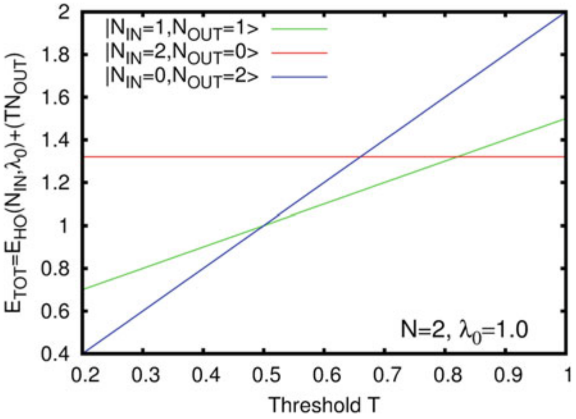

Fig. 7.3 Scheme for Controlling the Two-Boson Dynamics with the Threshold T. This plot shows the total energies $E_{TOT} = E_{HO}(N_{in}) + TN_{out}$ of the possible final states, $|2, 0\rangle$, $|1, 1\rangle$ and $|0, 2\rangle$ of two bosons at fixed interaction $\lambda_0 = 1.0$ and variable threshold T. At $T = 0.5$ a one-particle bound state emerges in the trap and at $T \approx 0.8$ the two-boson system becomes bound. The crossing points determine the (un)availability of final states. See text for further discussion. Figure reprinted from Ref. [1]

expected that for $T \leq 0.5$ both of the particles decay, and for $0.5 < T \lesssim 0.8$ one particle decays and the other stays bound. For $T \gtrsim 0.8$ the whole system is bound and no particle decays. This behavior is because the final states available are $|0, 2\rangle$, $|1, 1\rangle$ and $|2, 0\rangle$, respectively. The nonescape probability $P^x_{not}(t)$ should tend to 0 for the $|0, 2\rangle$ final state, to 0.5 for the $|1, 1\rangle$ final state and stay at 1 for the bound $|2, 0\rangle$ final state. To verify this behavior Fig. 7.4 shows a plot of the nonescape probabilities for the thresholds $T = 0.1$, 0.6 and 0.9.

One can see nicely that the expected behavior of the nonescape probability is recovered and that the prior analysis of the energetics of the problem is applicable. Furthermore, the above analysis demonstrates, how the threshold can be used to control the final state of the dynamics by modifying $E_{OUT} = N_{OUT} \cdot T$. By tuning $T \cdot N_{OUT}$ beyond the chemical potential of an N_{IN}-body system, an N_{IN}-body bound state is created. This allows for a flexible control of the counting statistics in the "IN"-subspace *and* the "OUT"-subspace. It remains to validate the predictions of the energetics model presented in Fig. 7.2 on the momenta of the ejected particles, see Eq. (7.9). For this validation it is good to inspect a plot of the peak structure in the momentum distribution of the tunneling processes occurring at equal times and varying different thresholds. See Fig. 7.5 for plots of $\rho(k, t, T)$ for $t = 600$ and $T = 0.1$ to $T = 0.6$.

The changes in the momentum distributions by the threshold are intuitive. The peak structure in the momentum distribution corresponds to the ejected bosons. If the threshold is increased, two effects upon the peaks are seen. First, by a larger threshold the peak is shifted towards 0, as the escaping bosons have to invest a larger part of their available energy to overcome the threshold (cf. Eq. (7.9)). Second, the

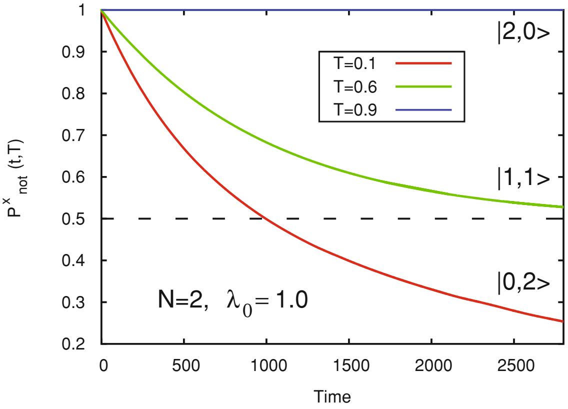

Fig. 7.4 Nonescape Probability for Varying Thresholds for $N = 2$ and $\lambda_0 = 1.0$. The nonescape probabilities $P^x_{not}(t, T)$ for different thresholds $T = 0.1, 0.6, 0.9$ are plotted as *red*, *green* and *blue line*, respectively. For $T = 0.1$ the final state $|0, 2\rangle$, for $T = 0.6$ the final state $|1, 1\rangle$ is favorable. For $T \gtrsim 0.8$, the two-boson system is bound, i.e., the only final state available is a bound state for $T = 0.9$. The thick horizontal *dashed line* marks $P^x_{not} = 0.5$, the nonescape probability of the final state $|1, 1\rangle$. See text for further discussion. Figure reprinted from Ref. [1]

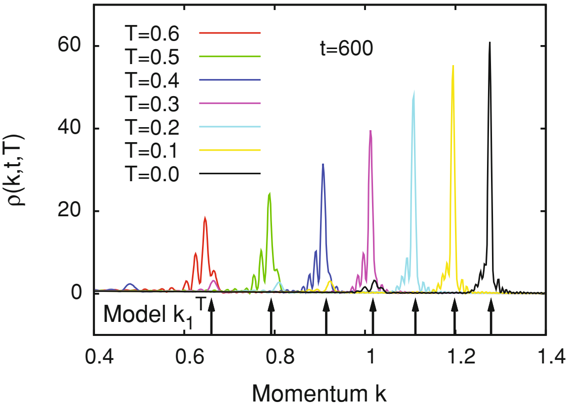

Fig. 7.5 Effects of Various Thresholds in the Momentum Distributions' Peak Structures.* This plot depicts $\rho(k, t = 600)$ for the tunneling processes in the potentials with thresholds $T = 0.0, 0.1, \ldots, 0.6$. *The arrows* at the *bottom* of the plot indicate the momenta k_1^T obtained from the model consideration. The momenta are shifted towards 0 by an increasing threshold T. The intensity, i.e. $\rho(k_1^T, t = 600)$, of the peaks is diminished by an increasing threshold. See Video 8 for the time-evolution of the momentum density for the depicted MCTDHB simulations. See text for further discussion. Figure reprinted from Ref. [1]

higher the threshold, the smaller is the intensity of the k_1^T peak, i.e. $\rho(k_1^T, t = 600)$. This means that the increase of the threshold decreases the rate with which the first boson is escaping.

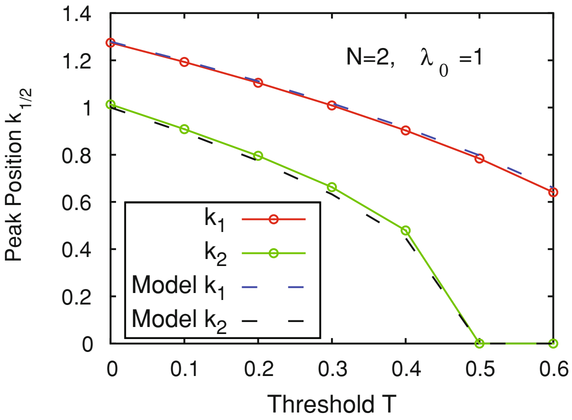

Fig. 7.6 Comparison of $N = 2$ Peak Positions to Model Predictions. The *solid red* and *green lines* with *circles* show the position of the peaks at k_1 and k_2 in the exact momentum distributions. The *blue* and *black dashed lines* show the model predictions k_1^T and k_2^T from Eq. (7.9). For the exact solutions *circles* represent actual data, the *lines* are drawn for guidance. See text for further discussion. Figure reprinted from Ref. [1]

As in the previous case of the tunneling to open space with 0 threshold, the agreement of the peaks' positions in k-space with the model's prediction is very good (see the arrows in Fig. 7.5). To further determine the validity of the model, especially also for the second peak at k_2^T, it is instructive to graph the change of the peak positions with varying threshold (see Fig. 7.6).

From the good agreement of the model predictions to the peaks of the exact solutions in Fig. 7.6, it can be deduced that the tunneling process of the many-boson system can indeed be pictured as an interference of different single-boson tunneling processes. These single-boson processes are happening simultaneously. Their momenta are determined by the chemical potentials of systems with different particle numbers. The momenta are shifted by the threshold. When the threshold is above the chemical potential of a certain process a bound state emerges and the momentum of this process becomes zero (see k_2, i.e., green line in Fig. 7.6 at $T \geq 0.5$). The emergence of a bound state in the system closes at least one of the final states. In the present case of $N = 2, \lambda_0 = 1$ the final state $|N_{IN}, N_{OUT}\rangle = |0, 2\rangle$ becomes energetically unfavorable for $T \geq 0.5$ and consequently the counting statistics of the final state are altered to $|N_{IN}, N_{OUT} = |1, 1\rangle$ (see Fig. 7.3) and the nonescape probability $P^x_{not}(t)$ of the decay converges to $N_{IN} = 1$ from above (see Fig. 7.4). Several different quantities can be controlled in the many-body tunneling dynamics to open space by modification of the threshold. First, the counting statistics can be controlled with the threshold by creating bound states. Second, this implies a control on the momentum spectra of the emitted bosons. Peaks can be *switched off (on)* by making the corresponding single-boson process energetically unaccessible (accessible).

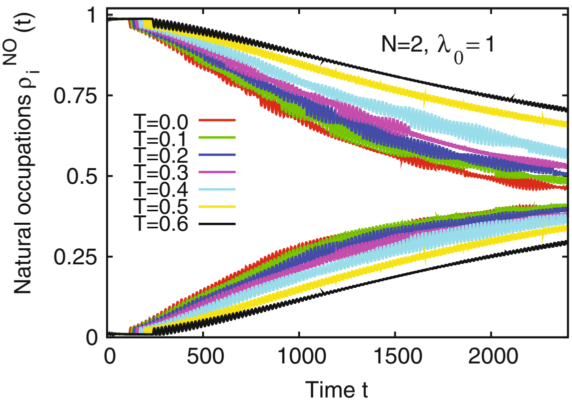

Fig. 7.7 Fragmentation is Delayed by Threshold. Shown is the time evolution of the first two occupations, $\rho_1^{(NO)}(t)$, $\rho_2^{(NO)}(t)$ for $N = 2$ bosons interacting with $\lambda_0 = 1.0$ for different thresholds T as various colored *solid lines*. The occurrence of fragmentation and the initial depletion are delayed by the increase of the threshold T. See text for further discussion. Figure reprinted from Ref. [1]

Effect of the Threshold on the Coherence and Correlation Dynamics

In Sect. 6 on the tunneling process of bosonic systems to open space without a threshold, the discussed dynamics of correlation and coherence were of key importance. The ejected bosons loose the coherence both with the source and among each other. As processes with a threshold are explained by a similar model, one would expect the correlation or coherence properties of the present process with a threshold to be similar to those properties of the process without a threshold. To prove this behavior, this section discusses the quantities describing the dynamics of coherence: the occupation numbers $\rho_i^{(NO)}(t)$ of the single-particle reduced density matrix and the one-particle and two-particle normalized correlation functions $g^{(1)}$ and $g^{(2)}$.

Time-Evolution of the Occupation Numbers

To find the effect of a change in the potentials threshold on the time-evolution of the occupation numbers, it is a good start to plot them for $N = 2, \lambda_0 = 1.0$ and thresholds $T = 0.0, 0.1, 0.2, \ldots, 0.6$ in Fig. 7.7.

The behavior of the occupation numbers upon increasing thresholds is as follows: as the process is slowed down by the threshold, the occurrence of fragmentation is delayed. Furthermore, the initial depletion of the system is delayed, i.e., $\rho_1^{(NO)} \approx 1$ holds for a longer initial time, when T is bigger. It is very interesting to note that the development of fragmentation persists also in the cases of $T \geq 0.5$, where a one-boson bound state emerges and the counting statistics of the final state are changing from $|0, 2\rangle$ to $|1, 1\rangle$. This is somewhat counterintuitive, because one would naively argue that the final state $|1, 1\rangle$ could be described with a single permanent (see Eq. (2.8)). Yet, the chosen $|N_{IN}, N_{OUT}\rangle$ notation refers to the counting statis-

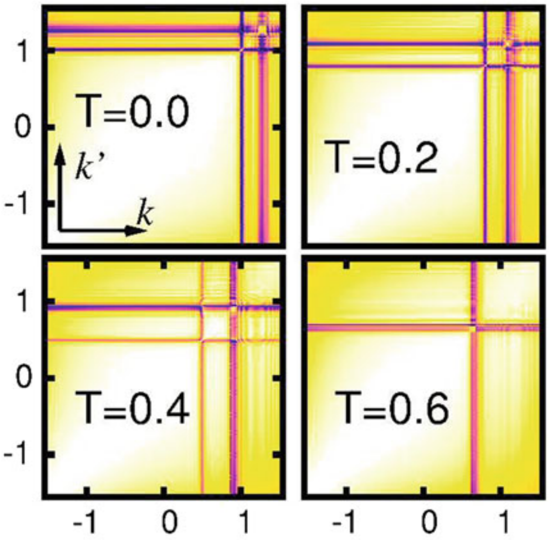

Fig. 7.8 Coherence in Tunneling to Open Space with a Threshold. Shown is the absolute value of the single-particle normalized correlation function, $|g^{(1)}(k', k; t)|^2$ for $t = 600$ for various thresholds T. White corresponds to full first-order coherence, i.e., $|g^{(1)}|^2 = 1$ and *black* to full first-order incoherence, i.e., $|g^{(1)}|^2 = 0$. Black, i.e., $|g^{(1)}|^2 \approx 0$ lines appear at the positions of the peaks in the momentum distribution (cf. Figs. 7.5 and 7.6). The ejected particles lose the coherence with the source. The change of the final state manifests in the absence of a *second line* where coherence is lost (cf. *bottom right plot* for $T = 0.6$). See text for further discussion. *Top left*, *bottom left* and *bottom right Panel* of Figure reprinted from Ref. [1]

tics and not to permanents or eigenfunctions of a many-body Hamiltonian. Hence, fragmentation is occurring anyways because one needs possibly many permanents to represent the final $|N_{IN} = 1, N_{OUT} = 1\rangle$ state.

Effects of Threshold on the Coherence and Correlation Dynamics

To explore, whether there is an effect of the threshold on the correlation dynamics during the fragmentation in the tunneling to open space, the normalized single-particle correlation function $g^{(1)}$ has to be inspected. See Fig. 7.8 for a plot of $g^{(1)}$ in momentum space.

In the correlation functions in Fig. 7.8 the single-particle processes, from which the many-boson tunneling process is built up, are seen as lines of incoherence. The positions of these lines coincide with the momenta k_1, k_2 predicted by the model considerations in Sect.7.2. During the time-evolution, the positions of the lines and hence the structure of $g^{(1)}$ does not change and it is therefore sufficient to depict $g^{(1)}$ at a single point in time. With the increase of the threshold the system's final state is changed from $|0, 2\rangle$ to $|1, 1\rangle$, i.e., only one of the two particles is decaying for $T \geq 0.5$. This change manifests itself in the correlation functions by the disappearance of the line at k_2 corresponding to the now energetically forbidden

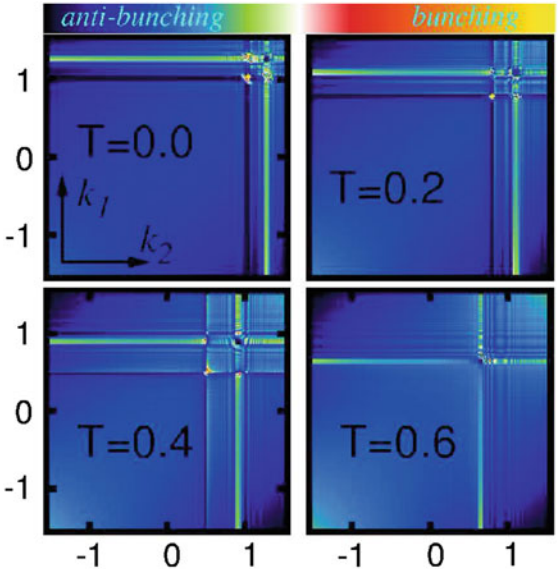

Fig. 7.9 Bunching and Anti-Bunching in Tunneling to Open Space with a Threshold. Shown is the value of the diagonal of the two-particle normalized correlation function, $g^{(2)}(k_1, k_2; t)$ for $t = 600$ for various thresholds T. The cases of $T = 0.0$ and $T = 0.2$ show anti-bunching for the k-space region with the first peak in the momentum distributions and anti-bunching for the region of the second peak. Increasing the threshold gradually switches off the second peak and leaves behind a slightly anti-bunched single line. Throughout the time-evolution (not shown) the peaks on the diagonal at $k_1 = k_2 = k_1^T$ and $k_1 = k_2 = k_2^T$ attain maximal bunching. See text for further discussion

process (cf. e.g. bottom left and bottom right part of Fig. 7.8). By the increase of the threshold the loss of coherence around the momentum k_2 is gradually decreasing until it becomes fully coherent for the $T = 0.6$ case, eventually. In this manner, peak after peak, corresponding to the model processes, is becoming fully coherent, as soon as the corresponding final state is energetically unfavorable. It is interesting that the coherence of the system is still lost in the cases where only a single particle is ejected (statistically). Hence, the two-body correlations in the tunneling process should be considered. The two-body correlations should show changes of the many-boson process, when the system is switched from two-boson to one-boson decay. In the spirit of Hanbury Brown and Twiss, Refs. [7–9], the situation where $g^{(2)} > 1$ is referred to as bunching and $g^{(2)} < 1$ is referred to as anti-bunching. For a plot of $g^{(2)}$ in momentum space for $t = 800$, see Fig. 7.9.

The structure of the diagonal of the two-particle normalized momentum correlation function, $g^{(2)}(k_1, k_2)$ is intricate: it has a line-structure similar to $g^{(1)}$ in Fig. 7.8. Yet, in the case of $g^{(2)}$ coherence can be lost in two ways—through bunching, i.e. $g^{(2)} > 1$, or anti-bunching, i.e. $g^{(2)} < 1$. In the case of bunching, the two momenta are likely to occur together whereas in the case of anti-bunching they are not. From the general structure of Fig. 7.9 it can be observed that the resting part of the cloud, i.e., where $k_1 = k_2 \approx 0$, is initially and throughout the tunneling process a slightly anti-bunched, almost second order coherent entity, because $g^{(2)} \lesssim 1$ holds for $k_1 = k_2 \approx 0$ at all different thresholds T. The lines are located at k_1^T and k_2^T where the peaks in the momentum distribution are. The first line at the bigger k_1^T shows bunching whereas the second line at the smaller k_2^T shows anti-bunching. This means that it is likely to find one boson at rest and one with k_1^T, while it is rather likely that the second boson also propagates when one finds the first one at k_2^T. The change in the final state of the tunneling process is again visible by the disappearance of the line around k_2^T (cf. bottom right part of Fig. 7.9). The diagonal point at $k_1^T = k_1 = k_2$ is strictly anti-bunched in this case. The line structure is less bunched. This behavior is expected because only one boson can leave and, hence, it is becoming more and more likely to have a boson at rest and another one propagating with k_1^T. In those cases where both bosons are decaying, the degree of sequentiality can be assessed with $g^{(2)}$: when one analyzes the line around k_2^T in the plots of $g^{(2)}$ for $T = 0.0, 0.2$ and 0.4 bunching occurs only at the intersections with the other lines and this means that it is very likely that one boson has already left the trap and propagates with momentum k_1^T when the second one follows with momentum k_2^T.

In the cases of two-particle decay, the intensities of the peaks at the intersection points of the lines are time-dependent. The ratio of the intensities of the peaks/holes at $k_1 = k_2 = k_1^T$ and $k_1 = k_2 = k_2^T$ on the diagonal to the intensities of the peaks/holes on the off-diagonal at $k_1 = k_1^T; k_2 = k_2^T$ and $k_1 = k_2^T; k_2 = k_1^T$ and the dynamics show the interference of the simultaneously happening single particle emission processes in the model consideration from Sect. 7.2. The interference causes the final state of the dynamics to contains two bosons neither of which is propagating with a specific momentum, but rather both bosons are simultaneously propagating with the momenta k_1^T and k_2^T to a certain degree.

To summarize, the dynamics of the tunneling process to open space can be controlled by the threshold T. The occurrence of bound states manifests itself by closing final states of the dynamics. The energies available in the decay process are obtained from the chemical potentials of systems with reduced particle number. These energies are first used to overcome the threshold and subsequently converted to characteristic momenta. The coherence of the ejected particles with the source is lost and the bunching and anti-bunching properties explain to which degree the processes occur (non-)sequentially and show the dynamics of the interference of the single-particle emission processes.

7.4 Controlling the Dynamics of Three Bosons by the Interactions

The aim of this section is to underline and corroborate the generality of the findings of the previous section for larger particle numbers. The control mechanism employed

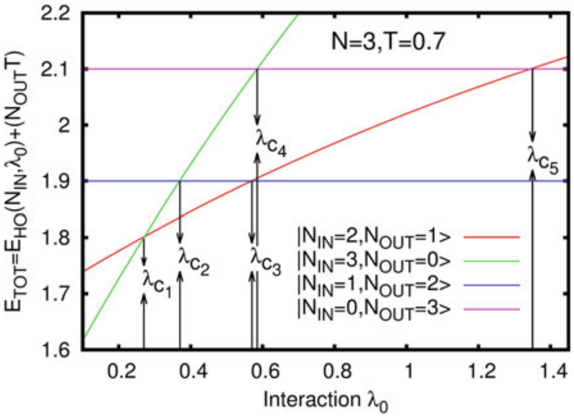

Fig. 7.10 Energetics of the $N = 3$ System with a Threshold of $T = 0.7$. This plot shows the minimal energies $E_{TOT}(N_{IN}, N_{OUT}, T, \lambda_0)$ which are needed to allow the different final states $|N_{IN}, N_{OUT}\rangle = |3, 0\rangle$; $|2, 1\rangle$, $|1, 2\rangle$, and $|0, 3\rangle$, as *solid green*, *red*, *blue*, and *magenta line*, respectively. The crossing points at λ_{c_k} show for which interactions final states are available. See text for discussion. Figure reprinted from Ref. [1]

for the final states is generalized: instead of the interaction strength λ_0 the threshold T is kept at a fixed value, $T = 0.7$. By changing λ_0 it is possible to determine which final states are favorable in the dynamics. A plot of $E_{TOT}(N_{IN}, N_{OUT}, T = 0.7, \lambda_0)$ for $N = N_{IN} + N_{OUT} = 3$ particles is given in Fig. 7.10.

Here, only the energies of $|3, 0\rangle$, and $|2, 1\rangle$, i.e., $E_{TOT}(N_{IN} = 3, N_{OUT} = 0, T = 0.7, \lambda_0)$, and $E_{TOT}(N_{IN} = 2, N_{OUT} = 1, T = 0.7, \lambda_0)$, are dependent on the strength of the interaction, λ_0. The energies of both $|1, 2\rangle$, and $|0, 3\rangle$, on the other hand, are independent of λ_0 in the considered model. The reason is that the energy of a single boson does not depend on the interaction ($E_{HO}(1) = 0.5$) and the interaction in the exterior is neglected in the model. The energy of $|1, 2\rangle$ is $E_{TOT} = (1, 2, 0.7, \lambda_0) = 0.5 + 2 \cdot T = 0.5 + 1.4 = 1.9$ and the energy of $|0, 3\rangle$ is $E_{TOT}(0, 3, 0.7, \lambda_0) = E_{HO}(N_{IN} = 0) + 3 \cdot T = 3 \cdot 0.7 = 2.1$. These are the minimal energies the system would need in order to eject two or three particles, respectively. The energy of the final state, in which a single particle has tunneled, $E_{TOT}(2, 1, 0.7, \lambda_0) = E_{HO}(N_{IN} = 2) + 1 \cdot T = 0.7 + E_{HO}(N_{IN} = 2)$, is dependent on the interaction, because the energy of the trapped system, $E_{HO}(N_{IN} = 2)$, with two bosons depends on interaction and so does the energy of the trapped system $|3, 0\rangle$ for the analogous reason.

If an interaction λ_0 smaller than λ_{c_1} is chosen for the initial state of $N = 3$ parabolically trapped particles, the system becomes bound at a threshold of $T = 0.7$ because all the possible final states, $|2, 1\rangle$, $|1, 2\rangle$, and $|0, 3\rangle$ are energetically not available. If one chooses an interaction of $\lambda_{c_1} \leq \lambda_0 \leq \lambda_{c_2}$, then the final state $|2, 1\rangle$ is energetically allowed, i.e., $E_{HO}(3) > E_{TOT}(2, 1, 0.7, \lambda_0)$, but the other final states are energetically forbidden. In this regime, the $N = 3$ system should thus decay by emitting a single boson, leaving behind two bound bosons. In the case of e.g. $\lambda_{c_3} > \lambda_0 > \lambda_{c_2}$, two final states, i.e., $|2, 1\rangle$, and $|1, 2\rangle$, are energetically allowed, because $E_{HO}(3) > E_{TOT}(1, 2, 0.7, \lambda_0) > E_{TOT}(2, 1, 0.7, \lambda_0)$. In this situation, it turns out that the energetically lowest configuration is the actual final state. This means that e.g. in the above case of $\lambda_{c_3} > \lambda_0 > \lambda_{c_2}$ one finds the final state of the dynamics to be $|2, 1\rangle$, i.e., the ejection of a single particle is preferred. This can be illustrated by the physics of decay processes: the rate at which a decay process is occurring is determined by the overlap of the initial and the final states. Intuitively, the overlap of the $|N_{IN} = 3, N_{OUT} = 0\rangle$ and $|N_{IN} = 2, N_{OUT} = 1\rangle$ states is larger than that of the $|N_{IN} = 3, N_{OUT} = 0\rangle$ and $|N_{IN} = 1, N_{OUT} = 2\rangle$ states. This is simply due to their contributions in the IN subspace. Furthermore, there is also an overlap of the $|N_{IN} = 1, N_{OUT} = 2\rangle$ and the $|N_{IN} = 2, N_{OUT} = 1\rangle$ states. This means that there is a rate with which $|N_{IN} = 1, N_{OUT} = 2\rangle$ is transformed to $|N_{IN} = 2, N_{OUT} = 1\rangle$. With this reasoning the final state is, hence, the energetically lowest final configuration. One can apply a similar reasoning for the other critical interactions $\lambda_{c_4}, \lambda_{c_5}$. It is interesting to note the peculiarity of the process—determined by the overlap of $|N_{IN} = 1, N_{OUT} = 2\rangle$ and $|N_{IN} = 2, N_{OUT} = 1\rangle$: the trapped particle number N_{IN} is actually increasing by one. With this reasoning it should thus be possible to find sets of parameters for which the nonescape probability of the system increases for a limited amount of time. This is at times at which the predominant part of the wave function is similar to e.g. $|N_{IN} = 1, N_{OUT} = 2\rangle$. However, in all the presented examples in this section this was not the case. This makes the following conclusion tempting: the rate at which the above-mentioned transformation of $|N_{IN} = 1, N_{OUT} = 2\rangle$ to $|N_{IN} = 2, N_{OUT} = 1\rangle$ is very large and this makes the observation of the counterintuitive behavior of the nonescape probability impossible. Any population in $|N_{IN} = 1, N_{OUT} = 2\rangle$ is momentarily shifted to $|N_{IN} = 2, N_{OUT} = 1\rangle$ and the respective counting statistics cannot be found.

In order to consistently investigate such populations so-called loss operators are needed (see Appendix A). With these loss operators the time-evolution of the population of any final state is, in principle, accessible. In the current implementation of the MCTDHB [10], these loss operators are not available. To check the validity of the above considerations, it remains to quantify the counting statistics in the dynamics with the nonescape probabilities $P^x_{not}(t)$, cf. Chap. 6, Sect. 6.1.

7.4.1 Nonescape Probabilities

To verify the above considerations, it is timely to first analyze the time-evolution of the nonescape probabilities, $P^x_{not}(t)$ in the given example of $N = 3$ bosons in a potential with $T = 0.7$ for various interactions λ_0. For a plot of all nonescape probabilities, corresponding to the different possible final states, see Fig. 7.11.

The behavior of the nonescape probabilities also for $N = 3$ is as predicted from the energetics: when a certain final state becomes energetically unavailable, then the counting statistics of the final state change. For example, for $\lambda_0 = 0.5$, the available

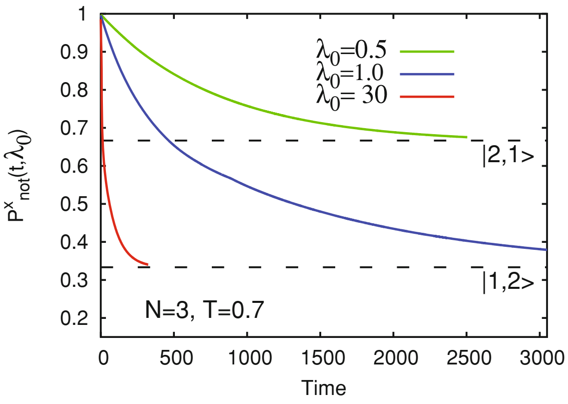

Fig. 7.11 Time-Evolution of Nonescape Probabilities for Different Final States for $N = 3$ Bosons. The dependence on the interaction λ_0 of the nonescape probability for $N = 3$ bosons tunneling to open space in a potential with a threshold of $T = 0.7$ is shown. The interactions and the threshold were chosen according to energetics (cf. Fig. 7.10) of the process such that there is a bound state for either $N = 1$ (*red* and *blue solid lines*) or $N = 2$ (*green solid line*) bosons. See text for further discussion

final state in the $|IN, OUT\rangle$ notation is $|2, 1\rangle$—consequently, the norm of the density in the "IN" subspace, i.e., the nonescape probability P_{not}, converges to $\frac{2}{3}$. In the case of the stronger interaction $\lambda_0 = 1.0$, the final state $|1, 2\rangle$ is energetically favorable and consequently the nonescape probability converges to $\frac{1}{3}$. The model introduced in Sect. 7.2 is indeed accurate in predicting the counting statistics of the tunneling to open space process with a threshold also for the control of the process with the interaction for $N = 3$ bosons.

It remains to analyze the many-body physics of coherence and correlations also for the $N > 2$ cases.

7.4.2 Coherence and Correlations in the Tunneling Process with a Threshold for N = 3

In order to determine the effects in the processes' correlation and coherence dynamics, it is convenient to investigate the correlation functions $g^{(1)}$ and $g^{(2)}$ in momentum space. Fig. 7.12 shows the coherence $|g^{(1)}(k_1, k_1', t = 800)|^2$ for different interactions and a fixed threshold $T = 0.7$ in the left and center panel. For convenience and in order to display all possible final states of the dynamics with an $|N_{IN} = 3, N_{OUT=0}\rangle$ initial state, the right panel of Fig. 7.12 shows the coherence in the $T = 0$ dynamics.

Indeed, the behavior of the case of $N = 2$ bosons is reproduced in the dynamics of the coherence in the tunneling to open space process of $N = 3$ bosons. Upon increase of the interaction λ_0 across the critical value for the availability of a certain final state,

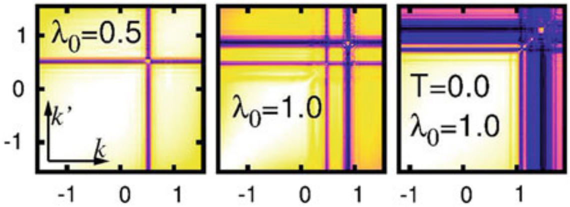

Fig. 7.12 Coherence Dynamics in Tunneling to Open Space with a Threshold for $N = 3$ Bosons.* The first order correlation function $|g^{(1)}|^2$ is plotted for three different final states with $N_{IN} = 2$, 1, and $N_{IN} = 0$ in the *left*, *middle* and *right Panel*, respectively, for the time $t = 800$. *White* corresponds to $|g^{(1)}|^2 = 1$ and *Black* to $|g^{(1)}|^2 = 0$. The *left Panel* for the interaction $\lambda_0 = 0.5$ and threshold $T = 0.7$ shows a single line at the momentum with which the single boson escapes. In the *middle Panel* for $\lambda_0 = 1.0$ and $T = 1.0$ two bosons are emitted and the wave function looses it's coherence at precisely their respective momenta. For convenience, the *right Panel* shows the case of $\lambda_0 = 1.0$ and $T = 0.7$ where all $N = 3$ bosons can decay—and consequently 3 *lines show up* where $|g^{(1)}|^2 \approx 0$. See Video 9 for the time-evolution of the momentum coherence for the MCTDHB simulation shown in the *left* and *middle* panels. See text for further discussion. *Left* and *middle Panel* of Figure reprinted from Ref. [1]

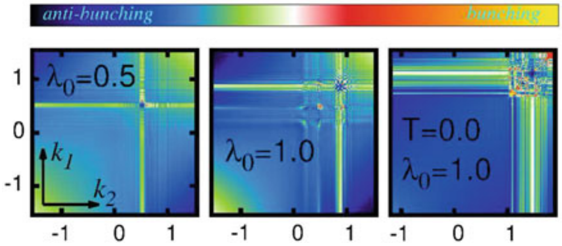

Fig. 7.13 Bunching Dynamics of Tunneling to Open Space with a Threshold for $N = 3$ Bosons.* The second order correlation function $g^{(2)}$ is plotted for three different final states with $N_{IN} = 2$, 1, and $N_{IN} = 0$ in the *left, middle and right Panel*, respectively for the time $t = 800$. The line structure of the first order correlation functions in Fig. 7.12 is preserved. The lines corresponding to the biggest momenta show slight anti-bunching. In their intersection the anti-bunching is intense. Where the lines corresponding to the bigger k intersect the lines of the smaller momenta and also on the diagonal, bunching occurs—the time-dependence of this (anti-)bunching pattern shows the dynamics of the interference of the concurrent ejection of two bosons. See Video 10 for the time-evolution of the momentum bunching and anti-bunching for the MCTDHB simulation shown in the left and middle panels. See text for further discussion

new lines, which are incoherent, show up (cf. left and middle panel of Fig. 7.12). Hence, with the momentum distributions, also the first order coherence in the process can be controlled by the manipulation of λ_0. Of course, the dynamics shown involve the fragmentation of the initially coherent sample of $N = 3$ parabolically trapped bosons. Both, the time evolution of the occupation numbers and the momentum distributions resemble in this case those in Figs. 7.7, and 7.5 and are not shown, therefore. It remains to find out what are the two-body properties of the process. For this purpose, a plot of the second order coherence $g^{(2)}$ is shown in Fig. 7.13.

The structure of the first order coherence $|g^{(1)}|^2$ in Fig. 7.12 is preserved for the diagonal part of $g^{(2)}$ in Fig. 7.13. The anticipated behavior from the case of $N = 2$ bosons (cf. Fig. 7.9) prevails: the (anti-)bunching intensities on the intersections of the lines corresponding to different ejection momenta shows the dynamics of the interference of the single-boson emission processes. The degree of the (anti-)bunching on the diagonal and the (off-)diagonal measures the sequentiality and interference of the processes. Interestingly, the line corresponding to the largest momentum is all cases the closest to uncorrelated (i.e., white in Fig. 7.13) and the anti-bunching for this line on the diagonal is the strongest. Hence, the boson emitted and propagating at the corresponding momentum k_1^T is very unlikely to be found, if another boson also propagates with the same momentum. Furthermore, the boson propagating with k_1^T is uncorrelated with all the other momenta—one could say it does not care at all about the remainder of the N-boson system. This explains the good applicability of the model introduced in Sect. 7.2. While the escaped bosons loose their first order coherence with the source entirely, their second order coherence is closer to being preserved. This is because a given process, accounting for a single line, is of a single particle. The model's elementary processes describe exactly such a behavior. Analogous reasoning can be applied to the other lines in $g^{(2)}$. This concludes the discussion of the first- and second-order coherence in the many-boson process of tunneling to open space. To assess the found conjectures and the generality of the discussed model considerations, the following section explores the tunneling process with a threshold for stronger interactions and large particle numbers.

7.5 Validation of the Control Scheme for Stronger Interactions and Larger Particle Numbers

To corroborate the findings of Sects. 7.3, 7.4 and to prove the generality of the model considerations in Sect. 7.2 also for stronger interactions, in Fig. 7.11 also a plot of the nonescape probability for the very strong interaction $\lambda_0 = 30.0$ is shown by a red solid line. For such a strong interaction the initial state is fermionized. It would be expected that the model's description is inaccurate if it was dependent on the interparticle interactions. Yet, the model prediction of a nonescape probability $P^x_{not,\rho}$ of $\frac{N_{IN}}{N} = \frac{1}{3}$ and the final state $|1, 2\rangle$ still holds. Intuitively, the decay happens at a much faster rate in this stronger interacting case. The conclusion that the model consideration should hold for particle numbers $N > 3$, independent of the interactions is tempting. In order to prove the general applicability of the model, Fig. 7.14, shows the energetics and nonescape probability for $N = 101$ particles. In this case, the threshold was fixed at $T = 0.6$ and the tunneling process' counting statistics were tuned by modifying the interactions in order to obtain an $N_{IN} \approx 50$ bound state by the energetics described in the model in Sect. 7.2.

Fig. 7.14 shows the validity of the model for a general number of particles: The nonescape probability of the many-body process converges to $\frac{N_{IN}}{N} = \frac{1}{2}$ (see right

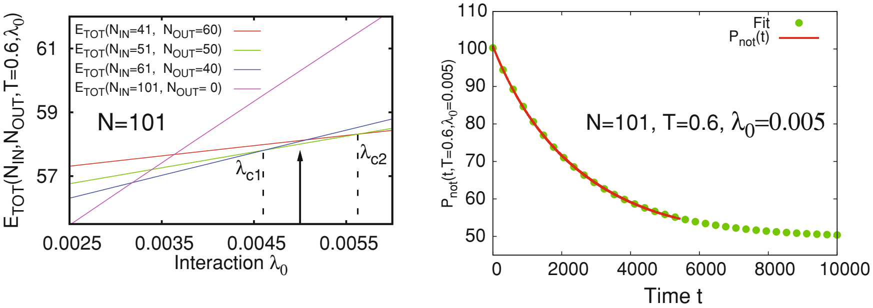

Fig. 7.14 Energetics and Nonescape Probability for the Tunneling to Open Space of $N = 101$ Bosons. *Left Panel* Shown are the energies of the final states $|N_{IN}, N_{OUT}\rangle = |41, 60\rangle$, $|51, 50\rangle$, and $|61, 40\rangle$ for a threshold $T = 0.6$. When one tunes the interaction λ_0 such that it lies in between the crossing points (marked by the *black dashed vertical lines*) of the *green* and *red/blue solid lines* at $\lambda_0 = \lambda_{c1/2}$, the energetically most favorable state will be with $N_{IN} \in (41, 61)$ and $N_{OUT} = N - N_{IN}$ particles. The *black arrow* shows the interaction $\lambda_0 = 0.005$ chosen for the propagation. See text for further discussion. *Right Panel* Shown is the nonescape probability $P_{not}(t)$ of $N = 101$ particles with $\lambda_0 = 0.005$ (*red solid line*). The *green dots* are an extrapolation obtained from a least squares fit of an exponential function to the actual data. According to this extrapolation, the final state is $|N_{IN} = 49, N_{OUT} = 52\rangle$ and hence in close agreement with the control objective aimed at in the *left Panel* of the figure. See text for further discussion. *Left Panel* of Figure reprinted from Ref. [1]

Panel of Fig. 7.14). This allows one to formulate a protocol for the deterministic production of a desired N-boson state. In the case of a fixed potential threshold the interactions λ_0 can be used to tune the energy $E_{TOT}(N_{IN}, N_{OUT}, T, \lambda_0)$ such that the energy of the desired number of bosons N_{IN} just becomes a bound state (see left Panel of Fig. 7.14). And in the case of fixed interactions the threshold T can be used to reach any desired number of N_{IN} bosons in the final state. With this approach, the counting statistics of the problem are fully under control. With just two parameters, it is hence possible to control the interplay of one-particle potential and interparticle interactions in order to manufacture any desired final state as the control's objective.

In summary, this chapter has shown that it is possible to exert control on the counting statistics and momentum density of the ejected bosons with the interplay of the threshold of the potential and the two-body interactions. The overall many-boson process is made up by single-particle processes which are well-described using the presented model (cf. Fig. 7.2). The momentum k_i^T of the ejection process is defined by the chemical potential μ_i of the N_{IN}-boson system in a parabolic trap. This chemical potential μ_i is firstly used to overcome the potential threshold T and secondly converted to kinetic energy E_{kin}^T. Hence, one finds peaks in the momentum distributions at $k_i^T = \sqrt{2m(\mu_i - T)}$. At precisely the peaks' positions, the first-order coherence of the bosons is lost, but the second order one is closer to being preserved. This illustrates the one-particle nature of the processes. It is hence also possible to control the coherence in the process by switching on or switching off certain final states with the interaction λ_0 or the threshold T. This diversity of achievable control objectives qualifies the system as a tunable quantum simulator for the mechanism of complicated ionization processes. The final states can be selected to resemble the open channels in the considered ionization process. The interaction can be used to tune the kinetic energies—which are associated with the ionization energies of the ionization process under consideration—of the ejected bosons.

References

1. A.U.J. Lode, S. Klaiman, O.E. Alon, A.I. Streltsov, S. Lorenz Cederbaum, Controlling the velocities and the number of emitted particles in the tunneling to open space dynamics. Phys. Rev. A **89**, 053620 (2014)
2. A. Öttl, S. Ritter, M. Köhl, T. Esslinger, Correlations and Counting Statistics of an Atom Laser. Phys. Rev. Lett. **95**, 090404 (2005)
3. I. Bloch, T.W. Hänsch, T. Esslinger, Atom Laser with a cw Output Coupler. Phys. Rev. Lett. **82**, 3008 (1999)
4. M. Köhl, T. Busch, K. Mølmer, T.W. Hänsch, T. Esslinger, Observing the profile of an atom laser beam. Phys. Rev. A **72**, 063618 (2005)
5. W. Ketterle, Nobel lecture: When atoms behave as waves: Bose–Einstein condensation and the atom laser. Rev. Mod. Phys. **74**, 1131–1151 (2002)
6. W. Ketterle, H.-J. Miesner, Coherence properties of Bose-Einstein condensates and atom lasers. Phys. Rev. A **56**, 3291 (1997)
7. R. Hanbury Brown, R.Q. Twiss, A Test of a New Type of Stellar Interferometer on Sirius. Nature **178**, 1046–1048 (1956)
8. R. Hanbury Brown, R.Q. Twiss, Interferometry of the Intensity Fluctuations in Light. I. Basic Theory: The Correlation between Photons in Coherent Beams of Radiation. Proc. Roy. Soc. London A **242** (1230), 300–324 (1957)
9. R. Hanbury Brown, R.Q. Twiss, Interferometry of the Intensity Fluctuations in Light. II. An Experimental Test of the Theory for Partially Coherent Light. Proc. Roy. Soc. London A **243**(1234), 291–319 (1958)
10. A.I. Streltsov, K. Sakmann, A.U.J. Lode, O.E. Alon, L.S. Cederbaum, *The Multiconfigurational Time-Dependent Hartree for Bosons Package*, version 2.3, Heidelberg (2012), see http://mctdhb.uni-hd.de

Chapter 8
Final Remarks and Outlook

Experience keeps a dear school, but fools will learn in no other.

Benjamin Franklin

8.1 Final Remarks

The present thesis consists of an application, exposition, benchmark and comparison of the currently most efficient numerical algorithm to solve the time-dependent many-boson Schrödinger equation: the multiconfigurational time-dependent Hartree method for bosons. The MCTDHB was applied to the problem of one-dimensional tunneling to open space of initially parabolically trapped coherent bosons in a potential without a threshold and also in a potential with a threshold. Throughout the investigation of the many-boson tunneling processes, various many-body models were formulated. These allow for a straightforward and intuitive understanding and control of the physics in the process.

The assessment of the capabilities of the methods was done by checking the convergence with analytical solutions of the HIM Hamiltonian and a time-dependent generalization of the HIM, the TDHIM. For the first time, numerically exact solutions, i.e., solutions of any desired accuracy of the TDSE even with time-dependent one- *and* two-body potentials have been achieved (see Chap. 3) and Ref. [1]. The problem of many-boson tunneling to open space consists in dynamics which involve the fragmentation of initially coherent samples—mean-field methods and lattice methods do not capture the correct many-body behavior. This was shown in Chap. 4 for the DNLS and BH/TEBD approaches.

In the case of zero threshold (Chap. 6), the tunneling to open space process of initially coherent ultracold bosons includes their gradual fragmentation. The mechanism behind can be explained by decomposing the many-body process in elemen-

A. U. J. Lode, *Tunneling Dynamics in Open Ultracold Bosonic Systems*,
Springer Theses, DOI: 10.1007/978-3-319-07085-8_8,

tary single-particle processes. Reasoning with the energetics of these single particle processes one finds: when a boson is ejected from a (close to) parabolic potential to open space, its energy—which it converts to kinetic energy—is the chemical potential: the difference in energy of the (close to) parabolically trapped N and $N-1$-particle system. These kinetic energies define a peak structure of the momentum distributions. The values at which the momentum density is peaked are predicted precisely by the model consideration in Chap. 5. Once the bosons are ejected, they propagate with different momenta and thus lose the coherence among each other and also with the source, which retains its coherence, see also Ref. [2].

If the threshold, i.e., the absolute value of the one-body potential in the asymptotic open space part, is changed, the physics of the process are changed, too (see Chap. 7). The momenta of the ejected bosons are shifted towards zero and vanish when the threshold crosses certain values. With the vanishing of the momenta the counting statistics of the final state change—a fraction of the system is left behind if the threshold is big enough to support a bound state of a certain number of particles. The reasoning with the energetics in the model consideration in Chap. 5 is modified: the available energy for the bosons is still defined by the chemical potential, but after the ejection the bosons have to first spend part of their energy to overcome the threshold before they convert the remainder to kinetic energy, which manifests in a peak in the momentum distribution. Hence, one can control the momentum of the ejected particles with the threshold. Furthermore, one can also tune the chemical potential with the interaction strength λ_0. A detailed analysis of the first order coherence of the process has consistently shown that the coherence dynamics can also be explained by the model, i.e., the ejected particles lose the first-order coherence among each other and with the source. An analysis of the second-order coherence shows the time-dependence of the (non-)sequentiality of the processes and their single-particle nature, see also Ref. [3].

It is appropriate to comment also on the analogs of the tunneling to open space process: ionization and atom lasers. The use of the investigated systems as quantum simulators for ionization processes was demonstrated. The control schemes found employing the threshold and the interaction can be used to calibrate the system to emulate almost any desired ionization process—by making the association of ionization energies with the ejection momenta of the bosons. In the case of the dynamics of atom lasers, the found dynamics show that it is very difficult to maintain the coherence of the sample. In all the repulsive cases studied, fragmentation, i.e., decoherence occurs dynamically in the open space part.

In summary the exploration of the many-boson tunneling process to open space in the present thesis not only explained the process on a many-body level, but also put forward an easy-to-implement and intuitive scheme of control of the counting statistics and many-body physics of the process.

8.2 Outlook

With a method that can solve a problem exactly, like MCTDHB, there is a plethora of opportunities. From the physical point of view, any quantum system is of course three-dimensional. It is, hence, of interest whether there is an effect of the dimensionality on the dynamics of the quasi one-dimensional systems studied here. It is a generally open question how tightly a system has to be confined in the transversal direction until it can be truly regarded as quasi one-dimensional. Certainly, the physics become more complex in the case of two-dimensional dynamics.

Another interesting step would be to change the particle statistics, i.e., to investigate whether the physics of the many-fermion tunneling to open space process is similar to the presented many-boson case. It is tempting to just adopt the found models and schemes for the many-boson tunneling also for a many-fermion system—yet, a proof that these models are applicable for fermions by exact numerical simulations or a suitable experiment (see Ref. [4]) is still needed.

In the presented cases, the interaction of the bosons was almost always repulsive. Repulsive interactions increase the chemical potentials. If one would make the interactions attractive, the chemical potentials would decrease and eventually become negative. The many-body properties of the process in such a case might be entirely different and rich.

The amount of control one can exert on the system with the threshold and the interactions is vast. The momentum distribution, final state counting statistics, and even the dynamics of coherence can be controlled. One could study the effects of further modifications of the potential, like including a second barrier or making the threshold time-dependent to achieve even more complicated control objectives.

The processes discussed in the present thesis all incorporate the loss of initial coherence. It would be interesting to see if it is possible to restore the coherence throughout the process by applying optimal control theory to a time-varying parameter like, for instance, the interaction or the potential threshold.

The previous points are steps to be taken in the exploration of the physics of this process. But from a more fundamental point of view, there is also a wealth of questions to be tackled. For instance, the definitions of a local measure for the coherence, formulated in Appendix B, could be an interesting theoretical concept in the physics of many-boson systems in general. Especially, for systems tunneling to open space, it seems as if the source is alway coherent whereas the ejected bosons always lose their coherence. Hence, a *local* measure of fragmentation is needed. Yet, the implementation of the necessary general transformations for many-body bases, see Chap. 2, is very complicated and presently not available. The concept of local fragmentation is just one of the examples of concepts and methods that are promising and not implemented. There is a plethora of theories in the MCTDH family, which deserve numerical implementation as for instance, the MCTDH for three kinds of different indistinguishable particles with up to three-body interactions, see [5].

References

1. A.U.J. Lode, K. Sakmann, O.E. Alon, L.S. Cederbaum, A.I. Streltsov, Numerically exact quantum dynamics of bosons with time-dependent interactions of harmonic type. Phys. Rev. A **86**, 063606 (2012)
2. A.U.J. Lode, A.I. Streltsov, K. Sakmann, O.E. Alon, L.S. Cederbaum, How an interacting many-body system tunnels through a potential barrier to open space. Proc. Natl. Acad. Sci. USA **109**, 13521 (2012)
3. A.U.J. Lode, S. Klaiman, O.E. Alon, A.I. Streltsov, S. Lorenz Cederbaum, Controlling the velocities and the number of emitted particles in the tunneling to open space dynamics. Phys. Rev. A **89**, 053620 (2014)
4. F. Serwane et al., Deterministic Preparation of a Tunable Few-Fermion System. Science **332**(6027), 336338 (2011)
5. O.E. Alon, A.I. Streltsov, K. Sakmann, A.U.J. Lode, J. Grond, L.S. Cederbaum, Recursive formulation of the multiconfigurational time- dependent hartree method for fermions, bosons and mixtures thereof in terms of one-body density operators. Chem. Phys. **401**, 2–14 (2012)

Appendix A
Particle Loss Operators

In order to define an operator, whose expectation value defines the υ-particle loss from an N-indistinguishable-particle system it is convenient to first define corresponding projectors employing Heaviside functions. For the sake of simplicity the considerations in this paragraph are restricted to the one-dimensional case. The Heaviside functions readily are the projectors up to a certain position C—in the case of a tunneling problem C is usually the position of the barrier. Yet, it is noteworthy, that it is straightforward to generalize these considerations to projectors also in 2 or 3 dimensions. The one-dimensional projectors read:

$$\Theta_k^- = \Theta(C - x_k) = (1 - \Theta_k^+); \qquad \Theta_k^+ = \Theta(x_k - C). \tag{A.1}$$

In principle, these operators measure the probability density of particle k to be in the interior, $x_k < C$ (Θ_k^-), or the exterior $x_k > C$ (Θ_k^+) parts of space. These operators are the building blocks for the general operators describing the υ-particle loss from an N-particle reservoir, denoted by $\hat{L}_\upsilon^N$. Clearly, the $\hat{L}_\upsilon^N$ will be simple products of the 1D projectors above and it will be possible to exploit the indistinguishability of the particles in the reservoir for their computation. It is instructive to start with the case, where one measures the probability that the whole system survives. This is the probability of all particles remaining in the interior, $x_k < C, \forall k$. Thus one finds

$$\hat{L}_0^N = \prod_{i=1}^{N} \Theta_i^- \tag{A.2}$$

The expectation value of this operator is completely equivalent to the above defined wave function-related nonescape probability $P_{not,\Psi}(t)$, cf. Eq. (2.29), where $\Omega = \{x_i < C, i = 1, ..., N\}$:

A. U. J. Lode, *Tunneling Dynamics in Open Ultracold Bosonic Systems*,
Springer Theses, DOI: 10.1007/978-3-319-07085-8,

$$\begin{aligned}\langle\Psi|\hat{L}_0^N|\Psi\rangle &= \int \Psi^*(x_1,...,x_N;t)\prod_{i=1}^{N}\Theta_i^-\Psi(x_1,...,x_N;t)dx_1\cdots dx_N \quad \text{(A.3)}\\ &= \int_{-\infty}^{C}\Psi^*(x_1,...,x_N;t)\Psi(x_1,...,x_N;t)dx_1\cdots dx_N = P_{not,\Psi}(t).\end{aligned}$$

In the last equality it is used that the action of $\hat{L}_0^N$ can be simply incorporated by restricting the boundaries for the integration on the different coordinates $x_1, ..., x_N$ to $x_i < C, i = 1, ..., N$. In the case in which all N particles of the N-particle reservoir are lost, one finds analogously:

$$\hat{L}_N^N = \prod_{i=1}^{N}\Theta_i^+. \tag{A.4}$$

It is instructive to write down the operators for the one- and two particle losses in order to generalize them to an arbitrary number $\upsilon \leq N$.

$$\hat{L}_1^N = \sum_{\kappa=1}^{N}\Theta_\kappa^+\prod_{\substack{i=1\\ i\neq\kappa}}^{N}\Theta_i^- = N\Theta_1^+\prod_{i=2}^{N}\Theta_i^-, \tag{A.5}$$

$$\hat{L}_2^N = \sum_{\{\kappa,\nu\}}\Theta_\kappa^+\Theta_\nu^+\prod_{\substack{i=1\\ i\neq\kappa\\ i\neq\nu}}^{N}\Theta_i^- = M_2\Theta_1^+\Theta_2^+\prod_{i=3}^{N}\Theta_i^-. \tag{A.6}$$

Here, the sums are running over all possible configurations of one or two of the N particles being in the exterior and the respective last equality uses the indistinguishability of the considered particles. M_2 denotes the cardinality of the different possibilities to realize a subset of two elements out of N. Clearly, $M_2 = \binom{N}{2}$ and $M_\upsilon = \binom{N}{\upsilon}$. It is now straightforward to write down the υ-of-N-particle loss operator:

$$\begin{aligned}\hat{L}_\upsilon^N &= \sum_{\{j_1,...,j_\upsilon\}}\left[\prod_{\kappa=1}^{\upsilon}\Theta_{j_\kappa}^+\right]\left[\prod_{\substack{i=1\\ i\notin\{j_1,...,j_\upsilon\}}}^{N}\Theta_i^-\right] \quad \text{(A.7)}\\ &= \binom{N}{\upsilon}\prod_{\kappa=1}^{\upsilon}\Theta_\kappa^+\prod_{\xi=\upsilon+1}^{N}\Theta_\xi^-. \quad \text{(A.8)}\end{aligned}$$

Here, the last equality uses the indistinguishability of the considered particles. With the expectation value of this operator it is possible to measure the loss of an arbitrary number υ of particles from a reservoir of N by defining an interior and an exterior region. Basically, the particle loss operators are nothing else but projectors on the

Hilbert space of a definite particle number whose coordinates are restricted. For instance, $\hat{L}_1^N$ is a projector on the Hilbert space where one coordinate is restricted to the exterior and all other $N - 1$ coordinates are restricted to the interior. Note that, for an N-particle system, these are N-body operators and hence very difficult to evaluate. In practical numerical computations, N-body operators' expectation values require N-dimensional integrals to be evaluated, which is a demanding task.

Appendix B
The Concept of Local Fragmentation

Fragmentation, i.e., the macroscopic (of order $\mathcal{O}(N)$) occupation of more than one natural orbital, is a quantity intimately related to the natural occupations $\rho_i^{(NO)}(t)$, i.e., the eigenvalues of the reduced one-body density matrix $\rho^{(1)}(x_1'|x_1;t)$, cf. Sect. 2.1.2 and Ref. [1]. The 1-RDM is a quantity defined on the whole Hilbert space of the system under consideration as an integral of the wave function. It is a natural question to ask how to assess the fragmentation of a system *locally*, because the full information might not be available in a given experimental setup. From a fundamental theoretical point of view there are two ways of approaching the question. The first idea takes the 1-RDM and applies a projection to a subspace to obtain a new, truncated 1-RDM from which one computes the local natural occupations. The second way to obtain local occupation numbers applies the projection to the subspace on the wave function and computes from the truncated wave function a new 1-RDM on the considered subspace, from which in turn one can obtain local natural occupations. The first is termed 1-RDM-related local natural occupations and the second way is termed wave function-related local natural occupations. The scope of this section is to clarify the properties and the differences of the two approaches.

B.1 The 1-RDM-Related Local Natural Occupations

To define local occupation numbers $\tilde{\rho}_{i,\tau}^{(NO)}$ and local natural orbitals $\tilde{\phi}_{i,\tau}^{(NO)}$ it is a natural approach to simply truncate the 1-RDM by projection to some subspace $\Omega = \{(x_1, ..., x_N)\,|x_j \leq x_{\tau,j}, j = 1, ..., N\}$ of the entire space $\mathcal{H}$. For the sake of simplicity one-dimensional systems are considered in this subsection. The projector $\hat{P}$ onto Ω is:

$$\hat{P} = \prod_{j=1}^{N} \hat{p}_j = \prod_{j=1}^{N} \Theta(x_{\tau,j} - x_j). \tag{B.1}$$

A. U. J. Lode, *Tunneling Dynamics in Open Ultracold Bosonic Systems*,
Springer Theses, DOI: 10.1007/978-3-319-07085-8,

Now one applies $\hat{P}$ to the 1-RDM $\rho^{(1)}(x_1|x_1';t)$:

$$\begin{aligned} \hat{P}\rho^{(1)}(x_1|x_1';t) &= \hat{p}_1\rho^{(1)}(x_1|x_1';t) \\ &= \hat{p}_1 N\int dx_2\cdots dx_N \Psi^*(x_1',x_2,...,x_N;t)\Psi(x_1,...,x_N;t). \end{aligned} \tag{B.2}$$

Here, it was firstly used that the 1-RDM is a function of only x_1 and x_1', so only $\hat{p}_1$ acts onto it. Secondly, the definition of $\rho^{(1)}$, see Eq. (2.24), was inserted. Next, one uses the possibility to express the 1-RDM expanded in a basis set ϕ_i, $i = 1, ..., M$, cf. the paragraph on natural orbitals and occupations:

$$\begin{aligned} \hat{p}_1\rho^{(1)}(x_1|x_1';t) &= \hat{p}_1\sum_{k,q=1}^{M}\rho_{kq}\phi_i^*(x_1',t)\phi_i(x_1,t) \\ &= \sum_{k,q=1}^{M}\rho_{kq}\hat{p}_1\phi_i^*(x_1',t)\hat{p}_1\phi_i(x_1,t) \\ &\equiv \sum_{k,q=1}^{M}\tilde{\rho}_{kq}\phi_{i,\tau}^*(x_1',t)\phi_{i,\tau}(x_1,t) \\ &\equiv \sum_{i=1}^{M}\tilde{\rho}_{i,\tau}^{(NO)}(t)\tilde{\phi}_{i,\tau}^{*(NO)}(x_1',t)\tilde{\phi}_{i,\tau}^{(NO)}(x_1,t). \end{aligned} \tag{B.3}$$

In the first step one uses the fact that $\hat{p}_1$ only acts on the functions used to expand $\rho^{(1)}$. In the second step, the respective truncated basis $\phi_{i,\tau} = \hat{p}_1\phi_i$, $i = 1, ..., M$ was introduced. In the last step the obtained truncated 1-RDM was diagonalized to obtain a set of truncated occupations, $\tilde{\rho}_{i,\tau}^{(NO)}(t)$, as well as a set of truncated natural orbitals $\tilde{\phi}_{i,\tau}^{(NO)}(x,t)$. Equation (B.3) also are an easy, practical guide for the implementation of this analysis tool.

B.2 The Wave function-Related Local Natural Occupations

In this section the notion of wave function-related local natural occupation numbers is introduced. In order to define local occupation numbers $\rho_{i,\tau}^{(NO)}(t)$ and local natural orbitals $\phi_{i,\tau}^{(NO)}$ starting from the wave function, one first uses the projector $\hat{P}$ defined in the previous subsection to obtain a truncated wave function Ψ_τ. This is done in the following specifically for the case of a multiconfigurational wave function:

$$\begin{aligned}
\Psi_\tau(x_1, ..., x_N, t) &= \hat{P}\Psi(x_1, ..., x_N, t) \\
&= \hat{P}\sum_{\mathbf{n}} C_{\mathbf{n}}(t)|\mathbf{n}; \mathbf{t}\rangle \\
&= \sum_{\mathbf{n}} C_{\mathbf{n}}(t)\hat{P}|\mathbf{n}; \mathbf{t}\rangle \\
&\equiv \sum_{\mathbf{n}} C_{\mathbf{n}}(t)|\mathbf{n}; \mathbf{t}\rangle_\tau .
\end{aligned} \tag{B.4}$$

Here, the multiconfigurational ansatz for the wave function is inserted in the second line of the above equation. In this case, the projector $\hat{P}$ acts only on the configurations $|\mathbf{n}, \mathbf{t}\rangle$ (third of the above equalities) and this leads to the introduction of new, projected configurations $|\mathbf{n}; \mathbf{t}\rangle_\tau = \hat{\mathbf{P}}|\mathbf{n}; \mathbf{t}\rangle$. Two things have to be noted here: first, that the new set of configurations is no longer orthogonal (!) and, second, that the projector $\hat{P}$ again only acts on the single particle functions constructing the permanents. In principle one thus relies on the same basis set $\phi_{i,\tau}$, $i = 1, ..., M$ as in the previous paragraph. To continue, one constructs a truncated 1-RDM $\rho_\tau(x_1|x_1'; t)$ from the truncated wave function Ψ_τ:

$$\begin{aligned}
\rho_\tau(x_1|x_1'; t) &= N\int dx_2 \cdots dx_N \Psi_\tau^*(x_1', x_2, ..., x_N)\Psi_\tau(x_1, x_2, ..., x_N) \\
&= N\int_\Omega dx_2 \cdots dx_N \hat{p}_1\Psi^*(x_1', x_2, ..., x_N)\hat{p}_1\Psi(x_1, x_2, ..., x_N).
\end{aligned} \tag{B.5}$$

Here, the first identity is simply the definition of $\rho^{(1)}$ with Ψ replaced by Ψ_τ and in the second identity the action of the projectors was incorporated as the boundaries of the integration. Of course, as in the previous subsection, also this truncated 1-RDM can be represented in the basis $\phi_{i,\tau}$, $i = 1, ..., M$ with weights $\rho'_{kq}(t)$:

$$\begin{aligned}
\rho_\tau^{(1)}(x_1|x_1'; t) &= \sum_{k,q=1}^{M} \rho'_{kq}\phi^*_{i,\tau}(x_1', t)\phi_{i,\tau}(x_1, t) \\
&\equiv \sum_{i=1}^{M} {\rho'}_{i,\tau}^{(NO)}(t)\phi_{i,\tau}^{*(NO)}(x_1', t)\phi_{i,\tau}^{(NO)}(x_1, t).
\end{aligned} \tag{B.6}$$

Note that $\rho'_{kq}(t) \neq \tilde{\rho}_{kq}(t)$. This is because the space where the wave function is integrated or, in other terms, the applied projectors are different, see Eqs. (B.2) and (B.3), from the case of the truncated $\rho^{(1)}$ in the previous subsection. To assess and understand better the concept of local fragmentation, it is instructive to compare the 1-RDM based approach to the present wave function-based approach directly.

B.3 Comparison of the Wave function- and 1-RDM-Based Approaches

The simplest way to compare two quantities is to simply calculate their difference. For the wave function-based and 1-RDM based local 1-RDMs this is achievable straightforwardly by subtracting Eq. (B.5) from (B.2):

$$\begin{aligned}
\rho'_{1,\tau} - \tilde{\rho}_{1,\tau} \quad &= \quad \hat{p}_1 N \int dx_2 \cdots dx_N \Psi^*(x_1', x_2, ..., x_N; t)\Psi(x_1, ..., x_N; t) \\
&\quad - N \int_{\Omega} dx_2 \cdots dx_N \hat{p}_1 \Psi^*(x_1', x_2, ..., x_N)\hat{p}_1 \Psi(x_1, ..., x_N) \\
&= \quad \hat{p}_1 \int_{\mathcal{H}\backslash\Omega} dx_2 \cdots dx_N \Psi^*(x_1', x_2, ..., x_N)\Psi(x_1, ..., x_N). \qquad \text{(B.7)}
\end{aligned}$$

A comment on the two approaches from a practical point of view is in order. The computation of the wave function-related local occupations is a numerically demanding task because it relies on N-body operators or quantities. In particular, the evaluation of the integral in Eq. (B.5) demands (unitary) transformations of permanents (see Eqs. (2.16), (2.18)) which constitute a big numerical effort and are not yet implemented in the software developed (see Ref. [2]) and in use throughout this thesis.

Appendix C
Reduced One-Body Density Matrix and Momentum Distribution of a Gross–Pitaevskii Wave Function Composed of Two Plane Waves

This Appendix demonstrates that one can in principle construct coherent quantum product states for $N = 2$ bosons incorporating two momenta.

Assumed GP Orbital:
One assumes a Gaussian $g(x)$ inside the well, $x < x_c$, and 2 plane waves with momenta k_1 and k_2 outside, $x > x_c$, where the Gaussian is 0 (no overlap is assumed).

$$\varphi(x) = g(x) + \theta(x - x_C)\left[e^{ik_1 x} + e^{ik_2 x}\right]. \tag{C.1}$$

Construction of the GP-Wave function:
Eq. (C.1) is used and the normalization is of no significance here and skipped therefore:

$$\begin{aligned}
\Psi_{GP} &= \prod_{i=1}^{N} \varphi(x_i); \qquad N := 2 \\
&= \prod_{i=1}^{2} g(x_i) + \theta(x_i - x_C)\left[e^{ik_1 x_i} + e^{ik_2 x_i}\right] \qquad \text{(C.2)}\\
&= g(x_1)g(x_2) \\
&\quad + \theta_{x_C}\left[e^{ik_1(x_1+x_2)} + e^{i(k_1x_1+k_2x_2)} + e^{i(k_2x_1+k_1x_2)} + e^{i(k_2x_1+k_2x_2)}\right]. \qquad \text{(C.3)}
\end{aligned}$$

Construction of the RDM:

$$\begin{aligned}
\rho^{(1)}(x_1|x_1') &= N\int \Psi^*(x_1', x_2, ..., x_N) \times \Psi(x_1, ..., x_N)dx_2 \cdots dx_N \\
&= 2\int \Psi^*_{GP}(x_1', x_2) \times \Psi_{GP}(x_1, x_2)dx_2 \qquad \text{(C.4)}\\
&= \int \Big\{ (g(x_1))^2\, g(x_1')g(x_2)
\end{aligned}$$

A. U. J. Lode, *Tunneling Dynamics in Open Ultracold Bosonic Systems*,
Springer Theses, DOI: 10.1007/978-3-319-07085-8,

$$\begin{aligned}&+\quad \theta_{x_C}\times\left[e^{-ik_1(x_1'+x_2)}+e^{-i(k_1x_1'+k_2x_2)}+e^{-i(k_2x_1'+k_1x_2)}+e^{-i(k_2x_1'+k_2x_2)}\right]\\ &\times\quad \left[e^{ik_1(x_1+x_2)}+e^{i(k_1x_1+k_2x_2)}+e^{i(k_2x_1+k_1x_2)}+e^{i(k_2x_1+k_2x_2)}\right]\Big\}dx_2,\end{aligned}\tag{C.5}$$

using the abbreviation $\theta_{x_C} := \theta(x_1 - x_C)\theta(x_2 - x_C)$ in the step from Eq. (C.4) to Eq. (C.5). Evaluating the integrand, $I = \Psi^*(x_1, x_1')\Psi(x_1, x_2)$, of Eq. (C.5):

$$\begin{aligned}&I=(g(x_1))^2\,g(x_1')g(x_2)+\theta_{x_C}\times\\ &\Big\{e^{i(k_1x_2-k_1x_1')}+e^{i(k_2x_2-k_1x_1')}+e^{i(k_2x_1+k_1x_2-k_1(x_1+x_1'))}+e^{i(k_2x_1+k_2x_2-k_1(x_1+x_1'))}\\ &\quad+\quad e^{i(k_1x_2-k_2x_1')}+e^{i(k_2x_2-k_2x_1')}+e^{i(k_2x_1+k_1x_2-k_1x_1-k_2x_1')}+e^{i(k_2x_1+k_2x_2-k_1x_1-k_2x_1')}\\ &\quad+\quad e^{i(k_1x_1+k_1x_2-k_2x_1-k_1x_1')}+e^{i((k_1-k_2)x_1+k_2x_2-k_1x_1'}+e^{i(k_1x_2-k_1x_1')}+e^{i(k_2x_2-k_1x_1')}\\ &\quad+\quad e^{i((k_1-k_2)x_1+k_1x_2-k_2x_1')}+e^{i((k_1-k_2)x_1+k_2x_2-k_2x_1')}+e^{i(k_1x_2-k_2x_1')}+e^{i(k_2(x_2-x_1'))}\Big\}.\end{aligned}\tag{C.6}$$

Performing the Integration, $\rho^{(1)} = \int I dx_2$, using the abbreviations and assuming the existence of $A = \int \theta_{x_C} e^{i(k_1x_2)} dx_2$ and $B = \int \theta_{x_C} e^{i(k_2x_2)} dx_2$ and $C = \int g(x_2) dx_2$

$$\begin{aligned}\rho^{(1)}\quad&=\int C\,(g(x_1))^2\,g(x_1')+\theta_{x_C}\times\\ &\Big\{Ae^{-ik_1x_1'}+Be^{ik_1x_1'}+Ae^{i(k_2x_1-k_1(x_1+x_1'))}+Be^{i((k_2-k_1)x_1-k_1x_1')}\\ &+\quad Ae^{-ik_2x_1'}+Be^{-ik_2x_1'}+Ae^{i((k_2-k_1)x_1-k_2x_1')}+Be^{i((k_2-k_1)x_1-k_2x_1')}\\ &+\quad Ae^{i((k_1-k_2)x_1-k_1x_1')}+Be^{i((k_1-k_2)x_1-k_1x_1')}+Ae^{-ik_1x_1'}+Be^{-ik_1x_1'}\\ &+\quad Ae^{i((k_1-k_2)x_1-k_2x_1')}+Be^{i((k_1-k_2)x_1-k_2x_1')}+Ae^{-ik_2x_1'}+e^{-ik_2x_1'}\Big\}.\end{aligned}\tag{C.7}$$

After simplifications, one obtains:

$$\begin{aligned}\rho^{(1)}=&\int C\,(g(x_1))^2\,g(x_1')+\theta_{x_C}\times\\ &\Big\{\,(2(A+B))\left(e^{-ik_1x_1'}+e^{-ik_2x_1'}\right)\\ &+(A+B)\left[e^{i((k_2-k_1)x_1-k_1x_1')}+e^{i((k_1-k_2)x_1-k_1x_1')}\right.\\ &\left.+\,e^{i((k_1-k_2)x_1-k_2x_1')}+e^{i((k_2-k_1)x_1-k_2x_1')}\right]\Big\}.\end{aligned}\tag{C.8}$$

Calculation of the Momentum Distribution:
By definition the momentum distribution is the Fourier transform of the RDM: $\rho(j) = \int dx_1 dx_1' e^{-ij(x_1-x_1')}\rho^{(1)}(x_1|x_1')$. Using the abbreviations $\aleph(j)$ for the Gaussian-shaped Fourier transforms of the Gaussian $g(x)$ one arrives at:

$$\begin{aligned}
\rho^{(1)}(j) = C\aleph(j) + \int \Big\{ & \theta_{x_C} \qquad\qquad\qquad\qquad\qquad\qquad\qquad\qquad\qquad\qquad\qquad\qquad \text{(C.9)} \\
& \times 2A\left[e^{-i((k_1-j)x_1'+jx_1)} + e^{-i((k_2-j)x_1'+jx_1)}\right] \\
& + 2B\left[e^{-i((k_2-j)x_1'+jx_1)} + e^{-i((k_1-j)x_1'+jx_1)}\right] \\
& + (A+B)\left[e^{-i((k_2-k_1)x_1-k_1x_1'-j(x_1-x_1'))} + e^{-i((k_1-k_2)x_1-k_1x_1'-j(x_1-x_1'))}\right]\Big\} dx_2 \\
= C\aleph(j) & + (2A+2B)\left[\delta(j-k_1) + \delta(j-k_2)\right] \\
& + (A+B)\left[\delta(j-k_1)\delta(j-(k_2-k_1))\right] \\
& + (A+B)\left[\delta(j-k_1)\delta(j-(k_1-k_2))\right] \qquad\qquad\qquad\qquad\qquad\qquad \text{(C.10)} \\
= C\aleph(j) & + (2A+2B)\left[\delta(j-k_1) + \delta(j-k_2)\right]. \qquad\qquad\qquad\qquad\qquad\qquad \text{(C.11)}
\end{aligned}$$

where Eq. (C.11) follows from the fact that $k_2 \neq 0$ in Eq. (C.10).
A comment is in place here: the momentum density and reduced density matrix described above do resemble the ones obtained in exact numerical simulations (cf. Chaps. 6, 7). The key difference is, that the exact solutions do not preserve the coherence whenever there is more than one momentum present. This is caused by the state constructed above being energetically much higher than its prescribed fragmented counterpart (cf. Appendices D, G). States of higher energy are excluded from the dynamics by the TDVP [3].

Appendix D
Derivation of the Reduced One-body Density for a System Tunneling with Two Momenta

The RDM of the $N = 2$ boson system with the wave function constructed in the orbitals given in Eq. (5.24) reads as follows:

$$\begin{aligned}
\rho^{(1)}(x_1|x_1') =& \int \Psi(x_1, ..., x_N) \times \Psi^*(x_1', x_2, ..., x_N) dx_2 \cdots dx_N \\
=& \int \Psi(x_1, x_2) \times \Psi^*(x_1', x_2) dx_2 \\
=& (C_{\mathbf{n_1}})^2 \int dx_2 \left[e^{-\frac{1}{2}(x_1^2+(x')_1^2+2x_2^2)} + \theta(x-x_c) e^{ik_1(x_1-x_1')} \right] \\
& + \theta(x-x_c) C_{\mathbf{n_1}} C_{\mathbf{n_2}} \int dx_2 \left[e^{i(k_1(x_1+x_2)-k_1x_1'-k_2x_2)} + e^{i(k_1(x_1+x_2)-k_1x_2-k_2x_1')} \right] \\
& + \theta(x-x_c) C_{\mathbf{n_1}} C_{\mathbf{n_2}} \int dx_2 \left[e^{i((k_1x_1+k_2x_2)-k_1(x_1'+x_2))} + e^{i(k_1x_2+k_2x_1-k_1(x_1'+x_2))} \right] \\
& + \theta(x-x_c) (C_{\mathbf{n_2}})^2 \int dx_2 \left[e^{i(k_1(x_1-x_1'))} + e^{i(k_2(x_1-x_1'))} \right] \\
& + \theta(x-x_c) (C_{\mathbf{n_2}})^2 \int dx_2 \left[e^{i(k_1x_1-k_1x_2+k_2x_2-k_2x_1')} + e^{i(k_1x_2+k_2x_1-k_1x_1'-k_2x_2)} \right] \\
& + \theta(x-x_c) (C_{\mathbf{n_3}})^2 \int dx_2 \left[e^{ik_2(x_1+x_2)-ik_2(x_1'+x_2)} \right] \\
& + \theta(x-x_c) C_{\mathbf{n_3}} C_{\mathbf{n_2}} \int dx_2 \left[e^{-i(k_2(x_1'+x_2)} (e^{i(k_1x_1+k_2x_2)} + e^{i(k_1x_2+k_2x_1)}) \right] \\
& + \theta(x-x_c) C_{\mathbf{n_3}} C_{\mathbf{n_2}} \int dx_2 \left[e^{i(k_2(x_1+x_2)} (e^{-i(k_1x_1'+k_2x_2)} + e^{-i(k_1x_2+k_2x_1')}) \right] \\
& + \theta(x-x_c) C_{\mathbf{n_3}} C_{\mathbf{n_1}} \int dx_2 \left[e^{-ik_2(x_2+x_1')} e^{ik_1(x_1+x_2)} + e^{ik_2(x_2+x_1)} e^{-ik_1(x_1'+x_2)} \right].
\end{aligned} \tag{D.1}$$

This equation drastically reduces when one takes the diagonal $x_1 = x_1'$ and uses the addition theorems $\cos^2\left(\frac{\lambda}{2}\right) = \frac{1}{2}(1+\cos(\lambda))$ and $\cos(\lambda) = \frac{e^{i\lambda}+e^{-i\lambda}}{2}$:

A. U. J. Lode, *Tunneling Dynamics in Open Ultracold Bosonic Systems*,
Springer Theses, DOI: 10.1007/978-3-319-07085-8,

$$
\begin{aligned}
\rho(x_1|x_1) \quad &= (C_{\mathbf{n_1}})^2 \left[\sqrt{\pi} e^{-x_1^2}\right] \\
&+ C_{\mathbf{n_1}} C_{\mathbf{n_2}} \theta(x - x_c) \left[4\cos^2(x_1(\frac{k_1 - k_2}{2}))\right] \\
&+ (C_{\mathbf{n_2}})^2 \theta(x - x_c) \left[4\cos^2(x_1(\frac{k_1 - k_2}{2})\right] \\
&+ C_{\mathbf{n_3}} C_{\mathbf{n_2}} \theta(x - x_c) \left[4\cos^2(\frac{(k_1 - k_2)}{2} x_1)\right] \\
&+ C_{\mathbf{n_3}} C_{\mathbf{n_1}} \theta(x - x_c) \left[2\cos((k_1 - k_2)x_1)\right] \\
&+ \theta(x - x_c) \left[2(C_{\mathbf{n_3}})^2 + 2(C_{\mathbf{n_2}})^2\right] x_2 \\
&= (C_{\mathbf{n_1}})^2 \left[\sqrt{\pi} e^{-x_1^2}\right] \\
&+ \theta(x - x_c) \left[(C_{\mathbf{n_2}})^2 + C_{\mathbf{n_3}} C_{\mathbf{n_2}} + C_{\mathbf{n_1}} C_{\mathbf{n_2}}\right] \left[4\cos^2(x_1(\frac{k_1 - k_2}{2}))\right] \\
&+ \theta(x - x_c) C_{\mathbf{n_3}} C_{\mathbf{n_1}} 2\cos((k_1 - k_2)x_1) \\
&+ \theta(x - x_c) \left[2(C_{\mathbf{n_3}})^2 + 2(C_{\mathbf{n_2}})^2\right] x_2. \qquad \text{(D.2)}
\end{aligned}
$$

As the reduced one body density is a function of x_1 and x_1' the term with x_2 is actually a constant coming from the undefined integral in the x_2 degree of freedom. Thus, $x_2 = \xi = const.$, is furthermore assumed. Thus one gets after introducing the abbreviations $D = (C_{\mathbf{n_1}})^2$; $E = \theta(x - x_c)\left[(C_{\mathbf{n_2}})^2 + C_{\mathbf{n_3}} C_{\mathbf{n_2}} + C_{\mathbf{n_1}} C_{\mathbf{n_2}}\right]$; $G = \theta(x - x_c)\left[2(C_{\mathbf{n_3}})^2 + 2(C_{\mathbf{n_2}})^2\right]\xi$ and $F = \theta(x - x_c) C_{\mathbf{n_3}} C_{\mathbf{n_1}}$:

$$
\begin{aligned}
\rho(x_1|x_1) = D &\left[\sqrt{\pi} e^{-x_1^2}\right] \\
&+ 4E \left[\cos^2(x_1(\frac{k_1 - k_2}{2}))\right] \\
&+ 2F\cos((k_1 - k_2)x_1) \\
&+ G. \qquad \text{(D.3)}
\end{aligned}
$$

Appendix E
Derivation of the Diagonal of the Reduced Two-body Density for a System Tunneling with Two Momenta

The two-body density of the $N = 2$ boson system with the wave function constructed from the orbitals given in Eq. (5.24) reads as follows:

$$\begin{aligned}\rho^{(2)}(x_1, x_2|x_1, x_2; t) &= \int \Psi(x_1, ..., x_N)\Psi^*(x_1, ..., x_N)dx_3 \cdots dx_N \\ &= \Psi(x_1, x_2)\Psi^*(x_1, x_2) \\ &= (C_{\mathbf{n_1}})^2 \left[e^{-(x_1^2+x_2^2)}\right] \\ &\quad + \theta(x - x_c)(C_{\mathbf{n_1}} \frac{C_{\mathbf{n_2}}}{\sqrt{2}}) \left[e^{i(k_1-k_2)x_1} + e^{i(k_2-k_1)x_1} + e^{i(k_1-k_2)x_2} + e^{i(k_2-k_1)x_2}\right] \\ &\quad + \theta(x - x_c)(C_{\mathbf{n_3}})^2 \left[e^{i[(k_1-k_2)x_1+(k_2-k_1)x_2]} + e^{i[(k_1-k_2)x_2+(k_2-k_1)x_1]}\right].\end{aligned} \tag{E.1}$$

The indices $\mathbf{n_1}, \mathbf{n_2}, \mathbf{n_3}$ refer to the configurations $|2, 0\rangle, |1, 1\rangle, |0, 2\rangle$, respectively. Introducing the abbreviations $A = (C_{\mathbf{n_1}})^2$; $B =; \theta(x - x_c)(C_{\mathbf{n_1}} \frac{C_{\mathbf{n_2}}}{\sqrt{2}})$ and $C = \theta(x - x_c)(C_{\mathbf{n_3}})^2$ and using the relation $\cos(\lambda) = \frac{e^{i\lambda}+e^{-i\lambda}}{2}$ one arrives at the following:

$$\begin{aligned}\rho^{(2)}(x_1, x_2|x_1, x_2; t) \quad &= A\left[e^{-(x_1^2+x_2^2)}\right] \\ &\quad + B\left[2\left(\cos((k_1 - k_2)x_1) + \cos((k_1 - k_2)x_2)\right)\right] \\ &\quad + C\left[2\cos((k_1 - k_2)x_1)\cos((k_1 - k_2)x_2)\right].\end{aligned} \tag{E.2}$$

The second row of the equation above can be transformed to a single factor via the relation $\cos(\lambda) + \cos(\lambda') = \cos(\frac{\lambda+\lambda'}{2}) \cdot \cos(\frac{\lambda-\lambda'}{2})$ times the coefficient B: if one further assumes real coefficients the diagonal of $\rho^{(2)}$ reads as follows:

$$\begin{aligned}\rho^{(2)}(x_1, x_2|x_1, x_2; t) &= A\left[e^{-(x_1^2+x_2^2)}\right] \\ &\quad + B\left[4\left(\cos((k_1 - k_2)\frac{(x_1 + x_2)}{2})\cos((k_1 - k_2)\frac{(x_1 - x_2)}{2})\right)\right] \\ &\quad + C\left[2\cos((k_1 - k_2)x_1)\cos((k_1 - k_2)x_2)\right].\end{aligned} \tag{E.3}$$

A. U. J. Lode, *Tunneling Dynamics in Open Ultracold Bosonic Systems*,
Springer Theses, DOI: 10.1007/978-3-319-07085-8,

Appendix F

Derivation of the Diagonal of the Second Order Correlation Function for a System Tunneling with Two Momenta

The construction of $|g^{(2)}(x_1, x_2|x_1, x_2, t)|^2$ (definition see Sect. 2.1.2) for the wave function constructed from the orbitals in Eq. (5.24) is presented in the following. As in the previous Appendix E, the indices $\mathbf{n_1}, \mathbf{n_2}, \mathbf{n_3}$ refer to the configurations $|2, 0\rangle, |1, 1\rangle, |0, 2\rangle$, respectively. Using the abbreviations $\alpha = x_1(\frac{(k_1-k_2)}{2})$; $\beta = x_2(\frac{(k_1-k_2)}{2})$; $A = (C_{\mathbf{n_1}})^2$; $B =; \theta(x - x_c)(C_{\mathbf{n_1}} \frac{C_{\mathbf{n_2}}}{\sqrt{2}})$; $C = \theta(x - x_c)(C_{\mathbf{n_3}})^2$; $D = (C_{\mathbf{n_1}})^2$; $E = \theta(x - x_c)\left[(C_{\mathbf{n_2}})^2 + C_{\mathbf{n_3}} C_{\mathbf{n_2}} + C_{\mathbf{n_1}} C_{\mathbf{n_2}}\right]$ and $F = \theta(x - x_c) C_{\mathbf{n_3}} C_{\mathbf{n_1}}$ and defining straightforwardly:

$$
\begin{aligned}
g^{(2)}(x_1, x_2|x_1, x_2) &= \frac{\rho^{(2)}(x_1, x_2|x_1, x_2)}{\sqrt{\rho^{(1)}(x_1|x_1)\rho(1)(x_2|x_2)}} \\
|g^{(2)}(x_1, x_2|x_1, x_2)|^2 &\equiv \frac{\mu}{\nu}.
\end{aligned}
$$

One finds the following for μ and ν:

$$
\begin{aligned}
\mu \quad &= A^2 e^{-(2x_1^2+2x_2^2)} + \theta(x - x_c)[A^2 + 2AB\,(\cos(\alpha) + \cos(\beta)) \\
&\quad + (\cos(\alpha)\cos(\beta))\left[AC + 4BC(\cos(\alpha) + \cos(\beta)) + 4C^2(\cos(\alpha)\cos(\beta))\right] \\
&\quad + 16B^2 \cos^2(\alpha + \beta)\cos^2(\alpha - \beta)],
\end{aligned} \tag{F.1}
$$

and

$$
\begin{aligned}
\nu &= D^2 e^{-(x_1^2+x_2^2)} + \theta(x - x_c)[E^2 + 4EF(\cos^2(\alpha) + \cos^2(\beta)) \\
&\quad + 16F^2(\cos^2(\alpha)\cos^2(\beta))].
\end{aligned} \tag{F.2}
$$

A. U. J. Lode, *Tunneling Dynamics in Open Ultracold Bosonic Systems*,
Springer Theses, DOI: 10.1007/978-3-319-07085-8,

Appendix G

Densities of a Model with Delocalized Orbitals and Two Momenta

The scope of this appendix is to derive the resulting densities $\rho^{(1)}$ and $\rho(2)$ with the ansatz for the orbitals given in Eq. (5.26), where one assumes the interior $\mu(x)$ part to be a Gaussian. This assumption yields the orbitals:

$$\phi_1(x) = e^{-\frac{x^2}{2}} \cdot e^{ik_1 x} \quad ; \quad \phi_2(x) = e^{-\frac{x^2}{2}} \cdot e^{ik_2 x}. \tag{G.1}$$

Furthermore, the description is restricted here to $N = 2$ bosons. In this case the possible permanents contributing to the full wave function are $|2, 0\rangle$, $|1, 1\rangle$, and $|0, 2\rangle$. Explicitly, they read:

$$\begin{aligned}
|2, 0\rangle &= e^{ikx - \frac{x^2}{2} + ik_1 y - \frac{y^2}{2}} \\
|1, 1\rangle &= e^{ik_1 x - \frac{x^2}{2} + ik_2 y - \frac{y^2}{2}} + e^{ik_2 x - \frac{x^2}{2} + ik_1 y - \frac{y^2}{2}} \\
|0, 2\rangle &= e^{ik_2 x - \frac{x^2}{2} + ik_2 y - \frac{y^2}{2}}.
\end{aligned} \tag{G.2}$$

From this basis, it is straightforward to form a multiconfigurational wave function. The above orbitals and permanents are not normalized, but one can just assume that the normalization is absorbed in the coefficients, u, v, w, of the multiconfigurational expansion:

$$\begin{aligned}
|\Psi\rangle &= u|2, 0\rangle + v|1, 1\rangle + w|0, 2\rangle \\
&= e^{-\frac{x^2}{2} - \frac{y^2}{2}} \left(e^{ik_1(x+y)} u + e^{i(k_1 x + k_2 y)} v + e^{i(k_2 x + k_1 y)} v + e^{ik_2(x+y)} w \right).
\end{aligned} \tag{G.3}$$

Having at hands the wave function one can write down the two-body density $\rho^{(2)}(x, y)$:

A. U. J. Lode, *Tunneling Dynamics in Open Ultracold Bosonic Systems*,
Springer Theses, DOI: 10.1007/978-3-319-07085-8,

$$\begin{aligned}\rho^{(2)}(x,y) &= Tr_{x_3 \cdots x_N}\left[|\Psi\rangle\langle\Psi|\right] = \Psi^*(x,y)\Psi(x,y)\\ &= e^{-x^2-y^2}\Big(u^2+2v^2+w^2\\ &\quad + 2v(v\cos[(k_2-k_1)(x-y)]\\ &\quad + (u+w)(\cos[(k_2-k_1)x]+\cos[(k_2-k_1)y]))\\ &\quad + 2uw\cos[(k_2-k_1)(x+y)]\big)\,. \end{aligned} \tag{G.4}$$

In the derivation the same addition theorems for trigonometric functions as in Appendix E were used. It is interesting to note that the oscillatory pattern is identical to the one presented in Appendix E. It remains to evaluate the reduced one-body density $\rho^{(1)}$:

$$\begin{aligned}\rho^{(1)}(x,y) &= Tr_{x_2,\cdots,x_N}|\Psi\rangle\langle\Psi|\\ &= \int dx_2\Psi^*(y,x2)\Psi(x,x_2)\\ &= \Bigg[\frac{1}{2}e^{-ik_2x-ik_1x-\frac{x^2}{2}-\frac{y^2}{2}}\sqrt{\pi}\\ &\quad\times\Big(e^{i(k_2x+ky)}\Big(u^2+v^2\Big)+e^{ik_2(x+y)}v(u+w)\\ &\quad + e^{ik_1(x+y)}v(u+w)+e^{i(k_1x+k_2y)}\Big(v^2+w^2\Big)\Big)\\ &\quad\times Erf[x_2]+\frac{1}{2}e^{\frac{1}{4}\left(-k_2^2-k_1^2+2k_2(k_1-2ix)-4ik_1x-2\left(x^2+y^2\right)\right)}\\ &\quad\times\sqrt{\pi}\Big(\Big(e^{ik_1y}u+e^{ik_2y}v\Big)\Big(e^{ik_2x}v+e^{ik_1x}w\Big)\\ &\quad\times Erf\left[\frac{1}{2}(ik_2-ik_1+2x_2)\right]\\ &\quad+\Big(e^{ik_2x}u+e^{ik_1x}v\Big)\Big(e^{ik_1y}v+e^{ik_2y}w\Big)\\ &\quad\times\ Erf\left[\frac{1}{2}(-ik_2+ik_1+2x_2)\right]\Big)\Bigg]_{-\infty}^{\infty}\,. \end{aligned} \tag{G.5}$$

When finally taking the limits in the above expression the terms dependent on x_2 and the error functions Erf disappear:

$$\begin{aligned}\rho^{(1)}(x,y) &= e^{\frac{1}{4}\left(-k_2^2-k_1^2-4i(k_2+k_1)x-2\left(x^2+y^2\right)\right)}\\ &\quad\times\sqrt{\pi}\Big(2e^{\frac{k_2k_1}{2}+ik_2x+ik_1y}uv+e^{\frac{1}{4}\left(k_2^2+4ik_2x+k_1(k_1+4iy)\right)}\\ &\quad\times\Big(u^2+v^2\Big)+2e^{\frac{k_2k_1}{2}+ik_2x+ik_2y}vw+e^{\frac{1}{4}\left(k_2^2+k_1^2+4ij(x+y)\right)}v(u+w)\\ &\quad+e^{\frac{1}{4}\left(k_2^2+k_1(k+4i(x+y))\right)}v(u+w)+e^{\frac{1}{2}k(k_2+2i(x+y))}\Big(v^2+uw\Big)\end{aligned}$$

$$+ e^{\frac{1}{2}k_2(k_1+2i(x+y))}\left(v^2+uw\right)+e^{\frac{1}{4}\left(k_2^2+k_1(k_1+4ix)+4ik_2y\right)}\left(v^2+w^2\right)\Big). \tag{G.6}$$

This concludes the analytical exposition of this appendix. It has been verified that the numerical diagonalization of the above one-body density matrix reproduces the natural occupation numbers $\rho_{1/2}^{(NO)}$ of the exact solutions of the $N=2$ boson dynamics if values of coefficients in MCTDHB calculations are taken for the coefficients u, v, w.

Appendix H
Author's Works and Awards

Publications:

- *Numerically exact quantum dynamics of bosons with time-dependent interactions of harmonic type*, A.U.J. Lode, K. Sakmann, O.E. Alon, L.S. Cederbaum, and A.I. Streltsov, Phys. Rev. A **86**, 063606 (2012).
- *How an interacting many-body system tunnels through a potential barrier to open space*, A.U.J. Lode, A.I. Streltsov, K. Sakmann, O.E. Alon, and L.S. Cederbaum, Proc. Natl. Acad. Sci. USA **109**, 13521 (2012).
- *Wave chaos as signature for depletion of a Bose–Einstein condensate,* I. Březinová, A.U.J. Lode, A.I. Streltsov, O.E. Alon, L.S. Cederbaum, and J. Burgdörfer, Phys. Rev. A **86**, 013630 (2012).
- *Recursive formulation of the multiconfigurational time-dependent Hartree method for fermions, bosons and mixtures thereof in terms of one-body density operators*, O.E. Alon, A.I. Streltsov, K. Sakmann, A.U.J. Lode, J. Grond, and L.S. Cederbaum, Chem. Phys., **401**, 2 (2012).
- *Mechanism of Tunneling in Interacting Open Ultracold Few-Boson Systems*, A.U.J. Lode, A.I. Streltsov, O.E. Alon, and L.S. Cederbaum, arXiv:1005.0093 [cond-mat.quant-gas] (2010).
- *Exact decay and tunneling dynamics of interacting few boson systems,* A.U.J. Lode, A.I. Streltsov, O.E. Alon, H.-D. Meyer, and L.S. Cederbaum, J. Phys. B: At. Mol. Opt. Phys. **42**, 044018 (2009); see also: *Corrigendum*, J. Phys. B: At. Mol. Opt. Phys. **43**, 029802 (2010).
- *Excitation spectra of many-body systems by linear response: General theory and applications to trapped condensates*, J. Grond, A.I. Streltsov, A.U.J. Lode, O.E. Alon, and L.S. Cederbaum, Phys. Rev. A **88**, 023606 (2013).
- *Numerically-Exact Schrödinger Dynamics of Closed and Open Many- Boson Systems with the MCTDHB Package*,

A. U. J. Lode, *Tunneling Dynamics in Open Ultracold Bosonic Systems*,
Springer Theses, DOI: 10.1007/978-3-319-07085-8,

A.U.J. Lode, K. Sakmann, R.A. Doganov, J. Grond, O.E. Alon, A.I. Streltsov, and L.S. Cederbaum, Springer, High Performance Computing in Science and Engineering '13, pp 81-92, Nagel, W.E.; Körner, D.H.; Resch, M.M. (Eds.) (2013).

- *Elastic scattering of a Bose–Einstein condensate at a potential landscape*, I. Březinová, A. U. J. Lode, A.I. Streltsov, L.S. Cederbaum, O.E. Alon, L.A. Collins, B.I. Schneider, and J. Burgdörfer, Journal of Physics: Conference Series, ICPEAC Proceedings (2013).
- *Controlling the Velocities and Number of Emitted Particles in the Tunneling to Open Space Dynamics*, A.U.J. Lode, S. Klaiman, O.E. Alon, A.I. Streltsov, and L.S. Cederbaum, arXiv:1309.4253 [quant-ph], Phys. Rev. A **89**, 053620 (2014).
- *What to do with targeted IL-2.*
  H.N. Lode, R. Xiang, P. Perri, U. Pertl, A.U.J. Lode, S.D. Gillies, and R.A. Reisfeld, Drugs Today, **36**(5): 321 (2000).

Software:

- *The Recursive Multiconfigurational time-dependent Hartree for Bosons package*, http://r-mctdhb.org; http://schroedinger.org; http://ultracold.org, A.U.J. Lode, and M.C. Tsatsos (2013).
- *The Multiconfigurational time-dependent Hartree for Bosons package*, Version 2.3, Heidelberg, http://MCTDHB.org, A.I. Streltsov, K. Sakmann, A.U.J. Lode, O.E. Alon and L.S. Cederbaum (2013).
- *The Open Multiconfigurational time-dependent Hartree for Bosons package*, Version 2.3, Heidelberg, http://tc.uni-hd.de/mctdhb/OpenMCTDHB.html, K. Sakmann, A.U.J. Lode, A.I. Streltsov, O.E. Alon, and L.S. Cederbaum (2013).

Awards and Scholarships:

- Ph.D. Scholarship of the International Graduiertenkolleg 710, Complex Processes: Modeling, Simulation and Optimization, 2008.
- Dr. Sophie-Bernthsen award of the University of Heidelberg, 2011.
- Minerva Short Term Research Grant, 2012.

Contributions:

- *Mechanism of the Decay by Tunneling Dynamics in Interacting Open Ultracold Few-Boson Systems*,
  Hybrid Quantum Systems, Heidelberg (2010).
- *Tunneling Dynamics in Open Ultracold Bosonic Systems*,
  Finite-Temperature Non-Equilibrium Superfluid Systems, Heidelberg (2011).
- *Insights on the Many-Body Physics of Tunneling from Numerically Exact Solutions of the Time-Dependent Schrödinger Equation for Ultracold Bosons*,
  Seminar at the Technion, Haifa (2012);
  Quantum Technologies Conference, Warsaw (2012).
- *Numerically-Exact Schrödinger Dynamics of Closed and Open Many- Boson Systems with the MCTDHB Package*,
  16th HLRS Review workshop, Stuttgart (2013).

- *How tunneling of interacting bosons to open space works and how to control it*,
  Quantum Optics and Statistics Group, Freiburg (2013);
  Condensed Matter Theory and Quantum Computing Group, Basel (2013);
  Theoretical Chemistry Group, Heidelberg (2014).

References

1. O. Penrose, L. Onsager, Bose–Einstein Condensation and Liquid Helium. Phys. Rev. **104**, 576–584 (1956)
2. A. I. Streltsov, K. Sakmann, A. U. J. Lode, O. E. Alon, L. S. Cederbaum. The Multiconfigurational time-dependent Hartree for Bosons package, version 2.3, Heidelberg, (2012), see http://mctdhb.uni-hd.de.
3. P. Kramer, M. Saraceno *Geometry of the Time-Dependent Variational Principle* (Springer, Heidelberg, 1981)

Index

A. U. J. Lode, *Tunneling Dynamics in Open Ultracold Bosonic Systems*,
Springer Theses, DOI: 10.1007/978-3-319-07085-8,